UNIVERSALITY AND SCALING IN COMPRESSIBLE TURBULENCE AND MIXING

A Dissertation

by

JOHN PANICKACHERIL JOHN

Submitted to the Office of Graduate and Professional Studies of
Texas A&M University
in partial fulfillment of the requirements for the degree of

DOCTOR OF PHILOSOPHY

Chair of Committee,	Diego A. Donzis
Committee Members,	Rodney D. W. Bowersox
	Sharath Girimaji
	Eric Petersen
Head of Department,	Rodney D. W. Bowersox

August 2020

Major Subject: Aerospace Engineering

Copyright 2020 John Panickacheril John

ABSTRACT

Compressible turbulence and turbulent mixing play a critical role in diverse systems ranging from engineering devices to astrophysics. Examples include high-speed scram jets, hypersonic flows, combustion and star formation. The phenomenon is poorly understood due to complicated interactions between the compressible (dilatational) and vortical (solenoidal) modes in addition to the coupling of the flow field with thermodynamic variables. Attempts to make progress using traditional governing parameters, namely the Taylor Reynolds number, (R_λ) and the turbulent Mach number, (M_t) have been marred with inconsistencies and conflicting results in the literature. Resolving these discrepancies, further our understanding of this phenomena, develop new turbulence models for actual applications and affect flow control in practical situations are the ultimate objectives of this project. For this, we perform direct numerical simulations for a wide range of forcing conditions using state-of-the-art massively parallel codes that we show to be scalable up to 431200 cores at world-record resolutions. The aggregate database comprises an unprecedented wide range of values of the governing parameters. Through a novel asymptotic theoretical approach and systematic data analysis, we identify a new non-dimensional scaling parameter, δ, the ratio of compressible to vortical strength along with traditional parameters to unravel universal behaviour and scaling laws resolving several major issues currently plaguing the field. This could prove a paradigm shift in how compressible turbulence is studied. We predict the energy distribution across scales of the dilatational part of turbulent kinetic energy by dividing the $\delta - M_t$ plane into different physical regimes. These insights are also applied to passive scalar mixing. Although the large-scale of motion of passive scalars is oblivious to the effects of compressibility, it has a strong effect on the smallest scales. With these insights, we successfully parametrize the mixing efficiency in terms of the governing parameters. Our results have major implications in turbulence modeling paving the road towards more accurate, robust and generic models. In order to generate the current unique database, several computational issues had to be addressed, such as IO at scales, the use of accelerators, and the overhead associated with high levels of parallelism. Thus we also

contribute towards extending the capabilities of the grand computational challenge of simulating turbulence at realistic conditions seen in nature and engineering applications.

DEDICATION

To my family

ACKNOWLEDGMENTS

It is my great privilege to thank everyone who have helped me to achieve my dream of doing research and earning a Ph.D. This would not have been possible without these wonderful people in my life and interacting with them was a very rewarding experience for me.

First and foremost, I would like to express my deepest gratitude to Prof. Diego Donzis who gave me the opportunity to do research under his guidance. The rigour, commitment and determination with which he conducts research along with the passion, enthusiasm and great zeal he brings in are indeed admirable and inspiring. He has helped me imbibe and to develop a wide spectrum of skills required to do scientific research. It ranged from the objectivity in evaluating the current literature and formulating a research problem to the art of disseminating ones work through journals and oral presentations. Despite his busy schedule, he was always available and had time for all sorts of concerns and questions. I am grateful for the encouragement, kindness, and constant support he has given me throughout these years. Overall, he has been an excellent mentor, role model and true leader for me.

During my stay at TAMU, Dr. Donzis had given me the chance to meet and discuss my work with some of the world's eminent scholars in turbulence and fluid dynamics. I had the great privilege to collaborate with Dr. K. R. Sreenivasan. The insights and perspectives that he imparts from his long years of experience in this field have helped us to improve our work and he is a coauthor in many of the resulting papers from this dissertation. The most important skill I learned from him is in defining the scope of the research and finishing it. I would like to thank him for the warm hospitality during my visits to New York University.

I would like to thank Drs Bowersox, Girimaji and Petersen for agreeing to be a part of my dissertation committee. The comments and suggestions during the preliminary and final defense exams were helpful in improving the final dissertation. I have taken courses offered by both Drs. Bowersox and Girimaji which have immensely helped me in conducting research. I fondly remember the TAMU dinners in each APS meeting where Dr. Girimaji always shared his professional

experiences. I am an avid listener to Dr. Girimaji both in and outside of the class. I also thank our excellent department staff–Karen, Rebecca, Gail and Colleen– for all administrative help. I also would like to thank Dr. Gregory Blaisdell from Purdue who introduced me to Dr. Donzis and Dr. R. Vijayakumar from NIT, Calicut who taught me my first fluid dynamics course and thus instilling in me an interest and fascination for the subject which has endured to culminate in this research work.

Next, I would like to express my thanks to my wonderful and lively lab mates–Dr. Agustin, Dr. Aditya, Dr. Chang Hsin, Sualeh, Komal and Akansha– for their help. The discussion I had with them and at times uncomfortable and penetrating questions during group meetings on research have helped me to improve my work and presentation skills. I also made innumerable friends outside my research group. I would like to especially thank Hari, Jobin, Nilardi, Kavya, Dhanesh, Sidharth, Nikhil and my room mates: Josef, Mathews, Terin, Jemerson, Arun and Jithin for all their help and understanding.

Finally I would like to thank my family whose sacrifices made this possible. Thank you Appa, Amma, my sister Shobi chechi, her husband Nevin and and my niece Mireya for their unfaltering and unconditional love, support and prayers for me throughout these years. I am really grateful and thankful to my wife, Seba for the love and support along with the patience and sacrifices she has to go through to help me finish my Ph.D. I would also like extend my thanks to Seba's Appa, Amma and brother for the prayers and support. Special thanks to her brother, Ben for proof reading some sections of the dissertation for me.

I am forever grateful and indebted to everyone who helped me to accomplish this.

CONTRIBUTORS AND FUNDING SOURCES

Contributors

This work was supported by a dissertation committee consisting of Professors Diego Donzis (advisor), Rodney Bowersox of the Department of Aerospace Engineering, Sharath Girimaji of the Department of Ocean Engineering, and Professor Eric Peterson of the Department of Mechanical Engineering.

All other work conducted for the dissertation was completed by the student independently under the supervision of Dr. Diego Donzis

Funding Sources

Graduate study and research were supported by a NSF grant CBET-1605914 and used resources provided by the Extreme Science and Engineering Discovery Environment (XSEDE) supported by NSF.

NOMENCLATURE

NS	Navier-Stokes
R_λ	Taylor Reynolds number
DNS	Direct numerical simulation
LES	Large eddy simulation
PANS	Partially averaged Navier-Stokes
RANS	Reynolds averaged Navier-Stokes
Sc	Schmidt number
ν	Kinematic viscosity
D	Scalar diffusivity
ρ	Density
OC	Obukhov-Corrsin
η_B	Batchelor scale
η	Kolmogorov length scale
‘ M_t	Turbulent Mach number
u'	Total root-mean-square (rms) velocity
$\langle c \rangle$	Mean sound velocity
$\langle \epsilon_\phi \rangle$	Scalar dissipation rate
L	Integral length scale based on total energy spectrum
$\langle \phi^2 \rangle$	Scalar variance
u^s	Solenoidal root-mean-square velocity
u^d	Dilatational root-mean-square velocity
DIA	Direct interaction approximation

χ	Ratio of the dilatational to total kinetic energy
ϵ	Total dissipation
ϵ_s	Solenoidal dissipation
ϵ_d	Dilatational dissipation
δ	Ratio of dilatational to solenoidal kinetic energy
GPU	Graphics processing unit
S_{ij}	Strain rate tensor
α_p	Relative strength of dilatational to solenoidal forcing
OU	Ornstein–Uhlenbeck
WENO	Weighted essentially non-oscillatory
cDNS	Compressible direct numerical simulation
TACL	Turbulence and advanced computational laboratory
MPI	Message passing interface
OpenMP	Open Multi-Processing
MDS	Meta data server
MDT	Meta data target
OST	Object storage target
OSS	Object storage server
N	Number of grid points
SC	Stripe count
SS	Stripe size
NA	Number of aggregators
GPGPU	General purpose graphic processing unit
CPU	Central processing unit
API	Application programming interface

PGI	Portland group Inc
RK	Runge Kutta
Flop	Floating point operations per second
HPC	High perfromance computing
TF	Thermal forcing
HIT	Homogeneous isotropic turbulence
HST	Homogeneous shear turbulence
M_d	Dilatational Mach number
F_p	P-Equipartition function
DDE	Dilatationally dominated p-equipartition
Da	Damköhler number
C_{oc}	Obukhov-Corrsin constant
$K41$	Kolmogorov 1941 theory

TABLE OF CONTENTS

Page

ABSTRACT ii

DEDICATION iv

ACKNOWLEDGMENTS v

CONTRIBUTORS AND FUNDING SOURCES vii

NOMENCLATURE viii

TABLE OF CONTENTS xi

LIST OF FIGURES xiv

LIST OF TABLES xix

1. INTRODUCTION 1

    1.1 Turbulence, Mixing and Compressibility: An Overview 1
    1.2 Motivation, Background and Literature Review 4
        1.2.1 Motivation 4
        1.2.2 Background and Literature Review 6
    1.3 Objectives of the Present Work 11

2. DIRECT NUMERICAL SIMULATIONS AND HIGH-PERFORMANCE COMPUTING 13

    2.1 Governing Equations and Simulations 13
    2.2 Grid Convergence and DNS Database 14
    2.3 Challenges of I/O at Scales 16
        2.3.1 Lustre File System and MPI I/O 17
            2.3.1.1 Lustre File System 17
            2.3.1.2 MPI I/O 20
        2.3.2 Current Optimization Strategies Implemented in cDNS 22
        2.3.3 Optimization Strategy 23
    2.4 General Purpose GPU Computing 24
        2.4.1 Preliminary Benchmark Results 25

3. ASYMPTOTIC ANALYSIS OF COMPRESSIBLE NAVIER-STOKES EQUATION 31

    3.1 Decomposition of Velocity Field 31

3.2 Governing Equations of Solenoidal and Dilatational Kinetic Energy 31
3.3 Two Parameter Expansion: Asymptotic Analysis 34

4. UNIVERSALITY AND SCALING IN COMPRESSIBLE TURBULENCE 41

4.1 Background 42
4.2 Governing Parameters, Scaling and Similarity 42
4.3 The Role of Dilatational Motions 45
4.4 Self Similarity for Compressible Flows 49
4.5 The Scaling of Pressure in Compressible Turbulence 51
4.6 Small-Scale Universal Scaling 57
4.7 The Broader Picture 61
4.8 Summary 67

5. DISSIPATIVE ANOMALY IN COMPRESSIBLE TURBULENCE 70

5.1 Introduction 70
5.2 Total and Solenoidal Dissipation: Classical scaling 73
5.3 Alternate Scaling of Total Dissipation 75
5.4 Dilatational Dissipation 78
5.5 Criterion for Cascade and Dilatational Dissipative Anomaly 81
5.6 Summary 82

6. SPECTRA AND REGIMES IN COMPRESSIBLE TURBULENCE 84

6.1 Introduction 84
6.2 Background 86
6.3 Global Scaling Results 89
6.4 Energy Spectra 92
6.5 Compressible Regimes and Dilatational Energy Spectrum 95
6.5.1 No Cascade Regime 98
6.5.1.1 Pseudosound Regime 100
6.5.1.2 Classical Weak Equipartition 102
6.5.2 Cascade Regime: Solenoidally Driven Cascade 103
6.5.3 Acoustic Cascade / Wave Steepening Regime 105
6.5.4 Solenoidally Driven Cascade vs Acoustic Cascade 109
6.6 Intermediate Cascade Regime 112
6.7 Summary 114

7. MIXING IN COMPRESSIBLE TURBULENCE 117

7.1 Introduction 117
7.2 Failure of Classical Scaling 119
7.3 Rescaling with the Solenoidal Variables 122
7.4 Alignment of Scalar Gradient with Dilatational Flow Field 125
7.5 Summary 129

8. CONCLUSIONS AND FUTURE WORK 130

8.1 Conclusions 130
8.2 Future Research Directions 135
8.2.1 Computational Perspective 135
8.2.2 Physics Perspective 137

REFERENCES 139

APPENDIX A. ASYMPTOTIC EQUATIONS 155

A.1 Compressible Navier-Stokes Equations 155
A.2 Solenoidal Kinetic Energy Equations 156

LIST OF FIGURES

FIGURE Page

1.1 The Langley curve. Relative growth rate (ratio of compressible to incompressible growth rate) of mixing layer versus the convective Mach number (M_c). 5

1.2 The scalar Langley curve. Normalized scalar dissipation rate vs (a) R_λ and (b) M_t. In both figures, circles: 100%, triangles: $90-70\%$ and squares: $60-30\%$ solenoidal forced cases. In (a), the color scheme correspond to M_t: $M_t < 0.1$, $0.1 < M_t < 0.2$, $0.2 < M_t < 0.3$, $0.3 < M_t < 0.4$, $0.4 < M_t < 0.5$, $M_t > 0.5$ and in (b) colors correspond to R_λ: $R_\lambda < 40$, $40 < R_\lambda < 70$, $70 < R_\lambda < 115$, $115 < R_\lambda < 180$. The dashed line in (a) is the curve fit for the incompressible case with a smaller prefactor as in Donzis *et al.* [38]: $\langle \epsilon_\phi L/\langle\phi^2\rangle u' = A\left(1+\sqrt{1+(B/R_\lambda)^2}\right)$. 6

2.1 Resolution of normalized centralized moments for moderate dilatational forced cases. $(\mu - <\mu>)^p$ when p=2 and $\frac{(\mu-<\mu>)^p}{\left((\mu-<\mu>)^2\right)^{p/2}}$ when p =2,3, where in (a,c) $\mu = \omega$ (vorticity) and (b,d) $\mu = \theta$ (dilatation), 80% solenoidal forcing (a,b) 60% solenoidal forcing (c,d). 15

2.2 Resolution of normalized centralized moments for highly dilatational forced cases. $(\mu - <\mu>)^p$ when $p = 2$ and $\frac{(\mu-<\mu>)^p}{\left((\mu-<\mu>)^2\right)^{p/2}}$ when $p = 2, 3$, where in (a) $\mu = \omega$ (vorticity) and (b) $\mu = \theta$ (dilatation), 10% solenoidal forcing (a,b). θ correspond to the convergence of the small scale compressible motions. 16

2.3 Motivation: I/O performance. 17

2.4 Overview of file system. Reprinted from Hadri, introduction to parallel I/O online at *www.nics.tennessee.edu/files/pdf/hpcss13_14/04_08_Parallel_IO_Part1.pdf* [55]. 18

2.5 Division among OSTs. Reprinted from Hadri, introduction to parallel I/O online at *www.nics.tennessee.edu/files/pdf/hpcss13_14/04_08 _Parallel_IO_Part1.pdf* [55]. .. 18

2.6 A striping example. Reprinted from Hadri, introduction to parallel I/O online at *www.nics.tennessee.edu/files/pdf/hpcss13_14/04_08_Parallel_IO_Part1.pdf* [55]. ... 19

2.7 Stripe non-alignment. Reprinted from Logan and Dickens, towards an understanding of the performance of MPI-IO in Lustre file systems, 2008 IEEE international conference on cluster computing, Tsukuba, Japan. [86] 21

2.8 Strong scaling of cDNS. 26

2.9 (a) Time per step for CPU and GPU. (b) Percentage speed up for GPU. 27

3.1 Scaling of ϖ_d'/ϖ_s' with δ. 35

4.1 Scaling of variance of pressure with M_t. Dashed line is $\gamma^2 M_t^4/9$, the scaling proposed in [34]. 47

4.2 Scaling of variance of pressure with M_d. Dashed lines are $\gamma^2 M_d^2/F_T$ (high M_d) and $\propto M_d$ for reference (low M_d). 53

4.3 Scaling of variance of pressure with $\mathcal{D}$. Dashed lines are $\mathcal{D}^{-2}$ (low $\mathcal{D}$) for different values of A and the asymptotic DDE horizontal lines (high $\mathcal{D}$). 55

4.4 Contours of $|\nabla p|/\ |\nabla p|_{rms}$ for $(\mathcal{D}, R_\lambda, M_t, \delta) = (0.04, 58, 0.09, 0.0035)$ (a), $(0.27, 102, 0.36, 0.097)$ (b), $(12, 50, 0.20, 1.4)$ (c), and $(52, 51, 0.06, 1.65)$ (d). 56

4.5 Scaling of ratio of dilatational to solenoidal dissipation with (a) M_t and (b) δ. Dashed line in (b) with a slope of 2 for reference. 59

4.6 Scaling of the negative skewness of the velocity gradient with (a) M_t and (b) δ. 60

4.7 Scaling of the negative of the skewness of the velocity gradient with $\delta^2 M_t$. 61

4.8 Regions in the δ-M_t diagram: Dilatationally dominated p-equipartition (DDE, $\mathcal{D} > \mathcal{D}_{crit}$), S-divergence ($\delta^2 M_t > 2 \times 10^{-2}$), and $\langle \epsilon_d \rangle / \langle \epsilon_s \rangle > 1$. (a) Entire database in Table 4.1. (b) Selected trajectories which include isotropic cases with two types of solenoidal forcing, cases with dilatational forcing, and homogeneous shear flows. .. 63

5.1 (a) Total dissipation normalized by total velocity and integral length scale based on total energy spectrum vs total Taylor Reynolds number. (b) Total dissipation normalized by total velocity and integral length scale based on total energy spectrum vs turbulent Mach number. Here and in all figures to follow in this chapter, circles: pure solenoidal forcing; triangles: percentage of dilatational forcing between 10 to 30 (weak dilatational forcing); squares: percentage of dilatational forcing between 40 to 60 (moderate dilatational forcing); diamonds: percentage of dilatational forcing between 70 to 100 (strong dilatational forcing). In (a), the colors correspond to turbulent Mach number: $M_t < 0.1$, $0.1 < M_t < 0.25$, $0.25 < M_t < 0.4$, $0.4 < M_t < 0.6$, $M_t > 0.6$ and in (b) colors correspond to R_λ: $R_\lambda < 20$, $20 < R_\lambda < 40$, $40 < R_\lambda < 70$, $70 < R_\lambda < 115$, $115 < R_\lambda < 180$, $180 < R_\lambda < 280$, $280 < R_\lambda < 500$. 73

5.2 (a) Solenoidal dissipation normalized by solenoidal rms velocity and solenoidal integral length scale based on total energy spectrum vs total Taylor Reynolds number. (b) Solenoidal dissipation normalized by solenoidal rms velocity and solenoidal integral length scale based on total energy spectrum vs solenoidal Taylor Reynolds number. In both figures, the color scheme corresponds to M_t as in Fig. 5.1 (a). The dashed line in (a) and (b) correspond to expressions in Eq. 5.2 and Eq. 5.5 respectively. 74

5.3 (a) Total dissipation normalized by solenoidal rms velocity and solenoidal integral length scale based on total energy spectrum vs δ. (b) Scaling of modified parameters, $\delta^{-3}C'$ vs $\delta^3 R_\lambda$. In both figures, the color scheme corresponds to R_λ as in Fig. 5.1 (b). The dashed lines in (a) and (b) correspond to a power law of 3 and -1 respectively. 76

5.4 Transitional δ as a function of Taylor Reynolds number. 77

5.5 Dilatational dissipation normalized by dilatational rms velocity and integral length scale based on dilatational energy spectrum vs (a) total Taylor Reynolds number, R_λ and (b) dilatational Taylor Reynolds number, R^d_λ. In (a) and (b), the color schemes correspond to M_t as in Fig. 5.1 (a) and R_λ as in Fig. 5.1 (b) respectively. .. 79

5.6 Dilatational dissipation normalized by dilatational rms velocity and integral length scale based on dilatational energy spectrum vs (a) δ and (b) δM_t for cases with $D = \delta\sqrt{\delta^2+1}/M_t < 0.5$. In both figures, color scheme corresponds to R_λ as in Fig. 5.1 (b). In (b), the cases where $R_\lambda < 30$ are not plotted. The dashed line in (a) has a power law of -1.25. 80

5.7 Normalized dilatational dissipation with shocklet strength for $D < 0.5$ and $R_\lambda > 30$ vs δM_t (a) in log-log scale and (b) log-linear scale. In both figures, color schemes corresponds to R_λ as in Fig. 5.1 (b). The dashed line in (a) has a power law of -2. 81

5.8 Normalized dilatational dissipation with shocklet strength for all cases vs δM_t. In the figure, color scheme corresponds to $D < 0.16$, $0.16 < D < 0.5$, $0.5 < D < 2.25$, $2.25 < D < 10$, $10 < D < 50$, $50 < D < 150$, $150 < D < 1100$. 82

6.1 (a) Dilatational energy spectra at $M_t \approx 0.1$ for different magnitudes of δ. (b) Current stationary homogeneous simulations in literature discussing dilatational energy spectra on $\delta - M_t$ phase plane. 85

6.2 Scaling of advection terms. (a) A_{c4} vs δ^2 (b) A_{c4} vs $\delta^2 M_t$ (c) A_{c2} vs δ^2 (d) A_{c2} vs $\delta^2 M_t$. Dashed lines are power law scaling in (a) $(\delta^2)^1$, (b) $(\delta^2 M_t)^{1.0}$, (c) $(\delta^2)^1$ and (d) $(\delta^2 M_t)^{1.0}$. 89

6.3 Scaling of advection terms. (a) A_d vs δ^3 (b) A_s vs δ (c) A_{c1} vs δ (d) A_{c3} vs δ. Dashed lines are power law scaling in (a) $(\delta)^3$, (c) $(\delta)^1$ and (d) $(\delta)^1$. 91

6.4 Scaling of ratio of dilatational to solenoidal dissipation ratio: $\langle\epsilon_d\rangle/\langle\epsilon_s\rangle$ vs $\delta^2 M_t$. Dashed line is power law scaling corresponding to $(\delta^2 M_t)^{1.3}$. 92

6.5 Kolmogorov compensated solenoidal (a) and dilatational (b) spectra. 93

6.6 $\delta - M_t$ phase plane, intermediate division (a) and final division (b); In both figures, A: pseudosound regime, B: classical weak equipartition, C: transition regime from non-cascade to cascade, D: solenoidal dominated cascade regime, E: wave steepening regime. 98

6.7 Dilatational spectra in the pseudo sound regime, $(\delta, M_t)\, d : [\delta M_t < 0.01, D < 0.5]$, Reynolds averaged compensated spectra (a),(c) and Kida averaged compensated spectra (b),(d). 101

6.8 Dilatational spectra in the equipartition regime, $(\delta, M_t) : [\delta M_t < 0.01, D > 0.5]$, Reynolds averaged compensated spectra (a) and Kida averaged compensated spectra (b). 102

6.9 Non-cascade regimes in $\delta - M_t$ phase plane. (a) Pseudosound and (b) Weak equipartition. 103

6.10 Dilatational spectra in the full developed solenoidal driven cascade regime; $(\delta, M_t) : [\delta M_t > 0.1, \delta < 0.3]$; Reynolds averaged spectra (a) Kida averaged spectra (b). 105

6.11 Dilatational energy spectra at wave steepening regime; $\delta M_t \approx O(1)$ and $\delta > 1.0$; Kolmogorov normalization (a) new normalization (b) dashed line in (a) correspond to power law of $k^{2.1}$ and in (b), a constant line. 108

6.12 (a) Dilatational energy spectra at fully developed solenoidally driven cascade regime: $\left[0.15 < \delta M_t < 0.09, \frac{\delta}{M_t} < 5.0\right]$ or $\left[\delta M_t > 0.15, \frac{\delta}{M_t} < 1.0\right]$. The red and black dashed lines correspond to a passive scalar and solenoidal spectrum respectively. (b) Dilatational energy spectra at Wave steepening regime: $\left[0.15 < \delta M_t < 0.09, \frac{\delta}{M_t} > 5.0\right]$ or $\left[\delta M_t > 0.15, \frac{\delta}{M_t} > 1.0\right]$ (b). 111

6.13 Cascade regimes in $\delta - M_t$ phase plane. (a) Fully developed solenoidal driven cascade and (b) Wave steepening. 112

6.14 Dilatational spectra in transition regime from "non-cascade" regimes to "cascade" regimes, $0.01 < \delta M_t < 0.1$. $D > 0.5$, variation with δ at constant $M_t \approx 0.1$ (a) $D > 0.5$, variation with M_t with constant $\delta \approx 0.1$ (b). 113

6.15 (a) Transition regime from non-cascade to cascade in the $\delta - M_t$ phase plane. (b) Dilatational spectra in transition regime from "non-cascade" regimes to "cascade" regimes, $0.01 < \delta M_t < 0.1$ and $D < 0.5$. 114

6.16 Final $\delta - M_t$ phase plane. The acronyms "W.E" and "S.D.D.C" in the figure correspond to weak equipartition and solenoidal driven dilatational cascade respectively. . 116

7.1 The Obukhov-Corrsin compensated scalar spectra using total dissipation and Kolmogorov length scale based on the total energy dissipation. No scaling is observed. Dashed line is for the incompressible case. In this figure and rest of the figures in this chapter unless otherwise stated, colors correspond to R_λ: $R_\lambda < 40$, $40 < R_\lambda < 70$, $70 < R_\lambda < 115$, $115 < R_\lambda < 180$. 120

7.2 Alignment of scalar gradient $(\nabla\phi)$ with the eigen-directions of the S_{ij}, i.e. $e_\gamma, e_\beta, e_\alpha$ which correspond to the eigenvalues (γ, β, α) with $\gamma < \beta < \alpha$. 121

7.3 The Obukhov-Corrsin compensated scalar spectra using solenoidal dissipation $\langle \epsilon_s \rangle$ and solenoidal Kolmogorov length scale based on the solenoidal energy dissipation. Excellent collapse is observed. Dashed line is for the incompressible case. 122

7.4 Normalized eigenvalues of the solenoidal symmetric velocity gradient tensor S^s_{ij}: (i) $\hat{\beta}_s = \sqrt{6}\beta_s/\sqrt{\alpha_s^2 + \beta_s^s + \gamma_s^2}$; (ii) β_s/γ_s. 124

7.5 (a) Alignment of scalar gradient $(\nabla\phi)$ with e^s_α, e^s_β and e^s_γ, the eigenvectors of S^s_{ij}. (b) Probability that the scalar gradient $(\nabla\phi)$ aligns perfectly with the eigendirection e^s_γ corresponding to the most compressive eigenvalue. In (b), the symbols correspond to % of dilatational forcing: circles: 0% dilatational forcing; triangles: $10 - 30\%$ dilatational forcing; squares: $30 - 60\%$ dilatational forcing; diamonds: $70 - 80$ % dilatational forcing; stars: $80 - 100$ % dilatational forcing. 125

7.6 Fine scale structure of scalar dissipation using dilatational variables. Alignment of scalar gradient $(\nabla\phi)$ with the eigendirections of the symmetric part of the dilatational velocity gradient S^d_{ij} at $M_t < 0.1$ for (a) purely solenoidal forcing (low δ) and (b) more than 50% dilatational forcing. Here and in the figure to follow, 'diamonds', 'dashed lines' and 'solid lines correspond to most compressive $\left(\mathbf{e}^\mathbf{d}_\gamma\right)$, intermediate $\left(\mathbf{e}^\mathbf{d}_\beta\right)$ and most expansive directions $\left(\mathbf{e}^\mathbf{d}_\alpha\right)$, respectively. 126

7.7 Fine scale structure of scalar dissipation for dilatationally-dominated conditions. The alignment of scalar gradient $(\nabla\phi)$ with eigendirections of the symmetric part of the dilatational velocity gradient tensor, S^d_{ij} at $M_t > 0.1$ for (a) purely solenoidal forcing (low δ) and (b) more than 50% dilatational forcing (high δ). 127

LIST OF TABLES

TABLE

Page

1.1 Scaling predicted by compressible theories. 9

1.2 Scaling observed in DNS; $^+$ corresponds to cases with ratio of bulk to shear viscosity = 30; HST: homogeneous shear forced cases. 10

2.1 Current DNS database..... 29

4.1 Databases used in this study. Flow types: homogeneous isotropic turbulence (HIT), which can have solenoidal forcing (S, circles), some dilatational forcing (D, triangles), homogeneous shear turbulence (HST, squares), or thermal forcing (TF). We also include flows (HIT, HST) with different types of gases, in particular two studies with gases for which the ratio of bulk to shear viscosity is 30 (BV) compared to zero for all the other cases. Studies with multiple symbols correspond to the different conditions marked with a † in increasing order. Studies marked with an asterisk did not provide δ and was thus computed using pressure fluctuations and Eq. 4.9. 48

6.1 Available dataset of homogeneous compressible turbulence in the literature and current study; Driving mechanisms are HIT,S (homogeneous isotropic turbulence, solenoidal forcing, circles), HIT, D (homogeneous isotropic turbulence, dilatational forcing, triangles depending on α_p), HST (homogeneous shear, squares) and TF (thermal forcing, rhombus). Color schemes of present data based on R_λ with $R_\lambda < 40$ $40 < R_\lambda < 70$, $70 < R_\lambda < 115$, $115 < R_\lambda < 180$ 86

6.2 Table illustrating the transition from pseudosound for a wide range of driving mechanisms. Driving mechanisms are HIT,S (homogeneous isotropic turbulence, solenoidal forcing, circles), HIT, S, BV (homogeneous isotropic turbulence, solenoidal forcing with ratio of bulk to shear viscosity equals 30, crosses), HST (homogeneous shear, squares) and HST,BV (homogeneous shear with ratio of bulk to shear viscosity equals 30.) 99

1. INTRODUCTION

1.1 Turbulence, Mixing and Compressibility: An Overview

Turbulence is a phenomenon of extraordinary complexity and is the most common state of fluid motion in nature and engineering. Turbulence plays a major role in many applications in diverse fields including astrophysics, atmospheric clouds, propulsion, medicine, pollutant transport and many more industrial processes of paramount importance to society. In some of these, it is justifiable to assume that the velocity field is incompressible. This implies that, the volume of any fluid element is conserved as it translates, rotates and deforms, and which further leads to a constant density field. Despite this simplification and the progress made through systematic research for many decades, turbulence still evades a complete understanding or theory and remains a formidable scientific challenge even today. This is perhaps epitomized or embodied by R. P. Feynmann's quote on turbulence: *Turbulence is the most important unsolved problem of classical physics.*

The primary reason for the immense difficulty in analyzing turbulence – theoretically, numerical or experimentally – is that, it is governed by a set of strongly coupled non-linear partial differential equations collectively known as the *Navier-Stokes* (NS) equations. The non-linearity and coupling inherent in the Navier-Stokes equations introduce several challenges such as non-integrability, extreme sensitivity to initial conditions, multi-scale behavior, and non-locality which makes it exceedingly difficult to analyze.

The non-integrability and the extreme sensitivity to initial conditions, typical signatures of chaotic motions, present extreme mathematical and theoretical challenges. For example, the existence and uniqueness of the solution for Navier-Stokes are open research questions and rightly a millennium problem of the Clay mathematical institute. Although, the Navier-Stokes equations are deterministic in nature, the strong sensitivity to initial condition renders a deterministic theory or an analytical solution for turbulence very unlikely. Although there are some deterministic

approaches to turbulence, for example coherent structures in the flow field, by far, the statistical or stochastic approach towards turbulence is most common. The stochastic approach has led to one of the most successful and widely recognized theories in turbulence, namely, the self-similar theory of Kolmogorov [70, 71]. The essence of this theoretical framework is that at high enough scale separation, statistical properties of the flow field after appropriate ensemble averaging are universal and independent of the external environment producing or sustaining turbulence.

These hindrances to the theoretical approach have led researchers to study turbulence experimentally and numerically. Since the focus of this dissertation is computational in nature, we briefly describe the approach and state the challenges involved in numerical investigations of turbulence. Due to the multi-scale nature of turbulence, the flow field contains a wide range of spatial and temporal scales. The separation between the largest and smallest scales increases with the Taylor Reynolds number, R_λ which is a measure of the strength of inertial forces relative to viscous forces, and is typically very high in applications of interest. Simulations that resolve all relevant scales of motion are called direct numerical simulations (DNS). The demand on the computational resources needed for a DNS steeply rises as R_λ^6. Along with this, the additional computational complexity to resolve complex geometries makes DNS infeasible for practical engineering applications. Thus, DNS has historically been limited to low R_λ or simple canonical geometries. However, the insights from these high-fidelity DNS simulations and phenomenological theories have been widely used for turbulence modeling. These turbulence models are then used for low-fidelity engineering simulations such as Large eddy simulations (LES), Partially averaged Navier-Stokes (PANS) and Reynolds averaged Navier-Stokes (RANS).

One of the defining features of turbulence is its ability to mix components efficiently which can be orders of magnitude greater than that due to pure molecular diffusion [131]. This property is pivotal in sustaining life [28], formation of stars [49] and design of many engineering applications such as turbulent combustion [101]. Most of the discussions about the velocity field directly apply to passive scalar mixing where the mixing process does not affect turbulence or the flow field. Apart from R_λ, an extra parameter, Schmidt number, $Sc = \langle\nu\rangle/D$, the ratio of momentum to

scalar diffusivity is required. For, $Sc \approx 0(1)$, the range of scales of passive scalars are similar to that of the velocity field. Analogous to the velocity field, phenomenological statistical theory such as Obukhov-Corrsin (OC) scaling exists for passive scalars. However for less diffusive scalars, $Sc > 1$, the range of scales of motions of scalars are greater than that of the velocity field. The smallest scale in the scalar field is the Batchelor scale, $\eta_B = Sc^{-1/2}\eta$, which is smaller than the Kolmogorov scale, $\eta = \left(\nu^3/\langle\epsilon\rangle\right)^{1/4}$, the smallest scale in the velocity field. The need to resolve Batchelor scale increases the computational requirements for a fixed R_λ. For $Sc > 1$, this increase in the scale separation leads to multiple scaling regimes proposed by Batchelor [9] for high Schmidt numbers.

The situation for compressible turbulence, though much more prevalent in real situations, is even more challenging. In compressible turbulence, the volume of the fluid is no longer preserved. Thus density is no longer a constant but a stochastic fluctuating variable. As a result, the inclusion of compressibility effects on turbulence increases the complexity of the problem enormously. The challenges grow from theoretical, numerical and experimental perspectives. Therefore, the literature on compressible is more limited and compared to incompressible turbulence, our fundamental understanding lags behind. The experimental challenges are also enormous as it is very hard to control the parameters required to realize canonical flows in laboratories to study its fundamental characteristics. Thus, virtually no experimental studies exist on this.

From a theoretical and numerical perspective, compressible turbulence has a much more complicated set of governing non-linear partial differential equations. Moreover, the thermodynamic and hydrodynamic processes are coupled. Theoretically, this leads to more correlations among the stochastic variables making the problem even more intractable. From a numerical standpoint, the computational complexity of the problem increases since there are more number of equations to be solved and the resolution requirements also increase due to additional fine scale structures such as shocklets [113]. With the relentless increase of the massive computational power available today, it is now possible to perform DNS of compressible turbulence at conditions and parameter ranges much closer to those found in real application. The objective of this work is, thus, to leverage

world-class computational resources to study homogeneous isotropic compressible turbulence and its effect on mixing for a wide range of compressibility conditions.

1.2 Motivation, Background and Literature Review

1.2.1 Motivation

One well known compressibility effect on turbulence dynamics is encountered in canonical compressible shear layer flows. The drastic effect of compressibility on the dynamics of such a flow can be seen in Fig. 1.1 [52] which is the so-called "Langley curve". This curve shows that the relative growth rate of the width of compressible shear layer, which is a measure of momentum mixing, decreases with convective Mach number for the data collected from a large number of studies including both experiments and simulations. This flow configuration has been studied extensively [121] and the physical mechanism for the reduction of growth rate has been attributed to the reduced production of turbulent kinetic energy due to compressibility [115, 137] rather than mere density variation as assumed in Markovin's hypothesis. The fundamental insights gained from this canonical problem have spurred considerable research in compressible turbulence and led to the development of improved models.

One of the biggest successes in incompressible turbulence is the self-similarity theories of Kolmogorov [70, 71], where the non-dimensional variable, R_λ, comprising of intrinsic turbulent variables is identified to characterize the behaviour. This helped in unravelling universal behaviour across a wide variety of flows independent of external mean flow, initial or boundary conditions. Since compressible turbulence has additional physics, an extra intrinsic parameter, the turbulent Mach number, $M_t = u'/\langle c \rangle$ has been introduced in the literature. Taken together, the accumulated data from research so far show that the current governing parameters (R_λ and M_t) are insufficient to characterize the behaviour of compressible turbulence. The characteristics depend on the external environment that sustains or produces the turbulent fluctuations such as initial and boundary conditions. For example, the reduced growth rate in the mixing layer, seen in Fig. 1.1 is better characterized by a mean flow parameter, M_c (gradient Mach number, M_g for shear layers) rather

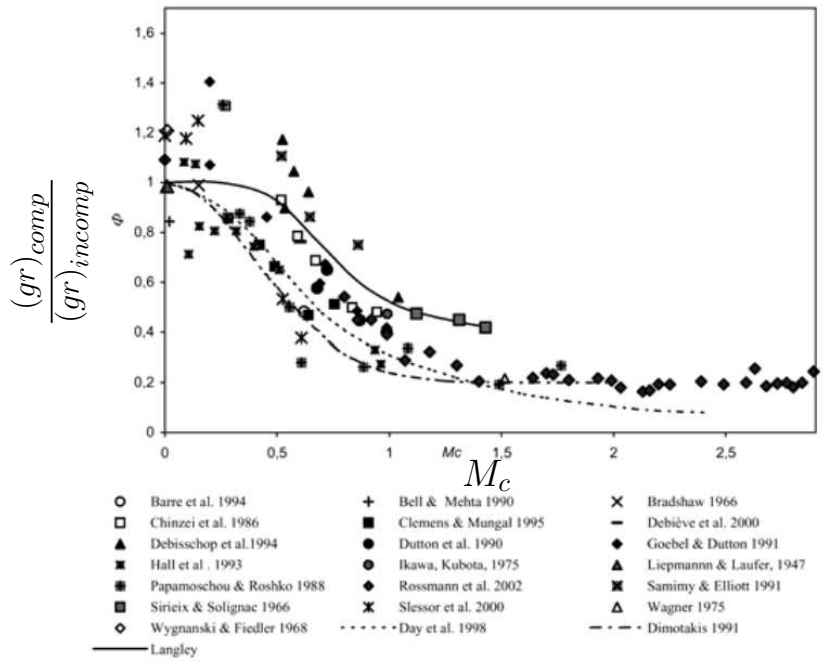

Figure 1.1: The Langley curve. Relative growth rate (ratio of compressible to incompressible growth rate) of mixing layer versus the convective Mach number (M_c).

than the intrinsic parameter, M_t.

The inadequacy of M_t and R_λ is even true for the homogeneous isotropic turbulence as we illustrate in Fig. 1.2. As an example we show the normalized scalar dissipation, $\langle \epsilon_\phi L/\langle\phi^2\rangle u'$. Clearly one can see from the Fig. 1.2 that mixing indeed depends on the forcing characteristics. One can see depending on forcing conditions and M_t, the normalized dissipation rate deviates from the dissipative anomaly trend seen in incompressible turbulence. As we show in this work, this lack of universality in M_t is true for virtually all quantities of interest.

This is clearly a hindrance for the development of theories for both velocity and scalar fields. The statistical theories of isotropic turbulence based on universality principles have played a pivotal role in the development of subgrid and turbulence models for LES and RANS simulations in incompressible turbulence. Therefore, lack of universality in compressible turbulence has also impeded the progress in the development of robust and general subgrid and turbulence models. A major reason for this state of affairs is the lack of high fidelity DNS data for wide ranges of

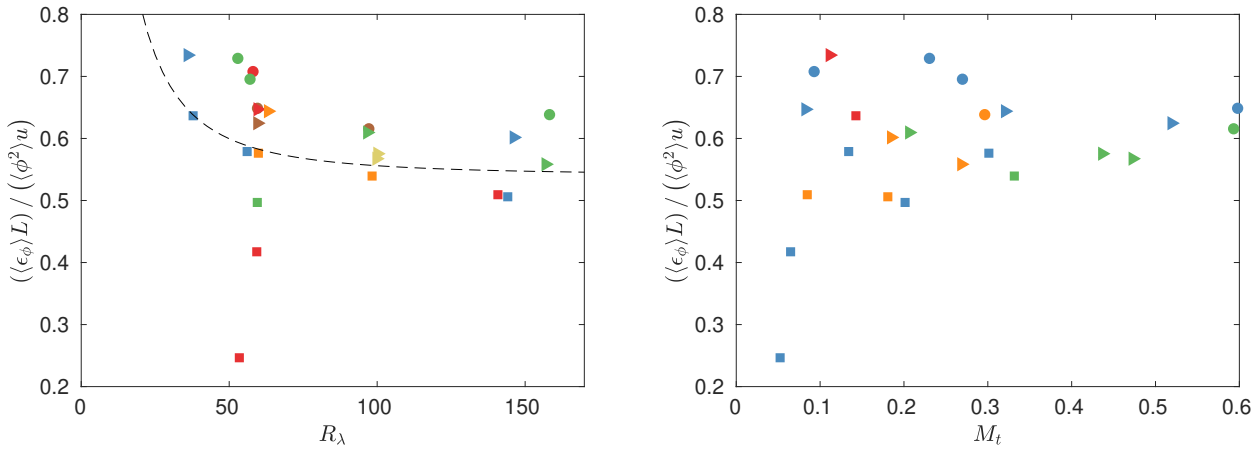

Figure 1.2: The scalar Langley curve. Normalized scalar dissipation rate vs (a) R_λ and (b) M_t. In both figures, circles: 100%, triangles: $90-70\%$ and squares: $60-30\%$ solenoidal forced cases. In (a), the color scheme correspond to M_t: $M_t < 0.1$, $0.1 < M_t < 0.2$, $0.2 < M_t < 0.3$, $0.3 < M_t < 0.4$, $0.4 < M_t < 0.5$, $M_t > 0.5$ and in (b) colors correspond to R_λ: $R_\lambda < 40$, $40 < R_\lambda < 70$, $70 < R_\lambda < 115$, $115 < R_\lambda < 180$. The dashed line in (a) is the curve fit for the incompressible case with a smaller prefactor as in Donzis *et al.* [38]: $\langle\epsilon_\phi L/\langle\phi^2\rangle u' = A\left(1+\sqrt{1+(B/R_\lambda)^2}\right)$.

possible compressibility conditions.

This forms the major motivation of this dissertation. Using high fidelity DNS data of compressible homogeneous isotropic turbulence at unprecedented resolutions and for a wide range of conditions in terms of R_λ, M_t and forcing, we show that universality is possible for compressible turbulence by expanding the parameter space. The insights from our analysis can help to explain many discrepancies in the current literature and provides insight into the characteristics of the "scalar Langley curve" in Fig. 1.2 among many others. Our work has the potential to lead towards a more general theory of compressible turbulence and thus the development of robust turbulence models. In the next section, we give a brief review of compressible turbulence and mixing literature concentrating mainly on the homogeneous isotropic turbulence.

1.2.2 Background and Literature Review

In compressible turbulence, as discussed before, we observe fluctuations in density and virtually all thermodynamic variables that result in additional types of motions in the flow field.

Kovasznay [73] first showed that apart from the vortical modes seen in incompressible turbulence, there are acoustic and entropy modes. Unlike the vortical modes, the divergence of the velocity corresponding to acoustic and entropy modes is not zero. He demonstrated that after linearizing the governing equations, to first order, all three modes are decoupled. However at higher orders, these modes become coupled and, moreover, Chu and Kovasznay [24] showed that any mode can be generated by the interaction between other modes due to the non-linear interactions in the governing equations.

In general, due to non-linearity, it is hard to decompose the total velocity field into Kovasznay modes. Thus it is common in the literature to decompose the velocity using Helmholtz decomposition into solenoidal and dilatational components. For a homogeneous flow field, this decomposition is unique. The solenoidal part of the velocity field is divergence free ($\nabla \cdot \mathbf{u^s} = 0$) whereas the dilatational part is curl free $\left(\nabla \times \mathbf{u^d} = 0\right)$. Thus the solenoidal and dilatational part can be interpreted as the incompressible and compressible physics of the velocity field, respectively. Although there are other ways to decompose the velocity field, the Helmholtz decomposition is by far the most widely used in fundamental studies of compressible turbulence and is also used here.

Theoretical and numerical studies aim to measure compressibility effects by studying the behaviour of the dilatational part and its interaction with solenoidal component as a function of the compressibility parameters which in the case of isotropic turbulence is M_t. Due to the complexity of the governing equations, it is common to attempt to simplify them using various asymptotic analyses under the assumption of low M_t. One such attempt is the equipartition theory proposed by Sarkar *et al.* [118] based on the assumption that turbulent and acoustic time scales are separated. This results in the dilatational part of the velocity flow field evolving independently of the solenoidal part. In such a case, one expects acoustic oscillations in the flow filed corresponding to the harmonic energy transfer between the dilatational kinetic and internal energy. The equipartition phenomenon has been observed in numerical simulations of decaying [80] and shear flows [11] at low M_t. However for solenoidally forced flows [61, 140], equipartition is not observed at low M_t but surprisingly was seen at high M_t.

Another low-M_t asymptotic result is the pseudosound theory proposed by Ristorcelli [110]. It is based on a length scale separation argument where the pressure waves are generated inside a compact turbulent source. Pseudosound theory is valid inside this compact space where the dilatational pressure is not acoustic in character. The main insight from this theory is that the dynamics of the dilatational motions is completely enslaved to the solenoidal mode. Thus, the major dilatational statistics can be derived from the solenoidal variables. Pseudosound behavior was indeed observed in the solenoidally forced DNS of Wang [140]. These two low-Mach-number regimes together are known as the low-Mach number quasi-isentropic regime in the literature [112]. Various other low-Mach-number thermal regimes based on asymptotic analysis [10, 157, 158] were also proposed where the flow field have significant heat effects which are distinct from pure acoustic effects.

Another important theoretical approach is Kriachnan's DIA [112] from which one can derive the Eddy damped quasi-normal markovian (EDQNM) equations. The resulting equations need to be numerically solved but is computationally less expensive than DNS. Although these are strictly valid at low M_t, numerical studies of EDQNM equations were also extended to high M_t. It should be noted, however that results based on EDQNM are extremely sensitive to the damping factor used in the simulations [112].

All the above theoretical approaches are valid at low M_t and can predict characteristics of the dilatational flow field statistics based on some assumptions. With the rapid advancement of computational power, it is now possible to conduct DNS of compressible turbulence for reasonably high R_λ. Thus DNS has become a major tool in understanding the physics of compressible turbulence at high M_t and R_λ. This regime of relatively high M_t (but less than unity) is known as nonlinear subsonic regime [112]. The focus of the current dissertation is also on cases with $M_t < 1$. The supersonic regime where $M_t > 1$ is important in astrophysical contexts and the literature is even more scarce [105, 106, 107].

In the rest of the section, we discuss the major results predicted and observed by the theories described above and DNS. We then discuss some important dilatational statistics.

	E_{dd}	K_d/K_s	$\langle\epsilon_d\rangle/\langle\epsilon_s\rangle$
EDQM1	$M_t^2 R_L k^{-11/3}$	$M_t^2 R_L$	M_t^2
EDQM2	$M_t^4 k^{-3}$	M_t^4	$M_t^4 R_L^{-1} ln\,(R_L)$
Equipartition	.....	M_t^2	M_t^2
Pseudosound	$M_t^4 k^{-3}$	M_t^4	M_t^4

Table 1.1: Scaling predicted by compressible theories.

The ratio of the dilatational to total kinetic energy, $\chi = u_d^2/u^2$ is considered a measure of the strength of compressible motions at large scales. Equipartition predicts a scaling of the form $\chi \sim M_t^2$ compared to M_t^4 [110] predicted by pseudosound theory. EDQNM theory predicts a scaling of the form $K_d/K_s \sim M_t^2 R_L$ or M_t^4 depending on the damping factor, where $K_d/K_s \approx u_d^2/u_s^2$ which is approximately equal to χ at low compressibility conditions. Jagannathan and Donzis [61] conducted solenolidally forced DNS which showed that at low $M_t < 0.3$, K_d/K_s scales as M_t^4 consistent with the pseudosound theory. The system undergoes a transition at $M_t \approx 0.3$, after which, K_d/K_s scales as M_t^2. This transition was later confirmed by other DNS studies but this transitional M_t was not universal across studies [22, 23, 140]. In fact, Chen *et al.* [23] showed that scaling consistent with pseudosound theory continues at least up to $M_t \approx 0.6$ with bulk viscosity. Wang [144] conducted DNS with 50% dilatational forcing and found that the ratio of kinetic energies was independent of M_t whereas thermally forced DNS [145] showed that χ decreases with M_t.

Similar transition was observed for other important dilatational statistics such as the ratio of dilatational to solenoidal dissipation, $\langle\epsilon_d\rangle/\langle\epsilon_s\rangle$ which is considered as the measure of the compressibility strength at small scales. The equipartition theory predicts an M_t^2 scaling compared to M_t^4 predicted by pseudosound. Similar scaling but with a Reynolds number correction was also predicted by EDQNM studies. At high M_t, simulations using EDQNM showed a M_t^5 scaling for the ratio of dissipation [112]. We summarize the scaling of this ratio from various DNS studies in Table 1.2. The main conclusion from all these results is the apparent difficulty across the literature to find universal behavior in compressible flows.

	Forcing	M_t range	E_{dd}	K_d/K_s	$\langle\epsilon_d\rangle/\langle\epsilon_s\rangle$
Jagannathan and Donzis [61]	100 % solenoidal	$M_t \leq 0.3$	.....	M_t^4	negligible
Jagannathan and Donzis [61]	100 % solenoidal	$0.3 \leq M_t \leq 0.6$	.....	M_t^2	$M_t^{4.1}$
Wang *et al.* [140]	100 % solenoidal	$M_t \leq 0.2$	$M_t^4 k^{-3}$	M_t^4	M_t^4
Wang *et al.* [140]	100 % solenoidal	$0.4 \leq M_t \leq 1.0$	.....	M_t^2	M_t^5
Wang *et al.* [144]	50 % solenoidal	$0.3 \leq M_t \leq 0.65$	k^{-2}	constant	constant
Wang *et al.* [22]	HST	$M_t \leq 0.1$	.....	M_4	M_t^4
Chen *et al.* [22]	HST	$0.3 \leq M_t \leq 1.0$	.....	M_t^2	.....
Chen$^+$ *et al.* [23]	100 % solenoidal	$0.1 \leq M_t \leq 0.6$	$M_t^4 k^{-3}$	M_t^4	.....

Table 1.2: Scaling observed in DNS; $^+$ corresponds to cases with ratio of bulk to shear viscosity = 30; HST: homogeneous shear forced cases.

The normalized mean dissipation rate, $D \equiv \langle\epsilon\rangle L/u^3$ plays a pivotal role in the dynamics of incompressible turbulence which is expected to asymptote to a constant at high R_λ. This behaviour, known as the "Zeroth law of turbulence" or dissipative anomaly [88], has been verified both numerically and experimentally for incompressible turbulence for a wide variety flows [88, 135]. Studies on dissipative anomaly are very scarce for compressible turbulence. One such study is that by Jagannathan and Donzis [61]. They showed that for solenoidally forced simulations, the normalized total dissipation is similar to that of incompressible turbulence but the normalized dilatational dissipation increases with M_t. The importance of the concept of dissipative anomaly stems from its relation to the phenomena of cascade. While one can speculate about a cascade of energy for the dilatational component of velocity, it is not clear under what conditions this can happen, or if at all. Aluie [2] has argued that despite the dilatational kinetic energy not being a conserved quantity, a cascade is possible for the dilatational kinetic energy provided the pressure dilatation spectrum decays rapidly. A cascade-like behavior for the dilatational kinetic energy has been observed in some numerical simulations at high M_t [8, 143, 146].

The cascade in incompressible turbulence emerges at high Reynolds number, when the large and small scales are well separated that by a wide inertial range. How energy is distributed across this wide range of scales is usually quantified in Fourier space by constructing the energy spectrum which is, thus, a fundamental quantity in studying turbulence. The Kolmogorov theory [70] pre-

dicts a $k^{-5/3}$ scaling in the inertial range for the energy spectrum which has been extensively tested and verified, at least to first order, in numerous studies [28, 51, 104]. The scaling of the dilatational energy spectra, E_{dd}, on the other hand is still not well understood. For example, pseudosound theory [110] predicts a scaling of k^{-3} for the inertial range while EDQNM depending on the damping factor, predicts a scaling of $k^{-11/3}$ and k^{-3} [112]. Pseudosound scaling for spectra was observed in many solenoidally [23, 140] and shear forced [22, 23] DNS at low M_t and excellent collapse of the spectra was observed for these cases. In all these cases, the scaling of the dilatational energy spectra transitions from the pseudosound scaling regime to an acoustic dominated regime. However no satisfactory collapse was seen in the acoustic dominated regime. For cases with more than 50% dilatationally forced DNS simulation, Wang *et al* [144] observed a k^{-2} scaling for the dilatational spectra similar to Burgers turbulence.

A summary of the scaling laws predicted by the theories and that observed in simulations respectively is presented in Table 1.1 and Table 1.2.

Studies of mixing in compressible turbulence have been scare. Some of the few studies available in the literature comprise of 2D flows [78], simulations with shock-capturing schemes which are highly dissipative [18], studies focussed on scalar flux [15] or compressibility effects in mixing [85]. However, the general scope was narrow and confined to a single low value of the Reynolds number. A relatively recent study focused on a comparison to classical incompressible phenomenology [94, 95]. Danish *et al* [27] studied the influence of topology on mixing for conditions where $R_\lambda \approx 20$ and M_t ranging from $0.5 - 0.7$. But none of these studies are adequate in explaining the complex behavior and scaling observed in general situations and range of conditions as seen in Figs. 1.2.

1.3 Objectives of the Present Work

The objectives of the current work are to

1. Build a massive database for compressible turbulence which covers a wide range of forcing conditions and parameter space consisting of the turbulent Mach number, M_t, Taylor

Reynolds Number, R_λ and the new parameter, δ, the ratio of dilatational to solenoidal kinetic energy. This is, to the authors knowledge, among the most comprehensive databases of this kind involving also some of the best resolved simulations available in the literature.

2. Explore the possibility of universality in compressible turbulence which enables or facilitates to discover scaling laws for dilatational statistics in terms of intrinsic turbulent parameters independent of forcing, initial and boundary conditions.

3. Systematically study dissipative anomaly for compressible turbulence and conditions for cascade for the dilatational component of the flow field.

4. Develop theoretical and asymptotic tools to identify different physical regimes and the corresponding scaling of energy spectra. Derive the associated criteria in terms of the governing parameters, M_t and δ to explain some apparent discrepancies in the literature.

5. Study the limitations of classical scaling for compressible turbulent mixing and modify scaling laws to incorporate compressibility effects. Quantify the effects of compressibility on the cascade and small scale features of passive scalars.

6. Develop state-of-the-art computational capabilities and strategies to enable even larger simulations in current and future systems.

2.1 Governing Equations and Simulations

Compressible turbulence dynamics evolves according to the conservation of mass, momentum and energy principles. For a compressible fluid, these can be mathematically formulated as these equations below:

$$\frac{\partial \rho}{\partial t} + \frac{\partial (\rho u_i)}{\partial x_i} = 0 \tag{2.1a}$$

$$\frac{\partial (\rho u_i)}{\partial t} + \frac{\partial (\rho u_i u_j)}{\partial x_j} = -\frac{\partial p}{\partial x_i} + \frac{\partial \sigma_{ij}}{\partial x_j} + \rho f_i \tag{2.1b}$$

$$\frac{\partial (\rho e)}{\partial t} + \frac{\partial (\rho e u_j)}{\partial x_j} = -p\frac{\partial u_i}{\partial x_i} + \frac{\partial}{\partial x_i}\left(\kappa \frac{\partial T}{\partial x_i}\right) + \sigma_{ij} S_{ij} - \wedge \tag{2.1c}$$

with an additional perfect gas equation of state.

$$p = \rho R T \tag{2.1d}$$

where ρ is the density, u_i is the i^{th} component of velocity, p, T, κ, f_i and e correspond to pressure, temperature, thermal conductivity, external forcing and internal energy per unit mass respectively. The $\wedge$ in the energy equation is the rate at which energy is removed from the system so as to maintain a stationary state. More details about $\wedge$ can be found in [61]. The viscous stress tensor and strain rate tensor are defined as

$$\sigma_{ij} = \mu\left(\frac{\partial u_i}{\partial x_j} + \frac{\partial u_j}{\partial x_i} - \frac{2}{3}\delta_{ij}\frac{\partial u_k}{\partial x_k}\right) \tag{2.2a}$$

$$S_{ij} = \frac{1}{2}\left(\frac{\partial u_i}{\partial x_j} + \frac{\partial u_j}{\partial x_i}\right) \tag{2.2b}$$

These equations are numerically solved using 10^{th} order compact schemes in space and the equations are evolved in time using third order Runge-Kutta. More details regarding the numerical

schemes can be found in references [34, 61]. In those studies, only the solenoidal modes were forced whereas in the present study, we extend the study for a range of dilatational forced cases. To accomplish this, we project the Fourier modes of $\underline{f}$ in Eq. 2.1b along the direction of the wavenumber vector, $\underline{k}$, $\left(\widehat{f_{||}}\right)$ and perpendicular to it $\left(\widehat{f_{\perp}}\right)$. These Fourier coefficients follow the independent OU process with a finite time correlation and act only at low wavenumbers inside a spherical shell of radius $k_f \approx 3$.

$$\mathbf{f} = \sum_{|\mathbf{k}|<k_f} (\alpha_p)\, \widehat{\mathbf{f}_{\perp}}\,(\mathbf{k})\, e^{-i\mathbf{k}\cdot\mathbf{x}} + (1-\alpha_p)\, \widehat{\mathbf{f}_{||}}\,(\mathbf{k})\, e^{-i\mathbf{k}\cdot\mathbf{x}} \tag{2.3}$$

The α_p parameter in Eq. 2.3 determine the the relative strength of solenoidal and dilatational forcing. α_p can range from 0 to 1 with 0 and 1 corresponding to the pure dilatational and solenoidal forced scenarios respectively.

The governing equation for passive scalar fluctuations is given as

$$\frac{\partial\left(\rho\phi'\right)}{\partial t} + \frac{\partial\left(\rho\phi' u_i\right)}{\partial x_i} = -\rho u_i \frac{\partial\langle\phi\rangle}{\partial x_i} + \frac{\partial\langle\phi\rangle}{\partial x_i}\frac{\partial D}{\partial T}\frac{\partial T}{\partial x_i} + \frac{\partial}{\partial x_i}\left(D\frac{\partial\phi}{\partial x_i}\right), \tag{2.4}$$

where D is the diffusivity of the scalar. The scalar fluctuations are maintained or sustained by the production mechanism due to a constant mean scalar gradient, $\partial\langle\phi\rangle/\partial x_i$.

2.2 Grid Convergence and DNS Database

In compressible turbulence, apart from the intense dissipative vortex filament structures in incompressible turbulence, previous studies [61, 81, 84, 102, 112, 113, 139, 146] have shown that additional flow structures such as shocklets can be observed in the flow field. These small-scale flow structures can affect the flow statistics and thus high resolutions may be needed to accurately capture it. Shocklets are considered to be small scale highly dilatational flow structures which obeys Rankine-Hugoniot relation similar to a normal shock [81]. Also, these structures are randomly distributed in the flow field. Samtaney [113] showed that for moderate compressibility strength, the most probable shocklet thickness is comparable to Kolmogorov length scale, η. For

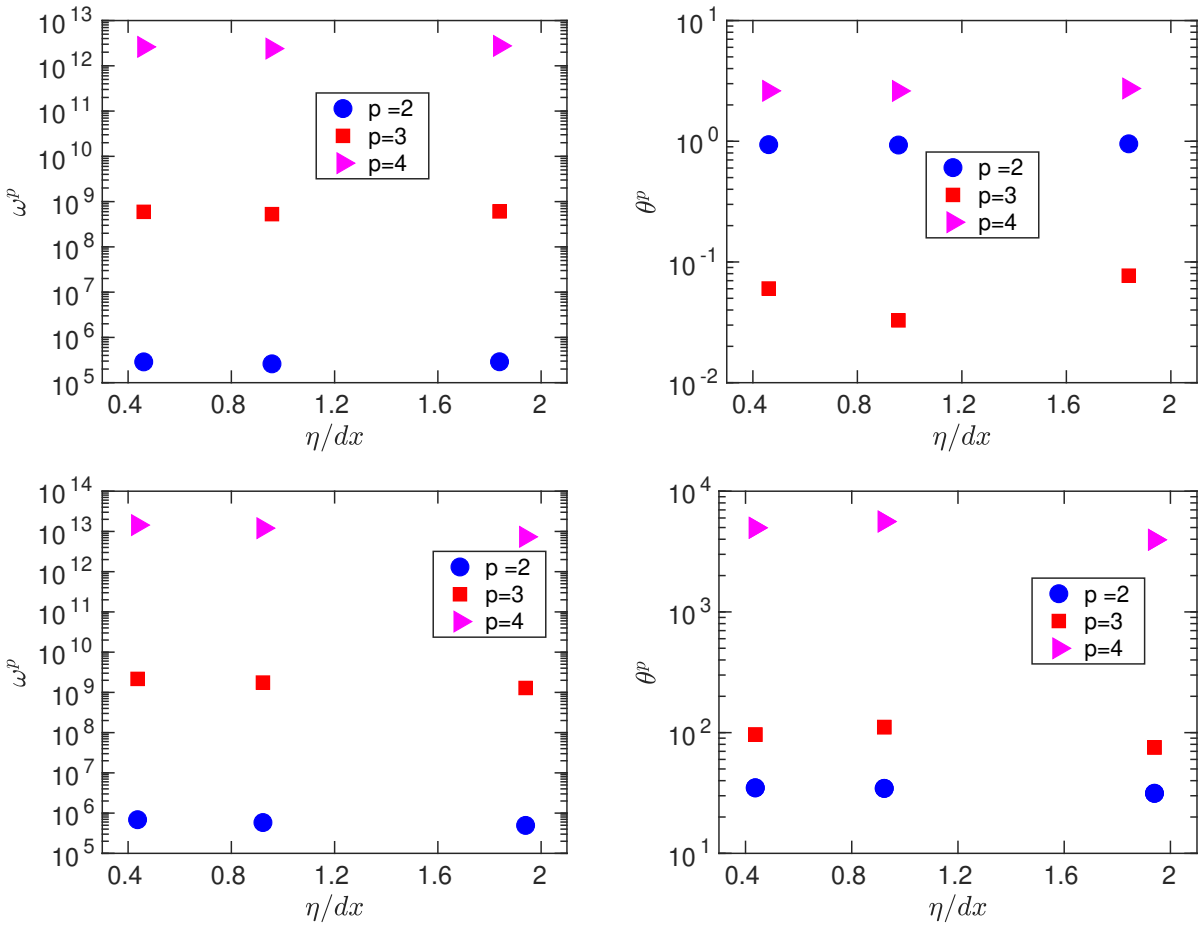

Figure 2.1: Resolution of normalized centralized moments for moderate dilatational forced cases. $(\mu - <\mu>)^p$ when p=2 and $\frac{(\mu-<\mu>)^p}{\left((\mu-<\mu>)^2\right)^{p/2}}$ when p =2,3, where in (a,c) $\mu = \omega$ (vorticity) and (b,d) $\mu = \theta$ (dilatation), 80% solenoidal forcing (a,b) 60% solenoidal forcing (c,d).

$M_t \leq 0.6$, Jagannathan and Donzis [61] showed that $\eta/dx \approx 0.5$ is sufficient to resolve all the small scale features such that higher orders of dissipation up to 4 are adequately converged. Here we extend this convergence studies to dilatational forcing.

We summarize in Figs. 2.1 and 2.2, the grid convergence studies performed under various levels of dilatational forcing. In Fig. 2.1, we plot the moments of small scale quantities, namely enstrophy and dilatation (which are extremely sensitive to grid resolution) for relatively low and moderately dilatationally forced cases.

The same quantities are plotted for highly dilatationally forced cases in Fig. 2.2. We clearly

see from both Figs. 2.1 and 2.2 that even for the highly dilatational forced cases, higher order moments up to 4 seem to converge at $\eta/dx \approx 0.5$. Thus a resolution that satisfies $\eta/dx \approx 0.5$ is adequate for this study as we consider only those statistics whose order is lower than or equal to 4. A more stringent resolution requirement is put forward by previous studies [139, 141, 142] at high M_t due to the formation of shock like structures in the flow field. However, the computational schemes used in their studies are different compared to our current study. For example, they use the more dissipative WENO schemes around the shocklets regimes which might be the probable reason for the more stringent resolution requirement.

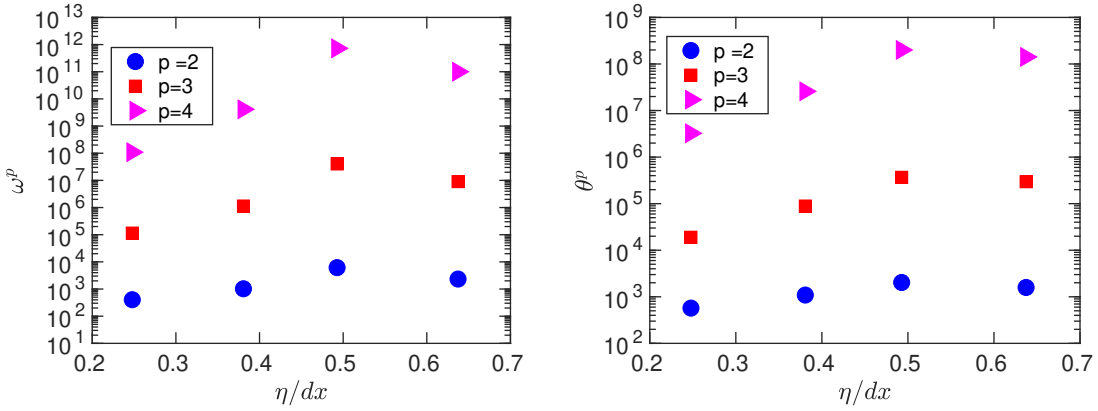

Figure 2.2: Resolution of normalized centralized moments for highly dilatational forced cases. $(\mu - <\mu>)^p$ when p = 2 and $\frac{(\mu-<\mu>)^p}{\left((\mu-<\mu>)^2\right)^{p/2}}$ when p = 2, 3 , where in (a) $\mu = \omega$ (vorticity) and (b) $\mu = \theta$ (dilatation), 10% solenoidal forcing (a,b). θ correspond to the convergence of the small scale compressible motions.

Later we show that shock like structures can be formed in the flow field under dilatational forcing despite low M_t. In fact, we show that criterion for shocklets is both a function of δ as well as M_t. We summarize the current dataset used in this dissertation in Table 2.1.

2.3 Challenges of I/O at Scales

The cDNS code used for direct numerical simulation of compressible turbulence developed in TACL is a highly scalable hybrid code using MPI and OpenMP which can scale to the $O(10^5)$

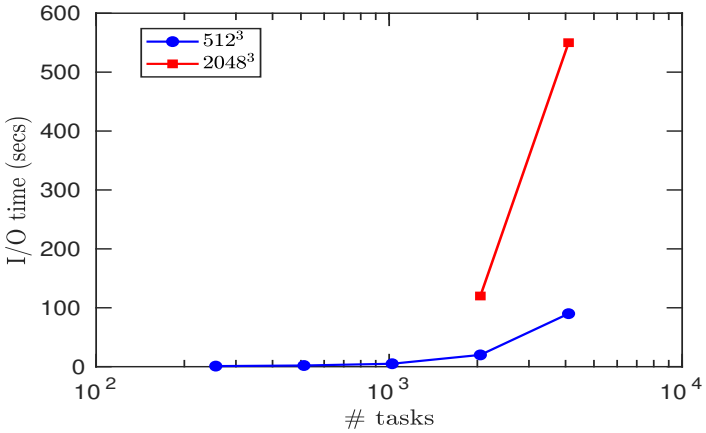

Figure 2.3: Motivation: I/O performance.

cores [60]. One of the main reasons of high scalability is due to the fact that the code implements a 2d pencil like domain decomposition compared to 1d slab decomposition. However the scalability/performance of the code is compromised due to poor or unoptimized I/O performance. And thus I/O is the bottleneck that limits scalability. This can be demonstrated from Fig. 2.3, where we can clearly see that the IO time increases with the number of tasks (# tasks), instead of decreasing or staying constant as required for ideal scaling. Furthermore, the increase becomes substantial when the size of the problem increases.

2.3.1 Lustre File System and MPI I/O

2.3.1.1 Lustre File System

The Lustre file system is one of the popular parallel distributed file system used for large scale computations. The Lustre file system is used in many supercomputers, for example, Stampede2, Frontera, CRAY to name a few. Fig .2.4 illustrates a simplified parallel I/O process using Lustre. Parallel I/O is the simultaneous transfer of data by multiple processors between the compute node, memory and data files on disks. This transfer is managed by Lustre. The major components of a file system can be described as follows:

1. Meta data server (MDS): MDS is responsible for opening and closing the files. It also stores

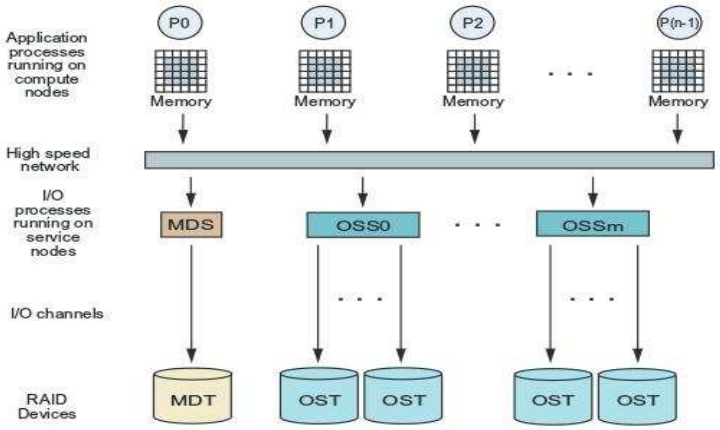

Figure 2.4: Overview of file system. Reprinted from Hadri, introduction to parallel I/O online at *www.nics.tennessee.edu/files/pdf/hpcss13_14/04_08_Parallel_IO_Part1.pdf* [55].

the directory and file metadata such as file ownership, timestamps and access permissions on the meta data target (MDT).

2. Object storage targets (OST): Once a file is created, the compute node processes (P0,P1,....) write data directly into OSTs going thorough object storage servers (OSS) and bypassing the MDS. The OSSs are the physical nodes on which the OSTs are mounted.

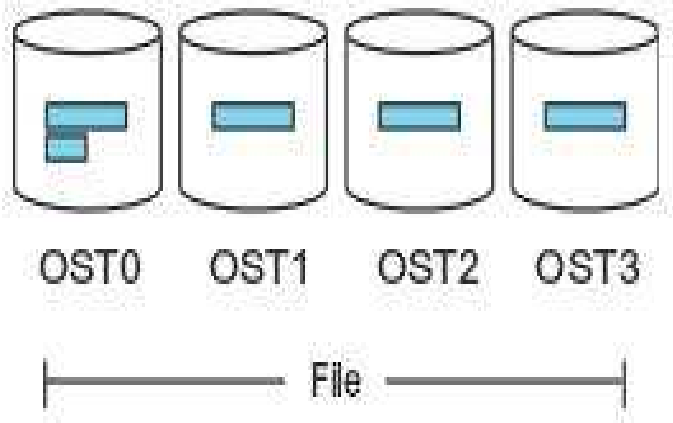

Figure 2.5: Division among OSTs. Reprinted from Hadri, introduction to parallel I/O online at *www.nics.tennessee.edu/files/pdf/hpcss13_14/04_08 _Parallel_IO_Part1.pdf* [55].

Physically a file is distributed among OSTs. In the example shown in Fig.2.5, the file is distributed among four OSTs. This process of distributing a file among multiple OSTs is called file striping. The way in which a file is distributed among the OSTs is done through the parameters known as stripe size and stripe count. File striping is important since it facilitates parallel I/O by physically separating a file's linear sequence of bytes into units called stripes so that the I/O hardware can simultaneously write or read on different stripes. It is important to realize that the file striping can have a major impact on the parallel I/O performance and usually the default values of file parameters are not the optimized values. Since the application code like ours does not have direct access to the physical OSTs or physical I/O blocks, the default values are used unless otherwise specified and thus can result in degraded performance of I/O.

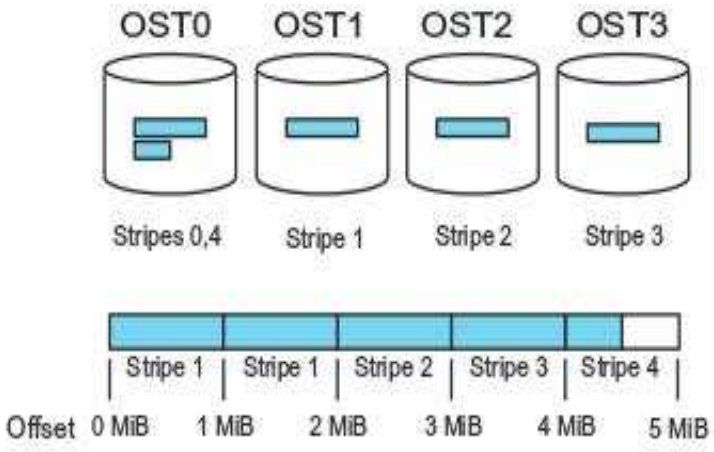

Figure 2.6: A striping example. Reprinted from Hadri, introduction to parallel I/O online at *www.nics.tennessee.edu/files/pdf/hpcss13_14/04_08_Parallel_IO_Part1.pdf* [55].

The parameters can be defined as below :

1. Stripe count: The stripe count is defined as the number of OSTs across which a file is written. As expected, more the number of OSTs , more parallel the writing process, thus better performance. However, the Lustre file system limits the maximum number of OSTs to be 160 (the number of OSTs can be less than 160 for different supercomputer) which is much

less compared to number of cores that are usually used in large scale HPC applications. This will introduce us to another parameter called aggregators and the problem of lock contention which degrades performance. This will be discussed later.

2. Stripe size: The stripe size can be defined as number of bytes written on one OST before cycling to the next. Usually the number of stripes are greater than the number of stripe count if the number of bytes in the file are greater than the product of stripe size and stripe counts.

Fig. 2.6 illustrates how a 5 MB file is distributed among 4 OSTs with a stripe size of 1 MB.

2.3.1.2 MPI I/O

MPI I/O is one of the I/O interface that can be used in a supercomputing system. All MPI applications use such an interface like MPI I/O and Lustre parallel file system to transfer data between the compute node memory and disk files. Before getting into the details of MPI I/O, a few of the strategies that can be used in Parallel I/O for better performance will be discussed.

1. One file per process, all write: In this strategy, all the processors write its own file. This strategy is already implemented in cDNS and mpi2d. Although this strategy works well for small number of processors, we wont be considering this strategy due to the following reasons.

    - All file metadata will reside on a single MDT creating problems for both application and file system
    - This does not scale well when the ratio of the number of cores to the OSTs available is large and usually, this is the case for large scale computations.
    - Too many files makes post processing difficult and if any one of the files among many files become corrupt, the entire flow field or output becomes useless.

      Such a strategy will not be viable for exascale computations.

2. Single shared file, one write : In this strategy, all cores transfer data to just one core which

does the writing. This is essentially a sequential process and thus for large scale computing, this strategy is not recommended.

3. Single shared file, all write/subset write : In this strategy, a single file is written and either all the cores involved in the application write simultaneously to the file or a subset of cores known as aggregators write to the common file. It might seem that the highest performance is obtained when all the cores participate in writing. But however due to the limited number of OSTs available in the Lustre file system, a large number of processors will be competing for the same OST which is called lock contention. This essentially serialize the writing process.

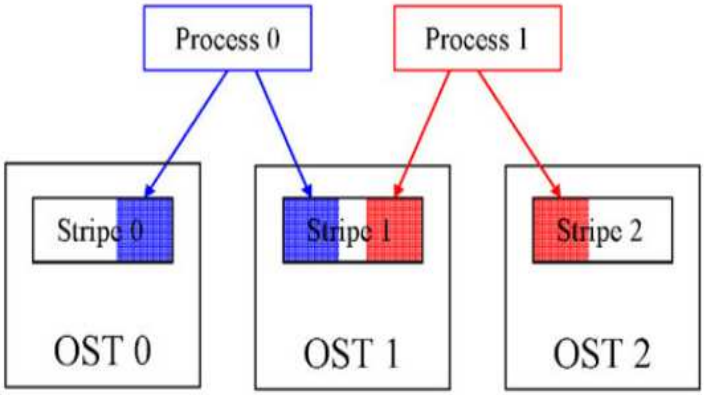

Figure 2.7: Stripe non-alignment. Reprinted from Logan and Dickens, towards an understanding of the performance of MPI-IO in Lustre file systems, 2008 IEEE international conference on cluster computing, Tsukuba, Japan. [86]

One of the ways to alleviate this locking contention is to transfer the data in all cores to a subset of cores known as aggregators which does the writing to the file. However, locking contention can still occur when stripe boundary is not aligned with OST boundary. Such a scenario is illustrated in Fig. 2.7, where each processor is trying to write to stripe 1 which is spread across two OSTs. Because of Lustre's locking protocol, each process must acquire the lock associated with the stripe which results in serializing the writing procedure [86]. Of course this problem occurs

when all processors write too. It should be noted that this locking problem can be removed by judiciously setting the no of aggregators, stripe count and stripe size which will be discussed in the optimization strategy section. MPI I/O provides two types of I/O calls:

1. Independent I/O call: Independent MPI I/O calls are referred to as independent because the calls can be made by any subset of the processors participating in the I/O, with each processor handling its own I/O independently. One of the advantage of this I/O is that no communication overhead is involved when all the processors are involved which is the case in collective I/O discussed next. But the major disadvantage is that this results in a lot of MPI I/O calls by each processor which can result in a lot of overheads and the fact that the data to be written is small compared to collective I/O, the entire process will be dominated by latency just as in normal communication.

2. Collective I/O call: In collective I/O, all processors in the communicator must make a single I/O call. With the collective I/O, MPI I/O uses a two phase process called collective buffering [132] where in the first step all processors transfer data to some selected processors called aggregators. And after the consolidation and transfer, only the aggregators perform the actual I/O. The number of aggregators by default are the number of OSTs available. The advantage of choosing the aggregators equal to the OSTs available is that it can reduce lock contention but however it does not make sure that it is stripe aligned. Furthermore, there is an overhead associated with the redistribution of data from all processors to the aggregators.

2.3.2 Current Optimization Strategies Implemented in cDNS

Currently there are three implementations of I/O in cDNS as listed below

1. The one in which all processors write its own file: As discussed earlier, this implementation does not suit large scale applications.

2. Collective I/O implementation: However, it was found that the performance was not good, probably due to large communications involved in transferring data from all processors to

aggregators. But this might only be a minor issue, the major problem is due to locking because of stripe non-alignment across the OSTs. This is primarily because the parameters are not optimized.

3. Independent I/O implementation: To reduce locking, the writing operations are done in batches (only a few cores are allowed to write at once). Although this seems to work better than unoptimized collective I/O, this is not a really good solution since it serializes the I/O process.

2.3.3 Optimization Strategy

It has been a well known fact that MPI I/O does not perform well in the Lustre file systems and the reason is mainly due to the Lustre's locking protocol when stripes are not aligned with the OST boundary. This problem could be avoided if we can judiciously choose the parameters in a way the stripes always align with the OST boundary. Thus the main strategy would be to avoid the stripe non-alignment. The advantage is that the code development efforts are minimal. To reiterate, the main parameters that need to be tuned for better optimization in the code are

1. Stripe count (SC): As discussed earlier, the stripe count is equal to the number of OSTs available. Intuitively, in order to have maximum parallelism, the stripe count should be set to the maximum allowable limit permitted by various supercomputers. For example, the maximum limit is 32 for stampede2 as well as for the scratch3 file system in Frontera.

2. No of aggregators (NA): In collective MPI I/O, we have seen that the only a subset of processors known as aggregators does the I/O. Now the minimum number of aggregators should be set to stripe count in order utilize all the resources available. Now setting to this minimum implies that there will be no locking contention issues, hence the major overhead will be the data transfer from all processors to aggregators. This could be huge when there are a large number of cores. However, when we increase the number of aggregators, we decrease the communication time but increase locking, since in such a case two or more processors will be competing for the same OST.

3. Stripe Size (SS): The stripe size can be chosen to avoid stripe alignment and decrease locking by the simple formula given below

$$SS = \frac{N^3 * 8}{NA * 1024 * 1024} \text{ in MB} , \tag{2.5}$$

where N is the number of grid points along each direction, 8 is the size of the double precision variable and (1024*1024) is the factor to convert bytes to MB.

The benchmark studies on various supercomputers were done and found to increase the performance.

2.4 General Purpose GPU Computing

The use of graphics processing units (GPU) for general-purpose scientific computing is known as GPGPU. The GPUs are highly parallel architectures compared to CPUs, for example, a Tesla K20X has 2688 cores compared to modern CPUs with a few to tens of cores. The adaptation of GPUs for general purpose scientific computing has been challenging due to the difficulties in programming the application programming interface (API) [111]. This changed when NVIDIA introduced CUDA architecture in 2007 with both hardware and software support. The new software environment or programming model, “CUDA C" is simple with few extensions to the programming language “C" which enables offloading certain regions of code to run on GPUs.

Despite some of the shortcomings of the GPGPU programming model, for example the bottleneck of transferring the data between the GPUs and CPUs, GPGPU is becoming increasingly popular. This is evident, since as of November 2019, half of the ten fastest supercomputers in the top 500 list are GPU powered and most of the upcoming Department of energy (DOE) machines such as Aurora, Frontier, El Capitan are based on GPU architectures. Researchers have started using GPUs for turbulence simulations. Clay *et al.* [25] reported the successful GPU implementation of their DNS code for high Schmidt number simulations. They achieved asynchronous computations of the coarse grid velocity and fine grid scalar fields in CPUs and GPUs respectively. More recently, Kiran *et al.* [109] implemented the entire pseudo spectral DNS code on GPUs. The

benchmark studies on Summit showed a speed up of 4.7 for a 12288^3 grid compared to CPUs alone.

In 2009, Portland group Inc (PGI) and NVIDIA jointly introduced CUDA-Fortran compiler which helped Fortran users to leverage the computational power of GPUs. Apart from high level programming paradigms such as CUDA and CUDA-Fortran, one can also use directive based OPENACC and OpenMP to offload computations to GPUs. More details and an introduction on GPU implementation can be found in references [46, 111]. We present in this section some initial results of our efforts to port some portions of cDNS to GPUs. We use the directive based OPENACC. We have ported some computationally intensive regions of cDNS for a single core.

2.4.1 Preliminary Benchmark Results

The in house cDNS code is a highly scalable parallel solver of compressible Navier-Stokes equations. The scalability has been demonstrated on various supercomputers such as Stampede2, Frontera to name a few. Fig. 2.8 shows the strong scaling of the cDNS code. It shows that the code is scalable up to 431200 cores, almost the entire Frontera machine. The cDNS code consists of three parts

1. Evolution of flow variables using RK3 time stepping

2. Evaluation of the spatial derivatives and thus assembly of rhs of the governing Navier-Stokes

3. Addition of an artificial stochastic forcing to the rhs thus sustaining turbulence.

The code is parallelized using MPI and the domain is decomposed into 2d pencils. Details regarding the parallel implementation can be found in [59, 60]. The parallel implementation introduces additional bottleneck which is the extra time required for communications among the processors. The scalability is lost when the time taken for communications exceed that of computations. In the absence of communications, the time required for the algorithm is thus directly proportional to the number of computations. The number of flops per grid and number of time steps can be estimated as the measure of the time taken to complete the algorithm. Using PAPI,

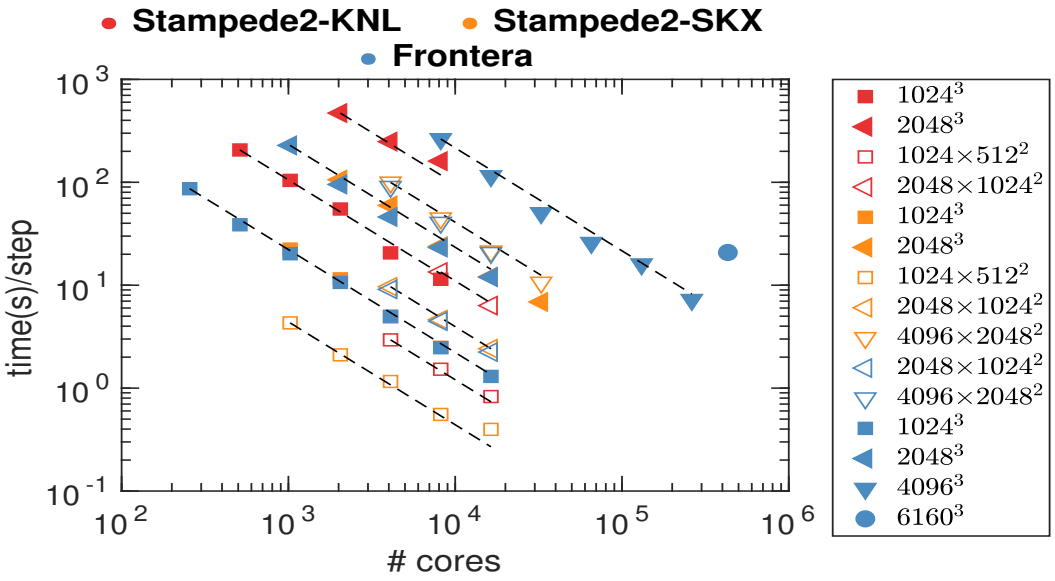

Figure 2.8: Strong scaling of cDNS.

after a number of benchmarks at various grid sizes, we estimate the flops/grid for a single time step as

- With forcing: flops/grid ≈ 35640
- With no forcing: flops/grid ≈ 9321.

Thus in the absence of communications, forcing subroutine takes around 75 % of the total time required for the program.

Since forcing is the most computationally intensive region of the code and is independent of other regions of the code, it is an ideal candidate to send to GPUs. To evaluate the viability of GPUs for cDNS, we implement a GPU implementation of the code for a single core where we perform the calculations in the forcing subroutine in a single GPU. The major bottleneck is the transfer of data from CPUs and GPUs and hence, in our implementation, we optimized the data transfer. The transfer from CPU to GPU is avoided by creating the forcing array inside the GPU,

whereas after the computations in the GPU, forcing array in the CPU is updated which involves transfer of data from GPU. Moreover in the CPU only version of the cDNS, the spatial derivatives in the rhs of the Navier-Stokes are computed and assembled together before the forcing term is calculated and added. However in the GPU implementation, the calculations of forcing and rhs are computed inside the GPU and CPU simultaneously thus achieving asynchronous computations in both architectures, thus speeding up the code. The benchmark studies are done on NVIDIA Tesla K20 GPUs of the terra supercomputer of the Texas A & M University high performance computing facility.

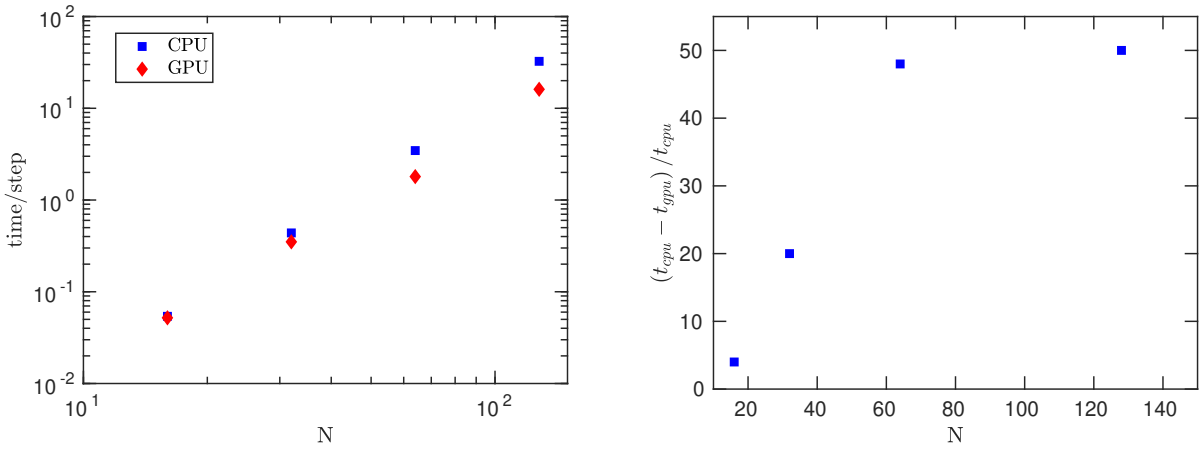

Figure 2.9: (a) Time per step for CPU and GPU. (b) Percentage speed up for GPU.

Fig. 2.9 (a) shows the time per step for CPU and GPU on a single core. One finds that as the grid size increases, the performance of the GPU relative to CPU increases. We plot the percentage of speed up for GPU in Fig. 2.9 (b). The percentage speed at $N = 16$ is negligible at around 4%. At this low grid number, the computations inside the GPU are lean to overcome the time taken for the data transfer between CPU and GPU. But as the grid size increases, the speed up also increases and ultimately reaches an asymptote of a 50 % speed up. At these high N, there is enough computations in the GPU to overcome the data transfer bottleneck. In summary, we were able to port computationally intensive forcing subroutine to the GPU for a single core and achieve a 50

% speed up at high grid size. We believe that extending the code development to multi-processor combining MPI and OPENACC will be beneficial at a higher gird size where the computations in the GPUs are high enough to counter the constraints due to data transfer involving multiple CPUs in addition to that between CPU and GPU.

N	α_p	Re_λ	M_t	δ	χ	η/dx
32	1.0	9	0.066	0.002	≈ 0	0.7986
32	1.0	8	0.144	0.007	≈ 0	0.8999
32	1.0	8	0.204	0.033	0.001	0.8324
32	1.0	11	0.643	0.198	0.038	0.6473
64	1.0	31	0.198	0.015	≈ 0	0.578
64	1.0	36	0.089	0.004	≈ 0	0.481
64	1.0	35	0.311	0.067	0.005	0.475
64	1.0	39	0.102	0.004	≈ 0	0.480
64	1.0	31	0.200	0.014	≈ 0	0.576
64	1.0	34	0.285	0.056	0.003	0.512
64	1.0	37	0.706	0.232	0.051	0.450
128	1.0	58	0.093	0.003	≈ 0	0.540
128	1.0	53	0.230	0.032	0.001	0.613
128	1.0	57	0.270	0.066	0.004	0.554
128	1.0	61	0.344	0.111	0.012	0.507
128	1.0	59	0.600	0.210	0.042	0.522
128	0.9	60	0.083	0.057	0.003	0.524
128	0.9	63	0.323	0.174	0.030	0.492
128	0.9	59	0.519	0.231	0.051	0.526
128	0.8	36	0.112	0.086	0.007	0.956
128	0.8	34	0.640	0.271	0.069	0.960
128	0.8	35	0.790	0.313	0.089	0.859
128	0.6	56	0.134	0.343	0.105	0.587
128	0.6	38	0.143	0.324	0.095	0.923
128	0.6	60	0.301	0.330	0.098	0.521
128	0.6	53	0.557	0.343	0.105	0.547
256	1.0	101	0.213	0.016	≈ 0	0.507
256	1.0	102	0.324	0.071	0.005	0.494
256	1.0	103	0.360	0.097	0.009	0.497
256	1.0	97	0.593	0.207	0.041	0.535
256	0.9	97	0.206	0.124	0.015	0.554
256	0.9	106	0.317	0.177	0.030	0.484
256	0.9	100	0.473	0.227	0.049	0.524
256	0.8	96	0.192	0.165	0.026	0.553
256	0.8	100	0.351	0.202	0.039	0.531
256	0.8	100	0.437	0.219	0.046	0.527
256	0.6	104	0.221	0.347	0.107	0.508
256	0.6	98	0.332	0.333	0.100	0.529
256	0.5	59	0.065	0.631	0.285	1.036

Table 2.1: Current DNS database

N	α_p	Re_λ	M_t	δ	χ	η/dx
256	0.5	59	0.201	0.513	0.208	0.915
256	0.4	53	0.052	1.016	0.508	0.956
256	0.4	51	0.254	0.824	0.404	0.702
256	0.3	51	0.063	1.644	0.730	0.704
256	0.3	50	0.204	1.399	0.662	0.496
256	0.3	64	0.117	1.456	0.680	0.465
256	0.2	51	0.061	1.655	0.732	0.703
256	0.1	36	0.100	3.810	0.936	0.636
256	0.1	33	0.053	5.447	0.967	0.857
256	0.1	44	0.147	2.805	0.887	0.490
512	1.0	166	0.202	0.015	≈ 0	0.495
512	1.0	158	0.296	0.045	0.002	0.526
512	1.0	159	0.356	0.072	0.005	0.519
512	1.0	141	0.476	0.174	0.029	0.627
512	1.0	158	0.603	0.198	0.038	0.548
512	0.9	146	0.185	0.142	0.020	0.617
512	0.9	157	0.268	0.183	0.033	0.573
512	0.6	136	0.049	0.364	0.117	0.745
512	0.6	141	0.085	0.412	0.145	0.714
512	0.6	144	0.181	0.356	0.113	0.643
512	0.6	141	0.245	0.323	0.094	0.617
512	0.4	103	0.041	0.995	0.497	0.924
512	0.3	75	0.21	1.369	0.652	0.597
1024	1.0	268	0.325	0.0454	0.002	0.496
1024	1.0	240	0.427	0.1947	0.037	0.670
2048	1.0	430	0.308	0.0303	0.001	0.525

Table 2.1 Continued

3. ASYMPTOTIC ANALYSIS OF COMPRESSIBLE NAVIER-STOKES EQUATION

3.1 Decomposition of Velocity Field

Compressible turbulence as we discussed before has extra physical modes such as acoustic and entropy modes in addition to the vortical mode in the velocity field. The acoustic and entropy modes represent the compressibility physics. Thus to access the compressibility effects on the flow field, one has to compare the relative magnitude of these modes as well as the interactions between them. However, for any arbitrary flow field, especially when modes strongly interact due to non-linearity in the system, it is impossible to isolate and analyze the modes independently [112]. Thus it is common in literature to isolate the compressibility effects using Helmholtz decomposition. For a homogeneous flow field such as the one we are considering in this study, it is possible to decompose the velocity into solenoidal and dilatational components exactly at any instant where the solenoidal and dilatatonal velocities satisfy the below equations,

$$\nabla \cdot \mathbf{u}^s = 0, \tag{3.1a}$$

$$\nabla \times \mathbf{u}^d = 0, \tag{3.1b}$$

respectively. The solenoidal and dilatational modes represent the incompressible and compressible physics respectively. Thus one can study compressibility effects by estimating the relative magnitude of these modes and their interactions as a function of the governing parameters (R_λ, M_t, δ). Next, we derive the equations for the solenoidal and dilatational kinetic energy.

3.2 Governing Equations of Solenoidal and Dilatational Kinetic Energy

Before we proceed to the asymptotic analysis, we derive the kinetic energy budget equations to understand the processes which are important at different conditions. We follow Kida and Orzag [65, 66] by defining $\varpi_i = \sqrt{\rho} u_i$. Therefore, now $\langle \varpi_i \varpi_i \rangle / 2$ is the turbulent kinetic energy. By writing the energy equations in terms of ϖ_i rather than $\mathbf{u}$ helps to partially incorporate the effect

of density fluctuations. The Navier-Stokes therefore can be rearranged as

$$\frac{\partial \varpi_i}{\partial t} + u_j \frac{\partial \varpi_i}{\partial x_j} - \frac{1}{2}\varpi_i \frac{\partial u_j}{\partial x_j} = \frac{-1}{\sqrt{\rho}} \frac{\partial p}{\partial x_i} + \frac{1}{\sqrt{\rho}} \frac{\partial \sigma_{ij}}{\partial x_j} + \sqrt{\rho} f_i \tag{3.2}$$

We introduce some notations before we derive the kinetic energy equations from above Navier-Stokes equation. The Fourier transform of any vector $\mathbf{B}$ is given below:

$$\widehat{\mathbf{B}}(\mathbf{k}) = \iiint \mathbf{B}(\mathbf{x})\, e^{-\mathbf{k}\cdot\mathbf{x}} d\mathbf{x} \tag{3.3}$$

We can decompose the Fourier modes into a solenoidal (perpendicular to $\mathbf{k}$) and dilatational (parallel to $\mathbf{k}$) component. They are denoted respectively as

$$\{\widehat{\mathbf{B}}\}^s(\mathbf{k}) = \mathbf{B}(\mathbf{k}) - \frac{\mathbf{k}}{k^2}\left(\mathbf{k}\cdot\widehat{\mathbf{B}}\right) \tag{3.4a}$$

$$\{\widehat{\mathbf{B}}\}^d(\mathbf{k}) = \frac{\mathbf{k}}{k^2}\left(\mathbf{k}\cdot\widehat{\mathbf{B}}\right). \tag{3.4b}$$

We can estimate the spatial average of the product of two terms by using Parseval theorem by summing the product of Fourier coefficients in $\underline{\mathrm{k}}$ space. Thus the spatial average can be represented by the notation below:

$$\langle \widehat{\mathbf{B}}^\alpha \rangle_k = \frac{1}{(2\pi)^3} \iiint \widehat{\mathbf{B}}^\alpha(\mathbf{k}) d\mathbf{k}. \tag{3.5}$$

Here "α" corresponds to the solenoidal ("s") and dilatational ("d") directions.

We follow the procedure in Miura and Kida [91] to derive the spatially averaged solenoidal and dilatational energy equations. We first transform the Navier-Stokes equations to the Fourier space. Projecting the Fourier transformed Navier-Stokes in the directions parallel and perpendicular to wavenumber vector gives the dilatational and solenoidal contributions. After taking the dot product of the Navier-Stokes in the wavenumber space with the complex conjugate of the Fourier transformed ϖ^s $(\widehat{\varpi}^{*s})$ and ϖ^d $\left(\widehat{\varpi}^{*d}\right)$ and summing over the entire wavenumbers, we have the av-

eraged solenoidal and dilatational kinetic energy equations respectively. The reader is referred to [91] for further details. The results are

$$\frac{dE_s}{dt} = A_s + A_{c1} + A_{c2} + P_s + D_s + F_s \tag{3.6a}$$

$$\frac{dE_d}{dt} = A_d + A_{c3} + A_{c4} + P_d + D_d + F_d \tag{3.6b}$$

where

$$E_s = \langle \varpi_i^s \varpi_i^s \rangle,\ E_d = \langle \varpi_i^d \varpi_i^d \rangle \tag{3.7a}$$

$$A_s = \Big\langle \widehat{\varpi}_i^s \Big\{ u_j^s \widehat{\frac{\partial w_i^s}{\partial x_j}} \Big\}^s \Big\rangle_k \tag{3.7b}$$

$$A_{c1} = \Big\langle \widehat{\varpi}_i^s \Big\{ u_j^d \widehat{\frac{\partial w_i^s}{\partial x_j}} + u_j^s \widehat{\frac{\partial \varpi_i^d}{\partial x_j}} - \frac{1}{2} \varpi_i^s \widehat{\frac{\partial u_j^d}{\partial x_j}} \Big\}^s \Big\rangle_k \tag{3.7c}$$

$$A_{c2} = \Big\langle \widehat{w_i}^s \Big\{ u_j^d \widehat{\frac{\partial \varpi_i^d}{\partial x_j}} - \frac{1}{2} \varpi_i^d \widehat{\frac{\partial u_j^d}{\partial x_j}} \Big\}^s \Big\rangle_k \tag{3.7d}$$

$$A_{c3} = \Big\langle \widehat{\varpi}_i^d \Big\{ u_j^s \widehat{\frac{\partial w_i^s}{\partial x_j}} \Big\}^d \Big\rangle_k \tag{3.7e}$$

$$A_{c4} = \Big\langle \widehat{\varpi}_i^d \Big\{ u_j^d \widehat{\frac{\partial \varpi_i^s}{\partial x_j}} + u_j^s \widehat{\frac{\partial \varpi_i^d}{\partial x_j}} - \frac{1}{2} \varpi_i^s \widehat{\frac{u_j^d}{x_j}} \Big\}^d \Big\rangle_k \tag{3.7f}$$

$$A_d = \Big\langle \widehat{\varpi}_i^d \Big\{ u_j^d \widehat{\frac{\partial w_i^d}{\partial x_j}} - \frac{1}{2} \varpi_i^d \widehat{\frac{u_j^d}{x_j}} \Big\}^d \Big\rangle_k \tag{3.7g}$$

$$P_s = \Big\langle -\widehat{\varpi}_i^s \Big\{ \widehat{\frac{1}{\sqrt{\rho}} \frac{\partial p}{\partial x_i}} \Big\}^s \Big\rangle_k,\ P_d = \Big\langle -\widehat{\varpi}_i^d \Big\{ \widehat{\frac{1}{\sqrt{\rho}} \frac{\partial p}{\partial x_i}} \Big\}^d \Big\rangle_k \tag{3.7h}$$

$$\epsilon_s = \Big\langle \widehat{\varpi}_i^s \Big\{ \frac{1}{\sqrt{\rho}} \widehat{\frac{\partial}{\partial x_j}} \frac{\partial u_i^s}{\partial x_j} + \frac{1}{\sqrt{\rho}} \widehat{\frac{\partial}{\partial x_j}} \frac{\partial u_j^s}{\partial x_i} \Big\}^s \Big\rangle_k \tag{3.7i}$$

$$\epsilon_d = \Big\langle \widehat{\varpi}_i^d \Big\{ \frac{1}{\sqrt{\rho}} \widehat{\frac{\partial}{\partial x_j}} \frac{\partial u_i^s}{\partial x_j} + \frac{1}{\sqrt{\rho}} \widehat{\frac{\partial}{\partial x_j}} \frac{\partial u_j^s}{\partial x_i} - \frac{2}{3} \frac{1}{\sqrt{\rho}} \widehat{\frac{\partial}{\partial x_j}} \frac{\partial u_k^d}{\partial x_k} \Big\}^d \Big\rangle_k \tag{3.7j}$$

$$F_s = \langle \widehat{\varpi}_i^s \{ \widehat{f}_i \}^s \rangle_k,\ F_d = \langle \widehat{\varpi}_i^d \{ \widehat{f}_i \}^d \rangle_k \tag{3.7k}$$

In compressible turbulence, the advection term in the energy budget has been subjected to many studies [65, 66, 143]. But in those studies, these advection terms were not decomposed into components to understand the strength of interaction among modes. In this study, the advection term is decomposed based on the strength of interactions among the solenoidal and dilatational modes in the kinetic energy equations. The two modes can interact through the cross advection terms, $A_{c1}, A_{c2}, A_{c3}, A_{c4}$. In general, the individual average of the cross advection terms need not be same but rather the average of the summation is zero $(\langle A_{c1} + A_{c2} + A_{c3} + A_{c4} \rangle = 0)$.

3.3 Two Parameter Expansion: Asymptotic Analysis

We now introduce the novel asymptotic analysis in terms of two compressible parameters, the turbulent Mach number (M_t) and the ratio of dilatational to solenoidal velocity rms (δ). A number of perturbation analyses [10, 43, 118, 158] have been done using M_t as the sole parameter which can simplify the complex governing equation to such an extent that it was possible to put forward specific theoretical predictions such as equipartition [118] and pseudosound [110]. However, under these framework, we are not able to explain some of the observations under general conditions of forcing in compressible turbulence. In all these studies, M_t was used as a measure of both compressibility strength and scale separation. We recently [35] showed that the strength of compressibility in the flow field has to be explicitly taken into account through $\delta = u'^d/u'^s$. In order to develop the two parameter expansion, the order of magnitude of the solenoidal part of the velocity is taken as $O(1)$ and that of dilatational part to be $O(\delta)$. In our study, δ ranges from $O(10^{-4})$ to $O(10)$. Thus total velocity is written as

$$\mathbf{u} = \mathbf{v^s} + \delta \mathbf{v^d}, \tag{3.8}$$

where both v^s and v^d have an $O(1)$ and correspond to the solenoidal and dilatational components respectively. Similarly, the order of magnitude of ϖ is assumed to be same as $\mathbf{u}$. This ϖ is written as

$$\varpi = \mathbf{w^s} + \delta \mathbf{w^d}. \tag{3.9}$$

This greatly simplifies the analysis. This is supported by our DNS data as seen in Fig. 3.1 for the range of conditions considered in this study.

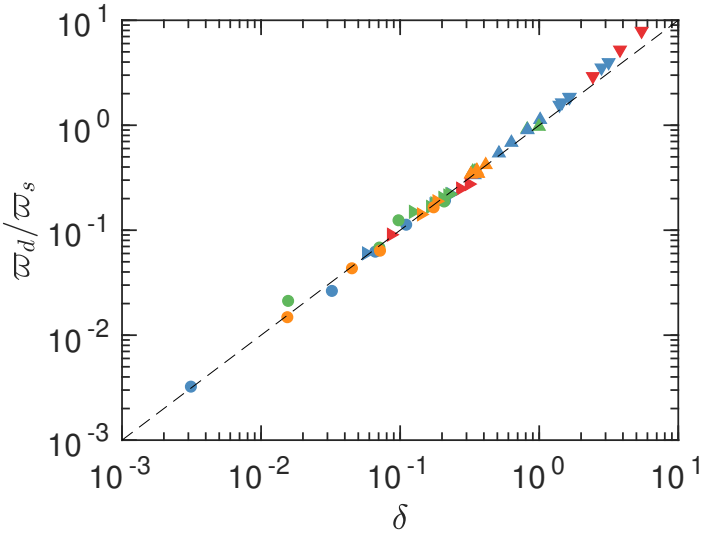

Figure 3.1: Scaling of ϖ'_d/ϖ'_s with δ.

The acoustic and turbulent time scales are well separated when $M_t \ll 1$ [118]. Similar to Zank and Matthaeus [158], we introduce two independent time scales separated by the turbulent Mach number, M_t. Thus the total time derivatives can be expanded as a combination of slow $(\tau = t)$ and fast $(\tau' = t/M_t)$ time scales as below:

$$\frac{\partial}{\partial t} = \frac{\partial}{\partial \tau} + \frac{1}{M_t}\frac{\partial}{\partial \tau'} \tag{3.10}$$

Similarly, we can separate the spatial length scales when $M_t \ll 1$:

$$\nabla = \nabla_\eta + M_t \nabla_\xi. \tag{3.11}$$

Here $\eta = x$ and $\xi = M_t x$ are waves corresponding to small and large wavelength respectively.

Since the behavior of solenoidal and dilatational pressure are different, it is important to distinguish the contributions from the solenoidal and dilatational pressure. In Zank and Matthaeus' study, they assume the same order of magnitude ($O\left(M_t^2\right)$) for both solenoidal and dilatational pressure. We recently [35] showed that $p_d/p_s = \delta\sqrt{\delta^2+1}/M_t$. Using the asymptotic limits, at low and high δ of this relation, we can define the total pressure as

$$P = P_o + O\left(M_t^2\right) p_s + O\left(\delta M_t, \delta^2 M_t\right) p_d. \tag{3.12}$$

This general expression reduces to the $O\left(M_t^2\right)$ when the dilatational contributions are neglected. We follow the non-dimensionalization used in Zank and Matthaeus:

$$\bar{p} = p_* \frac{L}{\nu u_o}; u = \frac{u^*}{u_o}; \bar{\rho} = \frac{\rho^*}{\rho_o} \tag{3.13a}$$

$$t = \left(\frac{u_o^2}{\nu}\right) t^*; x = \left(\frac{u_o}{\nu}\right) x^*, \tag{3.13b}$$

where the starred quantities are the dimensional variables and ones with subscript "o" correspond to some reference value. In this case, u_o and ρ_o would correspond to rms velocity, u' and mean density, $\langle\rho\rangle$. After non-dimensionalization, the Navier-Stokes momentum equations are

$$\bar{\rho}\frac{\partial u_i}{\partial t} + \bar{\rho} u_j \frac{\partial u_i}{\partial x_j} = \frac{-1}{\gamma M_t^2}\frac{\partial \bar{p}}{\partial x_i} + \frac{\partial \sigma_{ij}}{\partial x_j}, \tag{3.14a}$$

where

$$\sigma_{ij} = \left(\frac{\partial u_i}{\partial x_j} + \frac{\partial u_j}{\partial x_i} - \frac{2}{3}\delta_{ij}\frac{u_k}{x_k}\right). \tag{3.14b}$$

The non-dimensionalized Navier-Stokes in terms of ϖ is

$$\frac{\partial \varpi_i}{\partial t} + u_j \frac{\partial \varpi_i}{\partial x_j} + \frac{1}{2}\varpi_i \frac{\partial u_j}{\partial x_j} = \left(\frac{-1}{\gamma M_t^2}\right)\frac{1}{\sqrt{\bar{\rho}}}\frac{\partial \bar{p}}{\partial x_i} + \frac{1}{\sqrt{\bar{\rho}}}\frac{\partial}{x_j}\left(\frac{\partial u_i}{\partial x_j} + \frac{\partial u_j}{\partial x_i} - \frac{2}{3}\delta_{ij}\frac{\partial u_k}{\partial x_k}\right). \tag{3.15}$$

We first start with density which appears as $\sqrt{\rho}$ in the above equation to construct the order of magnitude of the terms in this equation. We can decompose the total density into a mean and

a fluctuating part: $\bar{\rho} = 1 + \rho'^{*}/\langle\rho\rangle = 1 + \rho'$. We can relate the density and pressure fluctuations through an isentropic or polytropic process where $\rho' = p'^{\gamma}$ in a number of situations. This was observed in shear flows [14] although at high M_t [144], there are some slight deviations. This assumption is justified from an order of magnitude analysis. We can write the order of magnitude of the density term appearing on the RHS as

$$O\left(\sqrt{\bar{\rho}}\right) = O\left(\sqrt{1+\rho'}\right) \approx O\left(\sqrt{1+M_t^{2/\gamma}}\right), O\left(\sqrt{1+(\delta M_t)^{1/\gamma}}\right), O\left(\sqrt{1+(\delta^2 M_t)^{1/\gamma}}\right), \tag{3.16a}$$

depending on which mode of pressure dominates the flow field. The order of magnitude of density term in the Eq. 3.15 is

$$O\left(\sqrt{\bar{\rho}}\right) = O\left(1\right), \tag{3.16b}$$

for the range of δ and M_t in our current study.

We can substitute Eq. 3.8 to Eq. 3.12 and Eq. 3.16b into Eq. 3.15, we match the expansions in terms of the power laws in the two different parameters δ and M_t. This exercise leads to ten equations. We start to analyze just the lower order terms and the higher order terms are included in the appendix A for completeness.

$$O\left(1\right) : \frac{\partial w_i^s}{\partial \tau} + v_j^s \frac{\partial w_i^s}{\partial \eta_j} = -\frac{1}{\sqrt{\rho}}\frac{\partial p^s}{\partial \eta_i} + \frac{1}{\sqrt{\rho}}\left(\frac{\partial}{\partial \eta_j}\frac{\partial v_i^s}{\partial \eta_j} + \frac{\partial}{\partial \eta_j}\frac{\partial v_j^s}{\partial \eta_i}\right) \tag{3.17a}$$

$$O\left(\frac{1}{M_t}\right) : \frac{\partial w_i^s}{\partial \tau'} = 0 \tag{3.17b}$$

$$O\left(\delta\right) : \frac{\partial w_i^d}{\partial \tau} + v_j^d \frac{\partial w_i^s}{\partial \eta_j} + v_j^s \frac{\partial w_i^d}{\partial \eta_j} + w_i^s \frac{\partial v_j^d}{\partial \eta_j} = -\frac{1}{\sqrt{\rho}}\frac{\partial p^d}{\partial \xi_i} + \frac{1}{\sqrt{\rho}}\left(\frac{\partial}{\partial \eta_j}\frac{\partial v_i^d}{\partial \eta_j} + \frac{\partial}{\partial \eta_j}\frac{\partial v_j^d}{\partial \eta_i} + \frac{\partial}{\partial \eta_i}\frac{\partial v_j^d}{\partial \eta_j}\right) \tag{3.17c}$$

$$O\left(\frac{\delta}{M_t}\right) : \frac{\partial w_i^d}{\partial \tau'} = \frac{-1}{\sqrt{\rho}}\frac{\partial p^d}{\partial \eta_i}. \tag{3.17d}$$

We make a few observations from this system of equations. We get the incompressible Navier-Stokes as both M_t and δ tend to zero in Eq. 3.17a. From Eq. 3.17b, we conclude that the solenoidal part of the velocity does not evolve in the acoustic time scale whereas from Eq. 3.17d, we see that the dilatational flow field can evolve in the acoustic time scale as expected. This physically corresponds to the acoustic oscillations seen in equipartition theory where the energy is transferred between dilatational kinetic and internal energies. Finally we can see from Eq. 3.17c that dilatational velocity can evolve in the turbulent time scale and at low $M_t \ll 1$, both these physical phenomena (Eq. 3.17c and Eq. 3.17d) are well seperated or there is an order of magnitude difference consistent with previous studies [35, 43]. Our recent study [35] shows there is no one to one relation between δ and M_t. We showed that under general conditions, $\delta \propto M_t^{\alpha}$ in the $\delta - M_t$ phase plane. The exponent α can even be negative for highly dilatational forcing and depends on the exact characteristics of forcing. This gives rise to different trajectories in the phase plane contrary to a unique trajectory often assumed in the literature.

From Eq. A.1a to Eq. A.1j in the appendix A, we can match the asymptotic expansions for the kinetic energy equations derived by the procedure mentioned previously in this section [91]. The order of magnitude equations for dilatational kinetic energy equation are

$$O\left(\delta\right) : \left\langle \widehat{w}_i^d \left\{ v_j^s \widehat{\frac{\partial w_i^s}{\partial \eta_j}} \right\}^d \right\rangle_k = \left\langle - \widehat{w}_i^d \left\{ \frac{1}{\sqrt{\rho}} \widehat{\frac{\partial p^s}{\partial \eta_i}} \right\}^d \right\rangle_k \tag{3.18a}$$

$$O\left(\delta^2\right) : \left\langle w_i^d \frac{\partial w_i^d}{\partial \tau} \right\rangle + \left\langle w_i^d \left\{ v_j^d \widehat{\frac{\partial w_i^s}{\partial \eta_j}} + v_j^s \widehat{\frac{\partial w_i^d}{\partial \eta_j}} + w_i^s \widehat{\frac{\partial v_j^d}{\partial \eta_j}} \right\}^d \right\rangle_k = \left\langle - \widehat{w}_i^d \left\{ \frac{1}{\sqrt{\rho}} \widehat{\frac{\partial p^d}{\partial \xi_i}} \right\}^d \right\rangle_k + \left\langle \frac{\widehat{w}_i^d}{\sqrt{\rho}} \left\{ \frac{\partial}{\partial \eta_j} \frac{\partial \widehat{v}_i^d}{\partial \eta_j} + \frac{\partial}{\partial \eta_j} \frac{\partial \widehat{v}_j^d}{\partial \eta_i} + \frac{\partial}{\partial \eta_i} \frac{\partial \widehat{v}_j^d}{\partial \eta_j} \right\}^d \right\rangle_k \tag{3.18b}$$

$$O\left(\frac{\delta^2}{M_t}\right) : \left\langle w_i^d \frac{\partial w_i^d}{\partial \tau'} \right\rangle = \left\langle - \widehat{w}_i^d \left\{ \frac{1}{\sqrt{\rho}} \widehat{\frac{\partial p^d}{\partial \eta_i}} \right\}^d \right\rangle_k \tag{3.18c}$$

$$O\left(\delta^3\right):\left\langle \widehat{w}_i^d\left\{ v_j^d\widehat{\frac{\partial w_i^d}{\partial\eta_j}}+w_i^d\widehat{\frac{\partial v_j^d}{\partial\eta_j}}\right\}^d\right\rangle_k=\left\langle -\widehat{w}_i^d\left\{\frac{1}{\sqrt{\rho}}\widehat{\frac{\partial p^d}{\partial\xi_i}}\right\}^d\right\rangle_k \tag{3.18d}$$

$$O\left(\delta^2M_t\right):\left\langle \widehat{w}_i^d\left\{ w_i^s\widehat{\frac{\partial v_j^d}{\partial\xi_j}}+v_j^d\widehat{\frac{\partial w_i^s}{\partial\xi_j}}+v_j^s\widehat{\frac{\partial w_j^d}{\partial\xi_j}}\right\}^d\right\rangle_k=2\left\langle \widehat{w}_i^d\left\{\frac{\partial}{\partial\xi_j}\frac{\partial\widehat{v}_i^d}{\partial\eta_j}+\frac{\partial}{\partial\xi_i}\frac{\partial\widehat{v}_j^d}{\partial\eta_j}+\frac{\partial}{\partial\eta_i}\frac{\partial\widehat{v}_j^d}{\partial\xi_j}\right\}^d\right\rangle_k \tag{3.18e}$$

$$O\left(\delta^2M_t^2\right):\left\langle \widehat{w}_i^d\left\{\frac{\partial}{\partial\xi_j}\frac{\partial\widehat{v}_i^d}{\partial\xi_j}+2\frac{\partial}{\partial\xi_i}\frac{\partial\widehat{v}_j^d}{\partial\xi_j}\right\}^d\right\rangle_k=0 \tag{3.18f}$$

$$O\left(\delta^3M_t\right):\left\langle \widehat{w}_i^d\left\{ v_j^d\widehat{\frac{\partial w_i^d}{\partial\xi_j}}+w_i^d\widehat{\frac{\partial v_j^d}{\partial\xi_j}}\right\}^d\right\rangle_k=0. \tag{3.18g}$$

Similarly, we can derive the solenoidal kinetic energy equations whose first few terms are

$$O\left(1\right):\left\langle w_i^s\frac{\partial w_i^s}{\partial\tau}\right\rangle+\left\langle \widehat{w}_i^s\left\{ v_j^s\widehat{\frac{\partial w_i^s}{\partial\eta_j}}\right\}^s\right\rangle_k=-\left\langle \widehat{w}_i^s\left\{\frac{1}{\sqrt{\rho}}\widehat{\frac{\partial p^s}{\partial\eta_i}}\right\}^s\right\rangle_k+\left\langle \frac{\widehat{w}_i^s}{\sqrt{\rho}}\left\{\frac{\partial}{\partial\eta_j}\frac{\partial\widehat{v}_i^s}{\partial\eta_j}+\frac{\partial}{\partial\eta_j}\frac{\partial\widehat{v}_j^s}{\partial\eta_i}\right\}^s\right\rangle_k \tag{3.19a}$$

$$O\left(\delta\right):\left\langle \widehat{w}_i^s\left\{ v_j^d\widehat{\frac{\partial\widehat{w}_i^s}{\partial\eta_j}}+v_j^s\widehat{\frac{\partial\widehat{w}_i^d}{\partial\eta_j}}+w_i^s\widehat{\frac{\partial v_j^d}{\partial\eta_j}}\right\}^s\right\rangle_k=-\left\langle \widehat{w}_i^s\left\{\frac{1}{\sqrt{\rho}}\widehat{\frac{\partial p^d}{\partial\xi_i}}\right\}^s\right\rangle_k \tag{3.19b}$$

$$O\left(\delta^2\right):\left\langle \widehat{w}_i^s\left\{ v_j^d\widehat{\frac{\partial w_i^d}{\eta_j}}+w_i^d\widehat{\frac{\partial v_j^d}{\eta_j}}\right\}^s\right\rangle_k=-\left\langle \widehat{w}_i^s\left\{\frac{1}{\sqrt{\widehat{\rho}}}\widehat{\frac{\partial p^d}{\partial\xi_i}}\right\}^s\right\rangle_k \tag{3.19c}$$

$$O\left(\delta^2M_t\right):\left\langle \widehat{w}_i^s\left\{ v_j^d\widehat{\frac{\partial w_i^d}{\partial\xi_j}}+w_i^d\widehat{\frac{\partial v_j^d}{\partial\xi_j}}\right\}^s\right\rangle_k=0. \tag{3.19d}$$

We provide the complete set of equations in the appendix A. The *cross advection terms* contained in both the solenoidal and dilatational components can result in the dynamic interaction of modes, an important property of compressible turbulence. From Eq. 3.18b, we can see in the $O\left(\delta^2\right)$, the solenoidal component plays a role in the evolution of the dilatational component. If the

compressible conditions are such that $O(\delta^2)$ equation dominates, we can expect real complex interacting dynamics. But on the other hand, if $O(\delta^2/M_t)$ dominates the behavior of the system, then the two modes are independent and it corresponds to linear equipartition. This small discussion shows that characteristics of turbulence would depend on the relative magnitude of δ and M_t [35]. In other words, it depends on the trajectory followed by the system in the $\delta - M_t$ phase plane. In Chap. 6, we analyze these order of magnitude equations for the dilatational kinetic energy in detail to divide the $\delta - M_t$ phase plane into distinct physical compressible regimes where we propose various normalization for the dilatational spectra at different regimes.

4. UNIVERSALITY AND SCALING IN COMPRESSIBLE TURBULENCE

One of the main obstacles for progress in compressible turbulence is the difficulty in finding universal scaling laws under diverse compressibility conditions. Traditionally, this has been attempted by using two non-dimensional parameters: Taylor Reynolds number, R_λ, the ratio of inertial to viscous forces and the turbulent Mach number, M_t, the ratio of a characteristic turbulent velocity scale to the speed of sound. In general, the efforts to find universality have been mixed in success, inconclusive and often contradictory. The scaling laws in general depend on the type of forcing mechanisms that sustain turbulence [47, 48, 72, 141, 145, 140, 147], initial conditions [102, 113] and other flow details which are in direct contrast to the success achieved in incompressible turbulence where universal scaling laws have been both insightful and practically useful [51, 125].

We argue in this section that universal scaling laws can indeed be observed in compressible turbulence but one has to include a parameter that represent internally generated dilatational motions in the governing parameter set. The previous efforts were focussed on externally imposed scales leading to an incomplete set of governing non-dimensional parameters to define the state of turbulence which are different from our current approach. We argue this drawback of previous studies is due to some implicit assumptions about the variables that control the system.

We show that the dilatational motions have to be explicitly considered to define the state of compressible turbulence. First we show that the flow undergoes a transition between two equilibrium states using pressure fluctuations. One regime is dominated by solenoidal pressure that obeys the elliptical nature of incompressible pressure whereas the other regime is dominated by dilatational pressure corresponding to linear acoustic oscillations. We derive a governing parameter that predicts this transition by comparing the relative order of magnitude strengths of these two equilibria. Classical parameters such as M_t and R_λ also fail to collapse or describe other important statistical quantities pertaining to the dynamics of compressible turbulence such as the dissipation rate, the skewness of the velocity gradient which exemplify the strength of the non-linear

behaviour, that leads to the conspicuous non-Gaussianity of turbulence. But when we introduce dilatational motions into the set of governing parameters, we see that universality can indeed be observed. This will be used to describe different statistical regimes of compressible turbulence in the extended parameter space which can explain some discrepancies observed in the literature. The different regimes in the $\delta - M_t$ phase plane can be used to explain when and in what sense the universal scaling laws can be expected.

4.1 Background

In order to avoid the complications from wall effects, spatial non-uniformities and transients, a common paradigm is to isolate the intrinsic dynamics to understand fundamental issues in turbulence by focussing on statistically steady homogeneous flows. Although greatly simplified, the rigorous treatment of the governing Navier-Stokes leads to extraordinary theoretical difficulties. As a consequence, both experiments and numerical simulations have been main drivers of progress. In particular for compressible turbulence, conducting experiments in this simplified set up is exceedingly difficult and thus experiments on homogeneous compressible turbulence have been scarce or even non-existent. Thus numerical simulations especially DNS which solves the entire temporal and spatial scales of the governing equations [58, 92] have been a main tool for investigating the physics of compressible turbulence.

Since relatively a lot is known about incompressible turbulence because of the comparatively large body of literature, more limited set of governing parameters and physical process, the most common strategy in understanding compressible turbulence is to study the departures from the scaling laws observed in the incompressible counterpart for similar conditions. Such an approach has led to significant advances in the field [52, 84].

4.2 Governing Parameters, Scaling and Similarity

Before we start to study similarity scaling in compressible turbulence, we briefly review the fundamental aspects and issues of its application to incompressible turbulence. Here we consider the Navier-Stokes equation along with continuity which represent the conservation of momentum

and mass respectively. We can then use a characteristic velocity, (U) and length scale, (L) to normalize the governing equations. Then using dimensional analysis techniques, one can come up with a general scaling relationship for any normalized statistical quantity of interest, Q and can be represented as $\overline{Q} = f_i(R)$. Here an overbar means normalized quantity and f_i is assumed to be a universal function for incompressible flows. Here, $R \equiv \rho U L/\mu$ is the well known non-dimensional quantity, Reynolds number, where μ and ρ are the dynamic viscosity and density respectively. Thus at same R, we can expect identical properties for geometrically similar flow. In principle, if U & L (for example, mean speed, mesh size in grid turbulence or size of the object generating turbulent wake) are known parameters and scaling laws in R are known, one achieves powerful predictive capabilities. This is called *external* similarity since L and U are imposed externally.

This framework fails when we attempt to compare across flows with dissimilar geometry. As an example, the scaling of the normalized mean dissipation rate $\langle\epsilon\rangle L/U^3$ (where ϵ is the instantaneous turbulent dissipation rate and $\langle\rangle$ is suitable ensemble average) is not expected to be the same for flows with distinct geometry such as grid turbulence or wake created due to a bluff body. It is thus common to use intrinsic turbulent parameters to compare across different flows. A large-scale Reynolds number $R_L = u'L/\sqrt{3}\nu$ (where $u'^2 = \langle|\mathbf{u} - \langle\mathbf{u}\rangle|^2\rangle$, L are the root-mean-square velocity and integral length scale respectively) or the Taylor Reynolds number, $R_\lambda = u'\lambda/\sqrt{3}\mu$ are the obvious choices. In the definition of R_λ, λ is the Taylor micro-scale which is an intermediate scale in between the large and small scales corresponding to viscous dissipation. The scaling of different statistical features of turbulence with R_λ, that is:

$$\overline{Q} = f_i(R_\lambda), \tag{4.1}$$

has been extensively studied in the incompressible turbulence literature. We wish to point out two critical issues. First, an implicit assumption that a single length and velocity scale are sufficient to characterize the flow at least in a statistical sense is apparent. Next, the flow scales $(u', L, \text{ and } \lambda)$ can be computed from the flow itself and thus from a priori known geometrical details of the flow

set up, their values can be estimated to within an order of magnitude. Thus we indeed have to acknowledge the fact that there is a knowledge gap between a priori characteristic velocities & lengths from the original geometry and the internal scales generated due to flow dynamics driven by these particular initial and boundary conditions defined by U and L. We call this approach *internal* or *self-similarity* since we are using internally generated scales. A conspicuous disadvantage of this approach is that we do not have pure predictive capabilities from a priori known flow characteristics, but is well suited to discover universal aspects across geometrically different flows.

The Kolmogorov phenomenology [70] is a well-known example where he showed that the internally generated Kolmogorov length scales can be used to find universality. The success of the proposed universality is indeed obvious since the multi-scale flow statistics collapse when normalized by Kolmogorov scales [93] at least for low orders [51]. The most salient example is the collapse of the compensated energy spectra at different Reynolds numbers from a wide variety of flows [126].

The primary strategy in studying universality in compressible turbulence is to interpret the departures from the known results in incompressible turbulence as compressibility effects [84]. It is common to access the strength of compressibility with the ratio of a characteristic velocity to the speed of acoustic propagation, defined as a Mach number, $M = U/c$. We approach the incompressible flow regime when $M = 0$ since $c \to \infty$. A well known example of the use of Mach number, M is the observed reduction of the spreading rate of a mixing layer when M (defined with some characteristic convective velocity) increases [121]. It is still not unanimous on what is the correct characteristic velocity to define M is [52]. A large body of literature has been devoted to homogeneous isotropic turbulence where no mean flow exists. This precludes the difficulties encountered in taking in to account geometrical factors and one can directly study the complexity of turbulence in general and in particular its interaction with compressibility. Thus this approach allows one to understand the fundamental intrinsic characteristics that emerge directly from the governing equations. In this current work, we study such flows where it is common to characterize compressibility with the turbulent Mach number, $M_t \equiv u'/\langle c \rangle$. In the definition,

u' is the root-mean-square velocity and $\langle c \rangle$ is the speed of sound. This can be considered as an example of self-similarity for compressible flows. However, here there is an implicit assumption that acoustic wave propagation speed completes the set of governing parameters of the flow. For a perfect gas, the relation $c^2 \sim \langle T \rangle \sim \langle p \rangle / \langle \rho \rangle$ is perhaps a more appropriate interpretation. Thus at least in a mean sense, when density is included in the set of governing parameters, c completes the specification of the thermodynamic state of the flow. Also note that, including c in the set of governing parameters corresponds to internal self similarity as in general, the mean speed of sound depends on the flow solution which includes the fluctuations of temperature. Thus we propose

$$\overline{Q} = f_c(R_\lambda, M_t), \tag{4.2}$$

which is a direct ramification from self-similarity. Here $\overline{Q}$ is any non-dimensional statistical quantity and f_c is a universal function. A considerable amount of research in compressible turbulence is based on this above scaling assumption. For example, several theories based on M_t and R_λ have been proposed to determine the scaling of important compressible statistics such as dilatational dissipation [52] and spectrum [61, 140, 144]. Weaker formulations of the form $\overline{Q} = f_i\left(R_\lambda\right) f_c\left(M_t\right)$, have also been proposed in the literature. All these proposals have been met with mixed success and failed to unravel any universal trends when compared with data from numerical simulations. We argue that this failure is due to the incorrect identification of non-dimensional parameters to determine the statistical nature of compressible turbulence. Although M_t compares the magnitude of turbulent velocity to the acoustic propagation speed, it does not contain any information regarding the amount of energy in the compressible modes that propagate in this wave-like fashion.

4.3 The Role of Dilatational Motions

The failure of Eq. 4.1 is evident since the qualitative behaviour of the turbulence changes depending on the nature of forcing and initial conditions. For both terrestrial and astrophysical contexts, the structure and dynamics of flow strongly depend on the proportion of dilatational content in forcing [48, 65, 119] and initial [102, 108, 113] conditions.

Let us consider the mass conservation equation

$$\frac{1}{\rho}\frac{D\rho}{Dt} = -\nabla \cdot \boldsymbol{u}\ , \tag{4.3}$$

where D/Dt is the substantial derivative. One can easily identify that density changes directly depend only on the dilatational component of the velocity. Thus it becomes apparent that one requires a dilatational velocity scale, U^d to properly normalize Eq. 4.3. Moreover in many scenarios, to the first order, pressure and density are related through an isentropic or polytropic relation [34, 61] which implies even pressure in the flow field are governed by dilatational motions.

One can derive the evolution equations for the kinetic energy of both modes seperately, starting from the full Navier-Stokes equations as we have seen in Chap. 3. The solenoidal component of velocity and pressure satisfy the incompressible Navier-Stokes and the governing equation for dilatational mode can be obtained by subtracting the solenoidal equation from the total Navier-Stokes. The length and time scales of both components are expected to be distinct [118, 110] when the two modes are decoupled. It can be argued that at low M_t and small fluctuations, the dilatational component of velocity can be considered to be decoupled from the solenoidal mode. One can get similar results from a different perspective, for example when the governing equations assuming isentropic fluctuations are linearized and the velocity field is projected into the Craya basis in Fourier space [120]. In this frame of reference, the dilatational velocity projects only along the wavenumber vector $\mathbf{k}$. In Fourier space, $\hat{\mathbf{u}}^s \cdot \mathbf{k} = 0$ (caret implies Fourier transform of the variable) since the solenoidal component is divergence free. Thus to the first order, the dilatational velocity and pressure evolve according to

$$\begin{aligned} \partial u^d/\partial t &= c_0\, k\, P^d \\ \partial P^d/\partial t &= -c_0\, k\, u^d. \end{aligned} \tag{4.4}$$

Since in the Fourier space, the dilatational component is parallel to the $\mathbf{k}$ direction, u^d in the above equation can be considered as a scalar. In the above equations, c_o and k are the speed of sound and

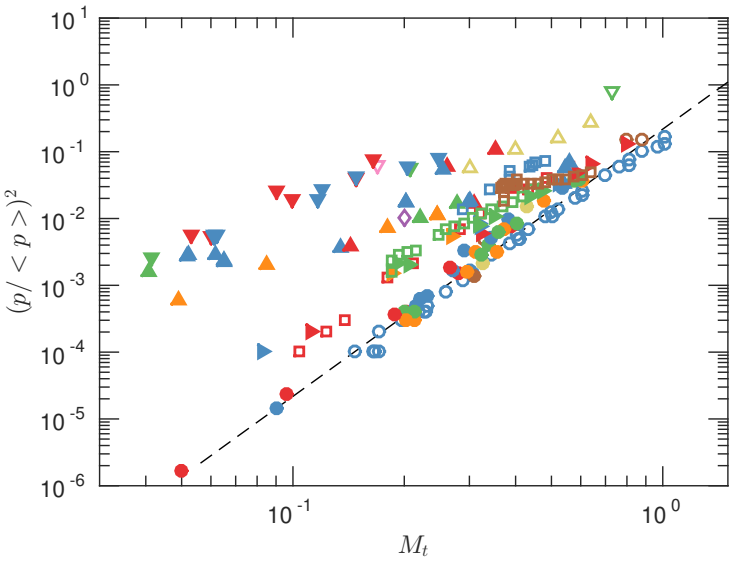

Figure 4.1: Scaling of variance of pressure with M_t. Dashed line is $\gamma^2 M_t^4/9$, the scaling proposed in [34].

wavenumber respectively. The pressure is normalized as $P^d = ip^d/\rho_o c_o$ where $i = \sqrt{-1}$. An analytical solution is possible for the above simplified equations. But here it is sufficient to note that, in a such a scenario, the dilatational motions are completely decoupled from the solenoidal modes and the dynamics are governed by the energy exchange between the dilatational mode of pressure and velocity. In this situation, we do not expect a characteristic solenoidal velocity to scale Eq. 4.4 which is completely dominated by the dilatational modes. These arguments can be applied to the evolution of the different Kovasznay decomposed modes [121].

The collected data in the literature lend support to these above arguments, implying in general, the scaling corresponding to Eq. 4.2 does not hold. For example, consider the scaling of mean normalized pressure variance with M_t in Fig. 4.1. The data in the figure consist of statistically stationary flows with pure solenoidal (circles) forced cases and a combination of solenoidal & dilatational (triangles) forced cases. It is crystal clear that dilatational forcing has indeed a profound effect on the flow features that generate pressure fluctuations. In fact, the order of magnitude of the pressure fluctuations when dilatationally forced are much greater than ones with just solenoidal

Flow type	σ	M_t	R_λ	Symbol
HIT, S [140]	100	0.05-1.02	38-370	○
HIT, S [65, 66]	100	0.11-0.88	12-44	○
HIT, S [142, 141]	100	1.03	254	○
HIT, S (Present)	100	0.05-0.6	38-430 †	●●●●●●
HIT, D [65, 66]	0	0.11,0.17	5.4,10	▽
HIT, D [147]	33.33	0.73	210	▽
HIT, D [144]	50	0.30-0.65	196-234	△
HIT, D [95]	4.76, 50 †	0.6	180	▽△
HIT, D (Present)	70-90	0.04-0.8	30-160 †	▶▶▶▶
HIT, D (Present)	35-70	0.05-0.55	38-154 †	▲▲▲▲
HIT, D (Present)	0-35	0.04-0.25	16-77 †	▼▼▼
HST [22]	...	0.03-0.66	32-220	□
HST [117]*	...	0.2-0.5	16-35	□
HST [116]	...	0.2-0.7 †	14-45	□□
HST [115]*	...	0.13-0.65	14-32	□
HIT, S, TF [145]	100,..	0.2,0.6	250	◇
HIT, S, BV [23]	100	0.1-0.6	100	+
HST, BV [23]	...	0.1-0.6	100	+

Table 4.1: Databases used in this study. Flow types: homogeneous isotropic turbulence (HIT), which can have solenoidal forcing (S, circles), some dilatational forcing (D, triangles), homogeneous shear turbulence (HST, squares), or thermal forcing (TF). We also include flows (HIT, HST) with different types of gases, in particular two studies with gases for which the ratio of bulk to shear viscosity is 30 (BV) compared to zero for all the other cases. Studies with multiple symbols correspond to the different conditions marked with a † in increasing order. Studies marked with an asterisk did not provide δ and was thus computed using pressure fluctuations and Eq. 4.9.

forcing at similar M_t. Apart from the data in the current study, Fig. 4.1 includes data from a large number of studies in the literature. These are summarized in Table 4.1 including cases that are solenoidally, dilatationally and thermally forced (or its combination) isotropic turbulence along with homogeneous shear flows. For general conditions, the inadequacy of proposed scaling with M_t [61] for solenoidal forcing (dashed line) is obvious when there is some dilatational forcing or modes are created due to thermodynamic coupling between temperature and dilatational field as in thermal forcing. The latter case is important in turbulent combustion when heat is generated due to exothermic chemical reactions. But later we show that universal scaling laws emerge when we include non-dimensional groups involving dilatational motions.

4.4 Self Similarity for Compressible Flows

We now return to the discussion of general principles pertaining to scaling in incompressible turbulence. In compressible turbulence, we are faced with similar challenges but on a much larger parameter space. To characterize the compressible system, we have to supplement the incompressible parameter space by a dilatational velocity, U^d that take into account the strength of the dilatational motions. It is still not clear, how one can attain this velocity from geometrical aspects such as the grid for a given flow. Although it might be possible to obtain it for a particular scenario, it is highly probable that the results would depend on the details of the setup. Thus we propose to use the same approach as in incompressible turbulence, where we seek to discover internal similarity in which an internal dilatational scale is generated by the flow itself. The root-mean-square of the dilatational component of velocity, u^d based on the Helmholtz decomposition is the most apt choice. The argument above is analogous to the incompressible case which lead to the choice of u'. Thus the enlarged modified parameter space is

$$Q = f(L, \mu, \langle\rho\rangle, u', c, u'^d). \tag{4.5}$$

In the expression above, we have only used a single length scale. This can be justified by the fact that for example, the integral length scales are generated by the largest scales in the geometry with-

out any distinction between solenoidal and dilatational modes. This does not in general insinuate that length scales of both modes are the same but are governed by the parameters in Eq. 4.5. The success of such an assumption can only be validated if such a proposal can result in providing universal scaling laws that can collapse numerical and experimental data which is demonstrated in this current work.

The number of parameters in Eq. 4.5 can be reduced from six to three by dimensional analysis. We can form different non-dimensional groups that include dilatational motions such as $\delta = u^d/u^s$, $\chi \equiv K^d/K$ (where $K^d = \langle\rho|u^d|^2\rangle/2$ and $K^s = \langle\rho|u^s|^2\rangle/2$ are the turbulent dilatational and total kinetic energy respectively.), and $M_d \equiv u^d/\langle c\rangle$ which compares the ratio of dilatational velocity and acoustic propagation. The parameter, χ is widely used as an initial condition in the literature, whereas M_d has been proposed in astrophysical contexts [72]. It is trivial to derive the relationships between these parameters, for example, $\chi \approx \delta^2/\left(\delta^2+1\right)$ or $M_d \approx M_t\sqrt{\chi}$ where these approximations are possible assuming density correlations are not strong enough, which have been verified to be the case for the objective of the work. In the past, the focus of many investigations has been to derive the scaling laws of these dilatational parameters in terms of M_t, for example, $\chi \sim M_t^2$ or M_t^4 were proposed based on different EDQNM closure assumptions [112]. But we have in general seen that M_t and R_λ alone cannot characterize completely the statistical state of turbulence from Fig .4.1.

The main aim of this thesis is to explore the viability of the non-dimensional groups such as M_t and δ as the proper similarity parameters to discover universal behaviour. We propose self similar scaling and thus universality in compressible turbulence is plausible if internal dilatational motions are included in the governing parameters as below:

$$\overline{Q} = f_c(R_\lambda, M_t, \delta). \tag{4.6}$$

in place of Eq. 4.1. Thus here we supplement the traditional parameters M_t and R_λ with δ.

The additional parameter δ to describe compressibility points out another important facet that may not be straightforward. Traditionally and even today, M_t is used to characterize two aspects

of compressible turbulence. First, it is used as a measure of compressibility strength or more explicitly dilatational motions in the flow field. On the other hand, it is interpreted as the ratio of acoustic to turbulence time scale. This comes from the following arguments. The large turbulent time scale can be represented by the eddy-turnover time, L/u' whereas the acoustic time scale can be identified as $L/\langle c \rangle$. Physically, this is the time taken for an acoustic wave to traverse a distance of the order of the largest scales in the flow field. Of course, this ratio is M_t and is a measure of separation of the two processes. Thus at low M_t, the acoustic and turbulent processes are decoupled and after some simplification of the governing equations, we obtain the linear system in Eq. 4.4 [43]. This conceptually does not allow a system with strong compressibility effects (high δ), but happens at a short acoustic time scale (low M_t).

The above observation can shed some light in explaining the accuracy and robustness of equipartition ($F_p \approx 1$ as shown below) at high M_t although the theorem was proposed in the limit of low M_t. Thus, for example in [61], as M_t was increased, so did χ and δ. Thus we can conjecture that, at high δ, the dilatational motions dominate the dynamics of flow field even thought the scale separation was not large due to high M_t. It is possible that equipartition embodied in Eq. 4.4 may be valid for a wider range of conditions than originally proposed.

4.5 The Scaling of Pressure in Compressible Turbulence

We had earlier seen from Fig. 4.1, the dramatic effect of dilatational forcing on the scaling of the pressure variance. In fact, using Eq. 4.3 and Eq. 4.4, we argued that thermodynamic fluctuations, for example pressure and density fluctuations are governed by dilatational motions, and thus we proposed Eq. 4.6. For pressure fluctuations, we can derive the statistical equilibrium equations for pressure at two asymptotic limits which can be used to rigorously justify our proposal.

Assuming Eq. 4.6 is correct, we propose the scaling of pressure variance as $p'^2/\langle p \rangle^2 = f_c\left(R_\lambda, M_t, \delta\right)$ where the mean pressure, $\langle p \rangle$ is defined as $\langle p \rangle = \langle c \rangle^2 \langle \rho \rangle / \gamma$. Pressure attains a statistical equilibrium with $p' \approx A\langle \rho \rangle |u^s|^2$ with a tenuous Reynolds number dependence [40, 79] in the incompress-

ible limit. This expression can be rewritten in terms of the parameters in Eq. 4.6 as

$$\frac{p'^2}{\langle p \rangle^2} \approx A^2 \gamma^2 M_t^4 / 9. \tag{4.7}$$

For compressible turbulence, the above scaling was verified from solenoidal forced homogeneous isotropic [34, 140] and shear simulations [22] with slightly different prefactor A for these simulations. One can also see that solenoidal forced cases (circles) follow this scaling (dashed line) in Fig. 4.1.

In the other limit of pure dilatational motions, system is governed by Eq. 4.4 if one neglects non-linearity. It is possible to get analytical solutions for u^d and p^d for Eq. 4.4 with appropriate initial conditions. For low M_t, Sarkar *et al.* [118] showed that, for any initial conditions, the unforced flow would asymptote to an equilibrium state of equipartition where the dilatational kinetic energy and potential energy stored in dilatational pressure are in equilibrium resulting in acoustic oscillations. In the literature, this is called equipartition. But here, we call it p-equipartition to differentiate with another equipartition to be discussed later. This statistical state on an average can be explicitly expressed by the equipartition function $F_p = c_o^2 \rho_o^2 |u^d|^2 / |p^d|^2 = 1$, which simply is the ratio of dilatational kinetic to potential energy. Although this result only involves dilatational pressure, as compressibility effects increase, the dilatational pressure dominates over solenoidal pressure. Thus the scaling of the dilatational pressure can be approximated as the scaling for the total pressure. Thus for dilatationally dominated p-equipartition (DDE), we expect total pressure variance to scale as $p'^2 = c_0^2 \rho_0^2 |u^d|^2 / F_p$ and after proper non-dimensionalization, we get

$$\frac{p'^2}{\langle p \rangle^2} = \frac{\gamma^2 M_d^2}{F_p}. \tag{4.8}$$

Here, $M_d = u'^d / \langle c \rangle$ is the dilatational Mach number and can be rearranged as $M_d \approx M_t \delta / \sqrt{\delta^2 + 1}$. Clearly, it is obvious that the above scaling conforms to Eq. 4.6 rather than Eq. 4.2. To test the scaling, we plot the normalized pressure variance with dilatational Mach number in Fig .4.2. Compared to Fig. 4.1, one observes a much better collapse of the data on to a universal curve at

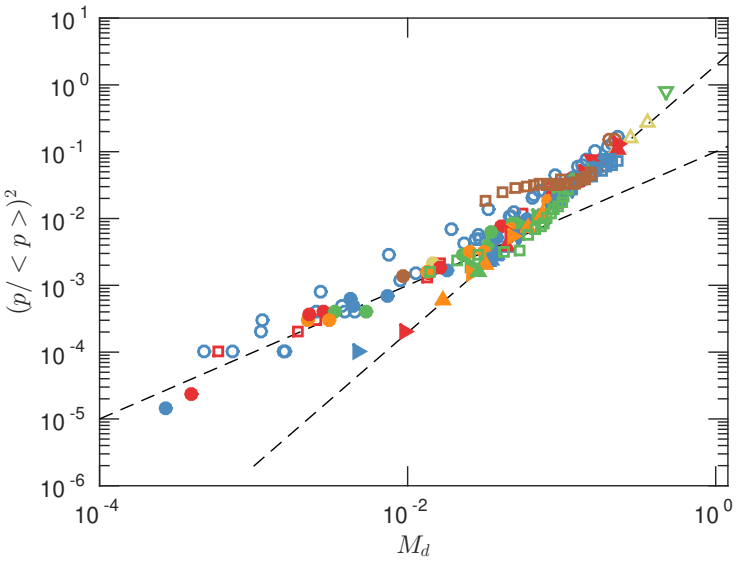

Figure 4.2: Scaling of variance of pressure with M_d. Dashed lines are $\gamma^2 M_d^2/F_T$ (high M_d) and $\propto M_d$ for reference (low M_d).

high M_d. One finds that Reynolds number effects are negligible consistent with previous studies [61, 34]. Our current database has cases where dilatational motions are generated exclusively due to Navier-Stokes dynamics (solenoidal forcing, thermal forcing or homogeneous shear flows) and directly driven due to external dilatational forcing.

These findings have important ramifications for the scaling of compressible turbulence. Eq. 4.8 expressing p-equipartition is an analytical result derived from the governing equations [118] neglecting terms that correspond to non-linear and viscous processes. Hence one can conclude that Eq. 4.2 is fundamentally incomplete in characterizing compressible turbulence under general conditions since p-equipartition is satisfied for many cases from our DNS database.

Since $p = p^s + p^d$ by construction, we get $p'^2 = |p'^s|^2 + |p'^d|^2 + 2rp'^s p'^d$, where r being the correlation coefficient between the two modes of pressure. At the two extreme asymptotic limits, contributions from only one of the component dominates the total field implying either $p' \approx p'^s$ or $p' \approx p'^d$. If one can assume that the two pressure fields are weakly correlated [61] as in low M_t,

then

$$\frac{p'^2}{\langle p \rangle^2} \approx A^2 \gamma^2 \frac{M_d^4}{\delta^4} + \frac{\gamma^2}{F_p} M_d^2. \tag{4.9}$$

And after proper non-dimensionalization, we can rewrite as:

$$\frac{p'^2}{\langle p \rangle^2} \frac{F_p}{M_d^2 \gamma^2} \approx A^2 F_p D^{-2} + 1, \tag{4.10}$$

where we introduce the new parameter defined as:

$$D \equiv \delta \sqrt{\delta^2 + 1} / M_t. \tag{4.11}$$

D is the ratio of the rms of dilatational pressure to solenoidal pressure. D of course can also be written in terms of other common parameters used in the literature, for example, $D = \delta\sqrt{\delta^2+1}/M_t = \sqrt{\chi}/M_t\,(1-\chi)$. This indeed demonstrates that D is a complex combination of the elementary proposed parameters. This can be considered as a self similarity of second kind [6, 7] where the governing parameters cannot be found out by simple dimensional analysis arguments.

Interestingly, D can be used to divide certain statistical regimes one expects turbulence to be in. At high enough D, flow field is dominated by dilatational pressure and the main mechanism driving the dynamics of the pressure fluctuations is the p-equipartition governed by Eq. 4.4. Whereas in the other limit of low D, the pressure manifests the elliptical nature embodied by the incompressible Navier-Stokes equations. Since $A \sim O\,(1)$ and $F_p = 1.0$ in p-equipartition, we can expect a critical $D = D_{crit}$ value of $O\,(1)$ that divide the two regimes. Therefore, the exact value of the D_{crit} and asymptote D would weakly depend on the flow characteristics through the constant A.

Fig. 4.3 agrees with these conclusions where the pressure variance is normalized according to Eq. 4.9. We have excellent collapse of the data with a sharp transition around $D_{crit} \approx 0.5$. Transition from solenoidal to dilatational dominated regimes was observed in solenoidal forced simulations [61, 140] albeit M_t was used as the parameter instead of D.

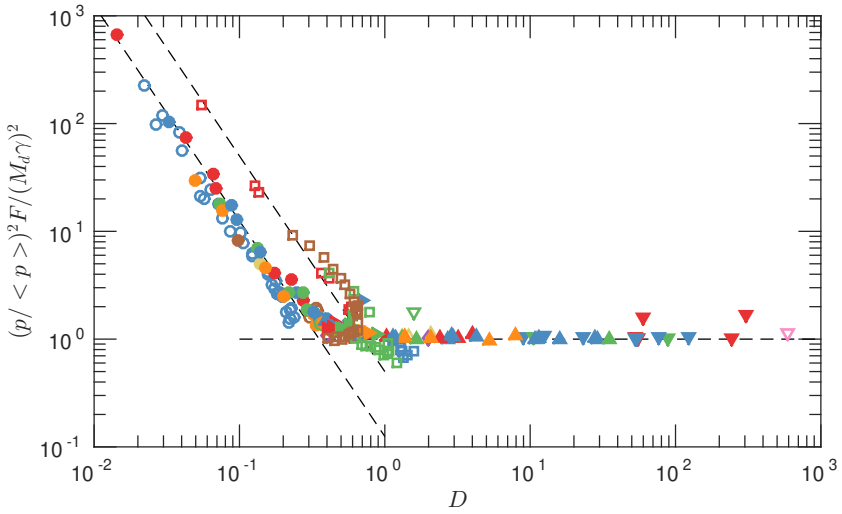

Figure 4.3: Scaling of variance of pressure with $\mathcal{D}$. Dashed lines are $\mathcal{D}^{-2}$ (low $\mathcal{D}$) for different values of A and the asymptotic DDE horizontal lines (high $\mathcal{D}$).

In Fig.4.3, we have flows which are dilationally forced [146, 144, 95], thermally forced [145] and homogeneous shear driven [22, 117, 115]. In the latter, the turbulent fluctuations are generated due to the production mechanism caused by the mean shear. The satisfactory collapse achieved for the compiled data in the literature, spanning a wide range of flow conditions, driven by diverse mechanisms provides ample support for universal self-similar scaling proposed in Eq. 4.6.

The constant A although $O\left(1\right)$ is flow dependent. DNS studies show that $A \approx 1.9$ for shear flows [22] and $A \approx [1.2, 0.9]$ for isotropic solenoidal forced simulations [140, 61]. Thus different asymptotes are observed at low D in Fig. 4.3 whereas the asymptotic state corresponding to p-equipartition seems to be universal.

To arrive at Eq. 4.10, we have assumed that the solenoidal pressure and dilatational pressure are completely independent for all conditions. Although we had observed successful collapse of data, it is possible to observe different scaling laws for both p'^s and p'^d at some conditions perhaps when the two modes are well correlated at high M_t [61].

We would like to point out an interesting observation about Eq. 4.11. M_t is regarded as a measure of compressibility. But Eq. 4.11 alludes that at constant δ, an increase in M_t corresponds

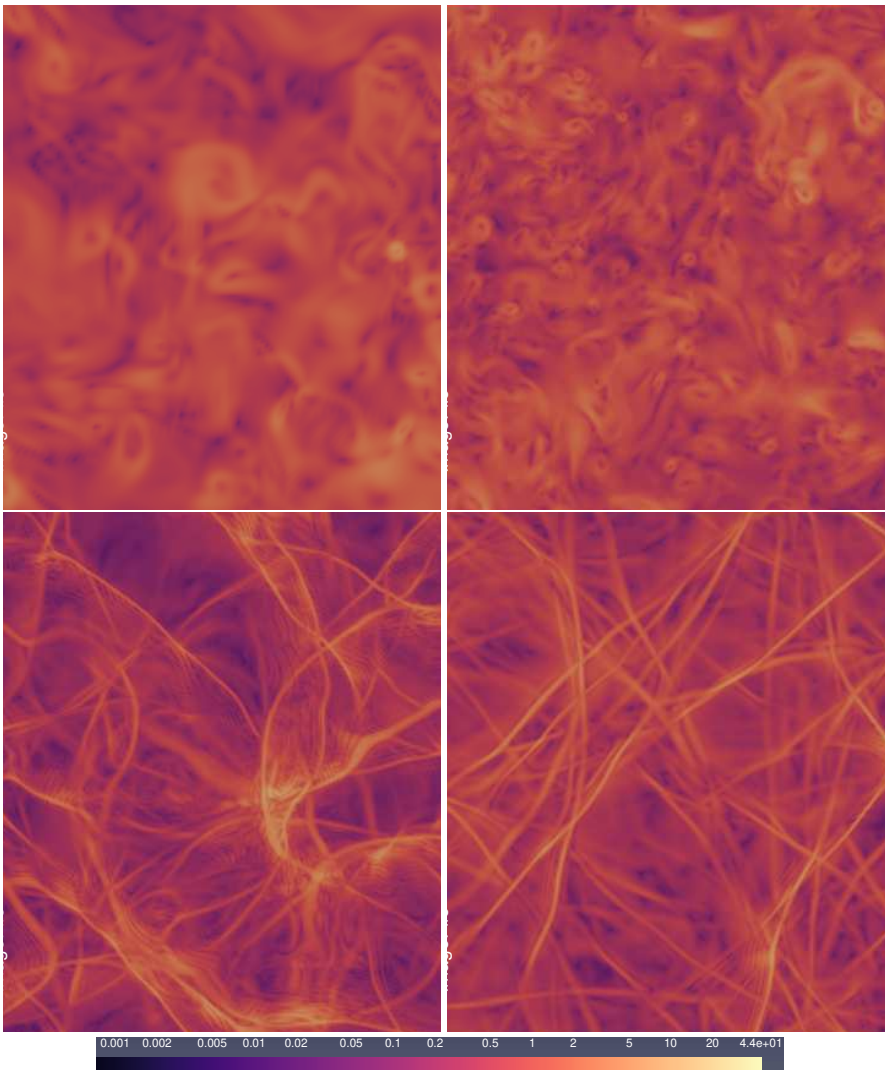

Figure 4.4: Contours of $|\nabla p|/\ |\nabla p|_{rms}$ for $(\mathcal{D}, R_\lambda, M_t, \delta) = (0.04, 58, 0.09, 0.0035)$ (a), $(0.27, 102, 0.36, 0.097)$ (b), $(12, 50, 0.20, 1.4)$ (c), and $(52, 51, 0.06, 1.65)$ (d).

to a decrease in D indicating weaker compressibility effects.

In Fig. 4.4, we plot the contours of the normalized instantaneous pressure gradient at an arbitrary plane at an instant of time for different values of D. It is clear from these figures that spatial structure of the flow field is qualitatively distinct. If we compare flows, (a) and (d) with similar M_t, one observes that the flow features are conspicuously different, proving that M_t is inadequate to capture crucial aspects of the flow field. The pressure gradients contours are similar to that of incompressible pressure in (a) and (b) where $D < D_{crit}$ and is thus the regime where the solenoidal

pressure would dominate the flow field. The fine-scale structures of the flow field also become more prominent with higher R_λ consistent with incompressible behaviour. Beyond the critical D_{crit}, where dilatational pressure dominates, shock fronts corresponding to thin pressure gradients are formed in contrast to the more vortical isotropic spot like structures seen for $D < D_{crit}$. Indeed some minor changes are also seen for cases with $D > D_{crit}$. For example, the shock fronts in (c) are more curved than that observed in (d) hinting probably a stronger interaction between the solenoidal and dilatational modes which we argue later in the chapter is due to the higher M_t in (c).

4.6 Small-Scale Universal Scaling

The small-scale self similar universality is pinned on the classical phenomenology of turbulence. It states that the energy produced at large scales due to geometry or forcing mechanisms such as shear is subjected to instabilities due to the non-linearities inherent in the Navier-Stokes. This results in a transfer of energy to smaller and smaller scales in a step-by-step cascade process. Ultimately, the scales are small such that molecular viscous effects become effective and the energy is dissipated as heat. Longer the scale range, it is assumed that the non-universal large scales aspects of the flow field are forgotten, resulting in a self-similar universality at small scales.

This energy dissipation at small scales results in a rise in temperature and subsequent decay of all turbulent fluctuations. The small scale properties only depend upon the rate at which energy is transferred from large scales. This rate of energy transfer is called the dissipation rate, defined as $\langle \epsilon \rangle = 2\mu \langle s_{ij} s_{ij} \rangle$, where $s_{ij} = \left(\partial u_i/\partial x_j + \partial u_j/\partial x_i\right)/2$ is the strain rate fluctuation tensor. Dissipation being the last process in energy cascade is an indispensable quantity in the classical theory and understanding of turbulence [51]. For homogeneous turbulence, the average dissipation can be written just in terms of vorticity [28] as $\langle \epsilon \rangle = \mu \langle \omega_i \omega_i \rangle$ (where $\omega \equiv \nabla \times \mathbf{u}$ is the vorticity vector). The total dissipation in incompressible turbulence has been subjected to intense research over the past few decades resulting in a large body of literature [126]. The most celebrated and pivotal result is the “Zeroth law of turbulence" which states that the $\langle \epsilon \rangle$ becomes independent of viscosity at high Reynolds number. In compressible turbulence, very little is known [61, 45] about

it due to the additional parameters and physics involved. Dissipative anomaly is the topic of Chap. 5. In compressible turbulence, there are additional contributions to dissipation due to dilatational motions [118] and in particular for homogeneous flows, $\langle\epsilon\rangle = \langle\epsilon_s\rangle + \langle\epsilon_d\rangle$ where $\langle\epsilon_s\rangle = \langle\mu\omega_i\omega_i\rangle$ and $\langle\epsilon_d = (4/3)\,\langle\mu\theta_i^2\rangle$ with $\theta \equiv \partial u_i/\partial x_i$ being the dilatation. The dilatational component requires modeling due to compressibility. An additional term $\mu_v\theta^2$ is present for flows with bulk viscosity [23, 97], where μ_v is the bulk viscosity. For a fixed μ_v/μ, the extra term is proportional to $\langle\epsilon_d\rangle$, thus does not require any additional modeling.

Historically, researchers have tried to model dilatational dissipation as "corrections" to solenoidal dissipation due to compressibility [118]. Most popular models proposed are of the form, $\langle\epsilon_d\rangle \propto \langle\epsilon_s\rangle M_t^\alpha R_\lambda^\beta$ where different models lead to distinct exponents (e.g. $(\alpha,\beta) = (2.0)$ [118], $(4,-2)$ [110], or $(4,-2)$ [140]). Other functional forms such as $\langle\epsilon_d\rangle = \langle\epsilon_s\rangle F\,(M_t)$ have also been proposed in the literature [52, 112]. We plot the ratio of dissipations available in the current literature against M_t in Fig. 6.4. It is clear that there is considerable scatter and any model based on similarity scaling as in Eq. 4.2 would fail to capture any universal behaviour.

Since dissipation is proportional to velocity gradients, we can in veiw of Eq. 4.5 estimate the scaling of $\langle\epsilon_s\rangle$ and $\langle\epsilon_d\rangle$ as $\mu\,(u'^s/L)^2\,g_1\,(R_\lambda, M_t, \delta)$ and $\mu\left(u'^d/L\right)^2 g_2\,(R_\lambda, M_t, \delta)$ respectively where g_1 and g_2 are presumably some universal scaling functions. Therefore we get the scaling for the ratio, $\langle\epsilon_d\rangle/\langle\epsilon_s\rangle = \delta^2 g_3\,(R_\lambda, M_t, \delta)$ where g_3 is again a universal function. The function g_3, should have the form, $g_3 \propto R_\lambda^\alpha M_t^\beta \delta^{-2}$. We show the scaling of the ratio of dissipations versus δ in Fig. 6.4 (b) to check the validity of the above proposed scaling. All the data in the literature seems to collapse along

$$\frac{\langle\epsilon_d\rangle}{\langle\epsilon_s\rangle} \approx \delta^2 \tag{4.12}$$

to the first order implying $g_3 \approx 1$ for a variety of flow fields with forcing conditions. From the figure, one can conclude that the scaling is robust for almost 10 order of magnitude for all flows including shear flows and flows with bulk viscosity. Although, some scatter is observed in the plot, we cannot decipher any systematic trend with other parameters. Once again it proves the adequacy and inadequacy of Eq. 4.6 and Eq. 4.2 respectively. Thus it once again demonstrates the success

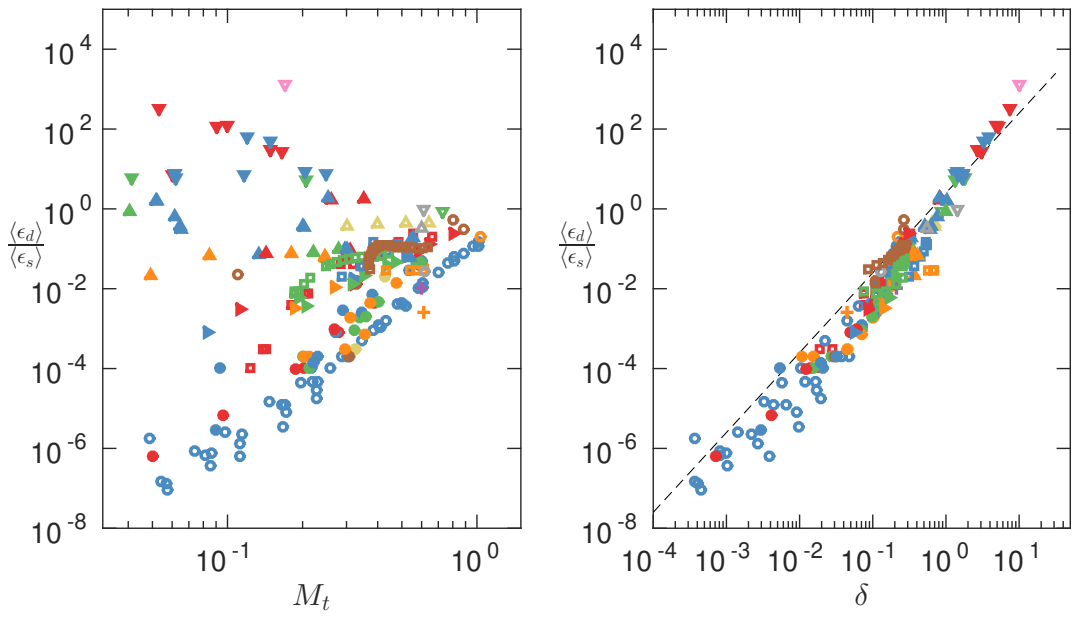

Figure 4.5: Scaling of ratio of dilatational to solenoidal dissipation with (a) M_t and (b) δ. Dashed line in (b) with a slope of 2 for reference.

in identifying universal behaviour when dilatational motions are explicitly included as a governing parameter in the formulation.

Another important small scale statistics of immense importance in incompressible turbulence is the skewness of the velocity gradient and has been studied extensively [126]. For fully developed turbulence, the longitudinal velocity gradients skewness, $S = \langle(\partial u_1/\partial x_1)^3\rangle/\langle(\partial u_1/\partial x_1)^2\rangle^{3/2}$ is a universal constant of around -0.5. The non-zero value of skewness implies that the velocity field in turbulence is non-Gaussian. Physically, velocity skewness is strongly correlated to the vortex stretching mechanism increasing vorticity that eventually leads to the cascade process [28]. In fact this criterion of $S = -0.5$ is so robust that it is common to use this to decide whether realistic turbulence is achieved in both experiments and numerical simulations. However the interpretation in compressible turbulence is more involved although this practise is extended to compressible case too. Hence any difference in S compared to the incompressible value (-0.5) can be considered as turbulence is not fully developed [82], a compressibility effect [139, 140, 141] (although we are

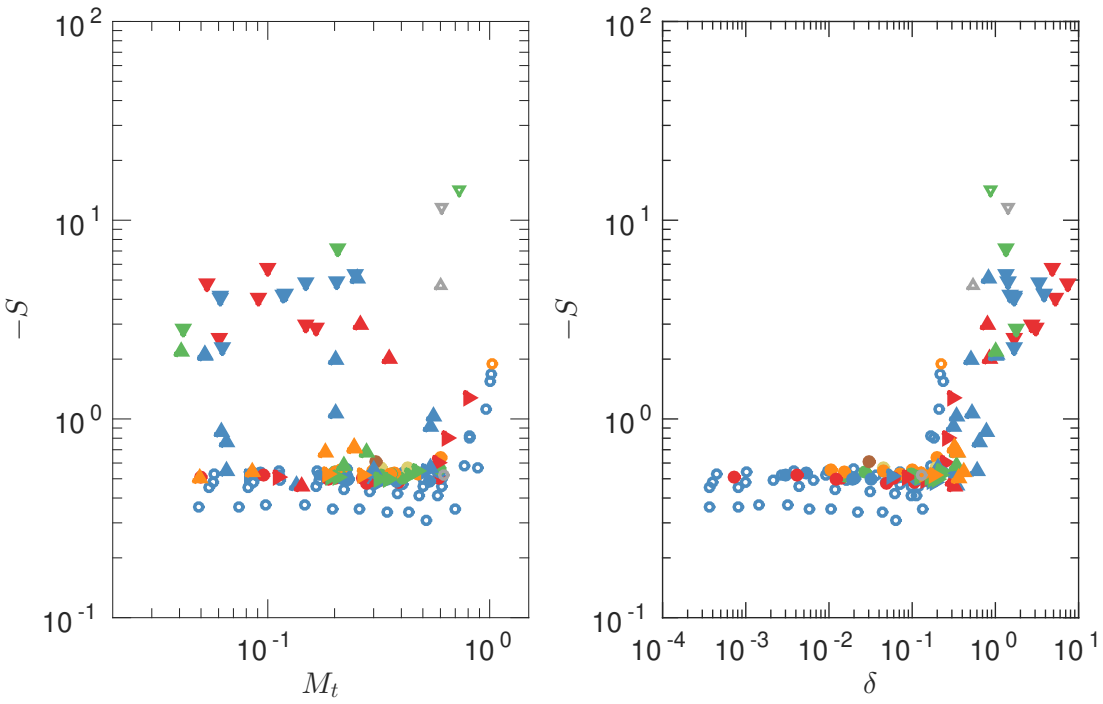

Figure 4.6: Scaling of the negative skewness of the velocity gradient with (a) M_t and (b) δ.

still unsure how S scales with compressible parameters) or even as a numerical artifact [141].

When we plot $-S$ from the compiled data in the literature versus M_t in Fig. 4.6 (a), the familiar non-universality emerges. For cases with solenoidal forcing and low M_t, S is very close to the incompressible value, implying dilatational motions are weak or have equal probability to generate both expansions and compressions. Higher magnitude of S at high M_t has been attributed to shocklets or high compressions [140, 139, 141]. But, we observe large negative skewness even at low M_t under dilatational forcing which underpins the role of dilatational motions. Since under solenoidal forcing, M_t is a proxy for a measure of dilatational motions, δ, we plot S against M_t in Fig. 4.6 (b). There is still considerable scatter although it is better compared to Fig.4.6 (a).

If we assume that large negative skewness of the velocity gradients is due to formation of shocklets due to dilatational motions, we can possibly conjecture that wave-steepening mechanisms are dominant. This occurs due to the non-linear term, $\mathbf{u}^d \cdot \nabla \mathbf{u}^d$. We can estimate the order of magnitude of this term. The order of magnitude if $\mathbf{u}^d$ in the term can be estimated as: $u'^d \sim \delta u'^s$. Due

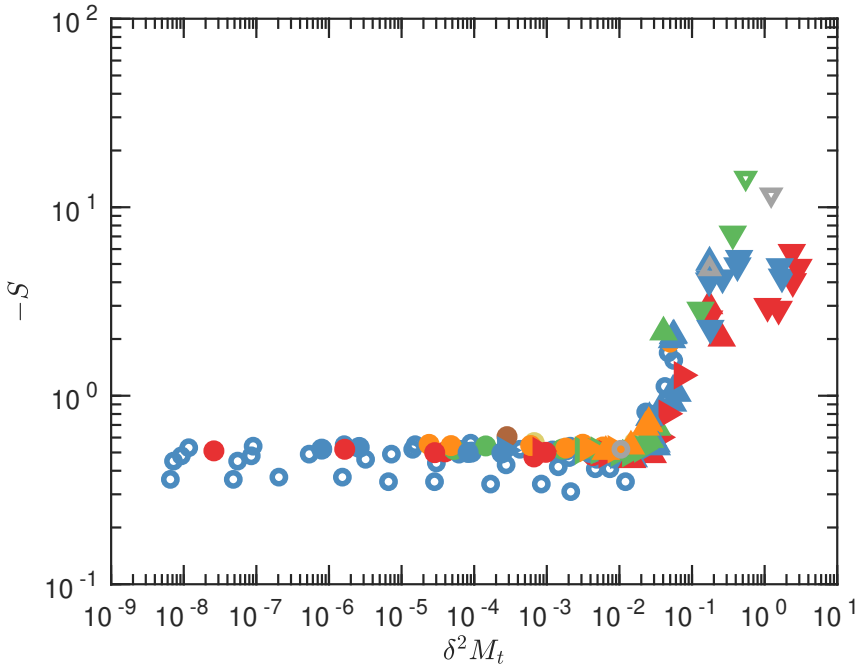

Figure 4.7: Scaling of the negative of the skewness of the velocity gradient with $\delta^2 M_t$.

to the fundamentally different physics represented by solenoidal and dilatational modes, they act at different scales. This leads to two orders of magnitude for gradient operator, $\nabla = \nabla_\eta + M_t \nabla_\xi$ where η and ξ are short and large wavelength scales respectively. The latter one corresponds to acoustic contributions. Thus if we include only the acoustic contributions, we can estimate the magnitude of the non-linear term as $\delta^2 M_t$. The phenomenological argument above implies that $-S$ increases or scales with $\delta^2 M_t$. This is indeed what we observe in Fig. 4.7 where, at a critical value of $\delta^2 M_t \approx 3 \times 10^{-}2$, it diverges from the incompressible value of -0.5. Although we do see some scatter at higher value of $\delta^2 M_t$, "*S-divergence*" at a critical $\delta^2 M_t$ is in agreement with the available data in the literature.

4.7 The Broader Picture

So far, we have demonstrated the inadequacy of the traditional parameters: M_t and R_λ cannot predict the statistical characteristics of compressible turbulence. However incorporating the dilatational motions into the governing parameters have shown some promise in discovering uni-

versal scaling laws. The satisfactory collapse of the data for pressure, dissipation rate and skewness is a testament for the viability of this approach. In the process, we have identified equilibrium regimes some already known in literature and new transitional criteria to distinguish these different regimes. The inset of Fig. 4.8 (a) illustrates these transitions separating dilatationally-dominated-p -equipartition, S-divergence and dominance of dilatational dissipation. The main part represents the variation of δ with M_t for all the data with different forcing conditions.

Clearly from the figure, M_t cannot characterize these transitions alone and thus the state of compressible turbulence in general. Contrary to the critical phenomena seen in classical problems, we cannot identify a simple single transition from “incompressible" to “compressible" regimes (stated very often in the literature parametrized by M_t alone). To demonstrate, if we consider a flow at low M_t, as δ increases, it first experiences DDE transition, then S-divergence and finally the flow will be dominated by dilatational dissipation at higher δ values. Whereas at high M_t, depending on the exact M_t, S-divergence can occur before DDE. So it is very much possible that a flow might be in one dominant compressible regime but not in another. For example, in Fig. 4.8 (a), the high $M_t > 0.8$ cases from [140] have already crossed S-divergence with skewness value much greater than that of incompressible value are not dominated by dilatational pressure. As an example for opposite case, consider our low M_t dilatationally forced isotropic cases and some intermediate-M_t shear cases [22]. These flows achieve DDE much before the S-divergence. Thus comparing different flows with nominally the same value of M_t can lead to potentially misleading conclusions.

For most of the cases in the $\delta - M_t$ phase plane, except for extremely low M_t and high δ, $S-$ divergence occurs much before the flow is dominated by dilatational dissipation. If one assumes that shocklets are responsible for both, then contributions to these processes occur much earlier for the third order moment compared to the second order moment. This is consistent with observation made by [152] that anomalous scaling corresponding to small-scale features emerges at much low R_λ for higher order moments compared to low order moments. In the following work [153], the transition between the statistical steady Gaussian and anomalous states at low and high R_λ

respectively provided key insights in finding the numerical values of the scaling exponents in the anomalous regime. In view of this, the discovery of S-divergence can be pivotal in the future to identify appropriate scaling parameters. This can, using the ideas of [153], provide impetus to completely describe small-scale characteristics in compressible turbulence.

The data we have compiled so far in Fig. 4.8 (a) cover virtually all possible conditions in the $\delta - M_t$ plane. If we can isolate a particular flow, then it appears to follow a specific trajectory in the $\delta - M_t$ phase plane. This trajectory of course depends on forcing and initial conditions. We isolate some subset of database for illustration in Fig. 4.8 (b). The chosen flow fields include: a subset of present solenoidal and dilatational forced cases, homogeneous shear flow of [22] & [116] and some isotropic simulations that inject energy into solenoidal and dilatational modes at a constant ratio at low wavenumbers [144].

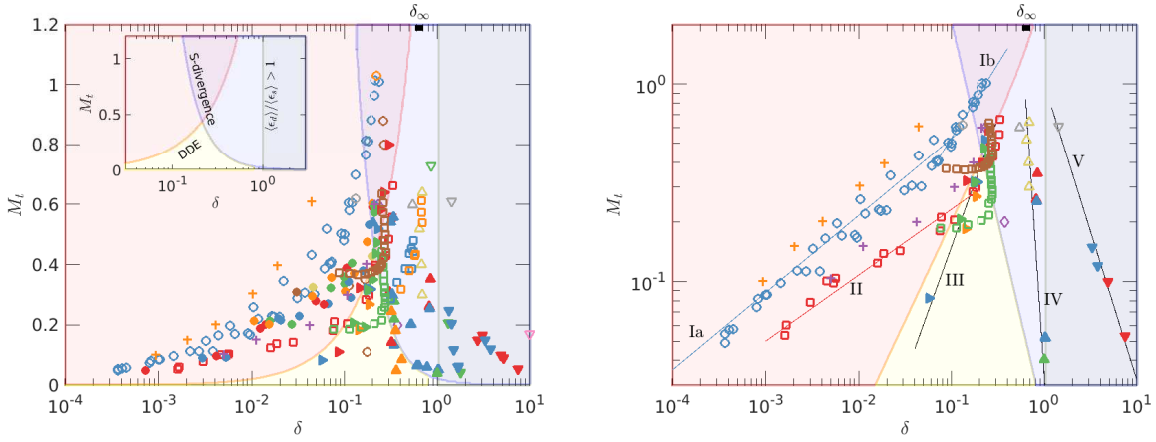

Figure 4.8: Regions in the δ-M_t diagram: Dilatationally dominated p-equipartition (DDE, $\mathcal{D} > \mathcal{D}_{crit}$), S-divergence ($\delta^2 M_t > 2 \times 10^{-2}$), and $\langle\epsilon_d\rangle/\langle\epsilon_s\rangle > 1$. (a) Entire database in Table 4.1. (b) Selected trajectories which include isotropic cases with two types of solenoidal forcing, cases with dilatational forcing, and homogeneous shear flows.

We can infer from Fig. 4.8 (b) that the level of dilatation in the flow field depends on driving mechanisms, geometry and even molecular viscous properties. The exact trajectories for a given flow depend on the conditions created by the governing parameters. For the case of HST flows

[22] (red squares) at constant shear rate, we can see a power law of approximately $M_t \sim \delta^{1/3}$ (line II) or $\delta \sim M_t^3$ as we increase M_t and R_λ at low δ. But at high δ, it seems to transition towards the DDE line, $D = 0.5$ (ie. $M_t = 0.5\delta\sqrt{\delta^2+1}$) or to a constant δ. This is in contrast with behaviour of the isotropic simulations of [140] (blue circles) where δ varies with M_t as $\delta \sim M_t^{2.56}$ at low δ (line Ia) but transitions to a shallower slope of $\delta \sim M_t^{1.33}$ (line Ib) at high compressibility conditions. We should also note that these simulations never cross the DDE transition. One also notices when comparing these flows, in addition to the difference in the power-laws, the prefactors in the expression relating both δ and M_t are an order of magnitude different resulting in a very different δ for these flows for the same nominal M_t. The trend is different even for isotropic simulations of [144] (yellow triangles) with a different forcing mechanism where δ remains constant with increasing M_t. For temporally evolving shear layer flows of [116] (green and brown squares), starting from different M_ts, M_t remains constant as δ increases at low δ for both cases and afterwards transitions towards a constant M_t trajectory as δ increases. Finally we conclude that trajectories followed in the $\delta - M_t$ phase plane by cases with different levels of dilatational forcing are even qualitatively different. We present results of $\sigma = 10\%$, 40% and 90% dilatational forced cases to demonstrate this. For $\sigma = 10\%$, low dilatational forcing, the behaviour is qualitatively similar to that of solenoidal or shear forced cases with δ increasing with M_t albeit with a smaller power law exponent, $\delta \sim M_t^{0.77}$ (line III). At the other extreme of high dilatational forcing, $\sigma = 90\%$, δ decreases with M_t with a power law trend: $\delta \sim M_t^{-0,67}$ (line V). δ is approximately constant for flows driven by $\sigma = 40\%$ diltational forcing and is comparable to the data of [144] driven by 50% dilatational forcing.

A detailed understanding of the physical mechanism that eventually makes a particular flow to follow a specific trajectory is certainly warranted and can lead to a deeper understanding of the compressible turbulent processes. But our objective here is to establish without a doubt that M_t alone cannot characterize the diverse statistical behaviour seen in compressible turbulence. But in combination with δ, it is possible to put-forward universal scaling laws independent of the external influences, as we have demonstrated for pressure variance, energy dissipation and skewness of the

velocity gradient.

The universal statistical equilibria view proposed here for compressible turbulence in the $\delta - M_t$ phase plane can help us to resolve or explain some of the contradictions in the literature. Just as we have pointed out the different trajectories that different flows follow, it is possible to identify common features the trajectories have for a given class of systems. For example, we can observe that, the solenoidally forced isotropic turbulence follows a trajectory of the form $\delta = C_p M_t^{\alpha}$ where α depends on where the flow is in the $\delta - M_t$ phase plane as we saw before. The prefactors C_p in the relation would depend on the specific details of the forcing mechanism or even molecular properties of the fluid as we explain below. This can be seen when we compare the flows with bulk viscosity (+) which has an extra source of dissipation for dilatational motions [97, 23] which results in lower δ for the same M_t relative to flows without bulk viscosity. One can also deduce from Fig. 4.8 (a) that, prefactors C_p is different for solenoidal forced cases with stochastic [44] and deterministic forcing. Of course we have seen above that dilatational forcing changes the value (and even sign) of the scaling exponents, α. The data from diverse studies in the literature with different numerical schemes and forcing can be grouped into classes of flow with similar trajectory (for e.g: I, IV, V). Similar conclusions can be drawn for homogeneous shear cases too. Thus with the same group or class of flows, Eq. 4.6 can be reduced or approximated to Eq. 4.2 which implies the scaling laws proposed with M_t alone in the literature is a reasonable approximation. Detailed analysis of these trajectories and separation of different universal classes need more data from carefully designed experiments and numerical simulations. Such an endeavour is of course of great value for turbulence modeling. The initial impression from the data in Fig. 4.8 seems to suggest the existence of different classes.

Finally, we compare two theoretical results from the literature in search for universal features. Staroselsky *el al.* [128] used renormalization group theory to study isotropic compressible turbulence with a Gaussian forcing at large scales. The authors report a statistical equilibrium where the ratio of solenoidal and dilatational kinetic energy (δ) is constant, provided the forcing spectrum decays sufficiently fast with respect to wavenumber. They predict an asymptotic limit, where,

$\delta \to \delta_\infty$ and δ_∞^{-2} is derived as approximately 3. Thus $\delta \approx 0.58$. We call this state of equipartition as δ-equipartition to differentiate from p-equipartition. Based on statistical mechanics framework or principles, Kriachanan [74] also proposed δ-equipartition much earlier than [128]. He predicted using Liouville theorem that for the inviscid cases with weak excitation, the vortical modes (two transverse velocity degree of freedom) and acoustic modes (one longitudinal velocity mode and one mode from a bijective function of density) are in equipartition. He predicted a value of $\delta_\infty^2 = 1/2$ or $\delta_\infty = 0.7$ which is quite close to that of [128], though both approaches stem out from entirely different perspectives. Interestingly, the formulation put forward by Kriachnan leads to p-equipartition for weak thermodynamic fluctuations.

We mark the range between the two theoretical limits by a thick line on the top of both panels of Fig. 4.8. On the whole, data in the figure qualitatively seem to approach this theoretical limits suggesting a universal feature across flows. The shear layers of [116], for example seem to follow this trend: δ approaches a constant, independent of M_t, not very far from the theoretical asymptotic limits during the temporal evolution of flow. Although the dilatational motions are much weaker for flows with bulk viscosity at same M_t, the above behaviour with the same asymptotic δ is seen for shear layers with bulk viscosity as large as 30 times the shear viscosity [22]. Solenoidally forced isotropic flows also seem to tend towards the same asymptote, but at a higher M_t compared to shear flows. From our highly dilatationally forced simulations, it can be observed that δ decreases with M_t and might approach the theoretical limit at higher M_t. But it is obvious that δ is bounded for high M_t even for highly dilatationally forced cases. We can find further support for this universal asymptotic behaviour from the simulations of [72]. Their simulations yield a constant, $\delta \approx 0.5$, really close to the theoretical value, for M_t values as high as 15. Since these simulations are based on isothermal Euler equations compared to complete Navier-Stokes equations in Table 4.1, it is plausible that this might be indicating a more general universal ultimate regime for compressible turbulence at high M_t.

Our observations can offer some insights on the correct interpretation of the governing parameters. Traditionally, M_t is interpreted both as the measure of compressibility strength and separation

of time scales. We have argued so far that this interpretation is wrong and M_t is inadequate. M_t represents only the ratio of time scales whereas compressibility or dilatational levels should be explicitly represented by δ. One can expect little interaction between the solenoidal and dilataional mode when time scales are vastly disparate. The asymptotic expansion of Navier-Stokes proposed by Zank and Matthaeus [158] based of M_t as the sole asymptotic parameter suggests that the cross-terms containing solenoidal and dilatational modes responsible for energy exchange between the modes grow with M_t. We can propose a simple physical scenario based on universal δ-equipartition state. At high M_t, for any flow conditions where $\delta \neq \delta_\infty$, the non-linear interactions between the two modes result in a redistribution of energy, such that a state corresponding to $\delta = \delta_\infty$ is achieved. The strong non-linear interactions lead to transfer of energy from dilatational to solenoidal mode if $\delta > \delta_\infty$. If $\delta < \delta_\infty$, the transfer will proceed in the reverse direction. The data in Fig. 4.8 lend support to this phenomenological argument. Our argument also finds support from Fig. 4.4 where the spatial shock fronts are more curved for the case with high M_t, compared to a case with same δ, due to the strong interaction between the vortical motions and compression waves. Rigorous analysis of energy transfers from governing equations is certainly warranted. It is counter-intuitive to note that for $M_t > \delta_\infty\sqrt{\delta_\infty + 1}/D_{crit} \approx 1.34$, δ_∞ is on the solenoidal dominated side of the DDE transition line. Thus when δ-equipartition is achieved at high M_t, the flow will always be dominated by solenoidal pressure. For a constant $\delta = \delta_\infty$, higher the M_t value, the solenoidal pressure becomes more dominant.

4.8 Summary

We finally would like to address the novelty and potential impact of the ideas proposed here. We believe they may be far reaching and broad in scope. Here we provide elements to support this idea.

- We are able to show that isotropic flows and shear layers can be described by universal scaling laws. The collapse observed in the figures is remarkable given the very diverse sources (flows, forcing schemes, level of dilatational forcing, etc) and has been a long-term

goal of the field for decades. Indeed, even in isotropic flows this was not possible until now (which we further integrate with shear flows). The existence of universal scaling laws may be linked to underlying symmetries of the governing equations. While addressing this is beyond the scope of this current work, this is clearly a research line the present work can stimulate which could also be extremely useful in our general understanding of these flows as well as in modeling efforts.

- The data available is limited since only some researchers published e.g. values of δ. But researchers will not publish δ unless there is a reason to do so. In this sense, the universality ideas proposed here would break the cycle, potentially triggering a new era in our understanding of turbulence and pave the way to more accurate turbulence modeling.

- The impact can also extend beyond fundamental understanding. The collapse of dissipation seen for all the database can be used to model $\langle \epsilon_d \rangle$, a quantity that is still widely parametrized by M_t and is well-known to be a weak element in turbulence models in compressible situations. This finding alone can provide a change in direction in how these flows are modeled.

- Perhaps even more important than the collapse is the identification of statistical regimes turbulence can be in and that it does not depend only on M_t. This helps resolve the trends widely observed across the literature. An example, is the disagreement of the skewness of velocity gradients with incompressible values which people have either overlooked or explained away as general "M_t" or "compressibility" effects. The proposed δ-M_t plane, clearly shows that a flow can be in p-equipartition but S is still incompressible, or viceversa depending on conditions. This essentially invalidate simple but widely-made claims such as "at high M_t the flow is compressible". Our work suggests specific ways in which the flow departs from incompressible behavior (e.g. at $M_t \approx 0.6$ the flow could be in p-equipartition or not depending on δ).

- In this plane, we have identified three frontiers that define different behaviors. Except for the dissipation line, the others are indeed novel contributions ($\mathcal{D} \approx 0.5$ and $\delta^2 M_t \approx 0.03$) which,

while simple, have never been presented or studied before. Our work, we believe, can lead to identification of other regions which may overlap, expand or consolidate regimes. This will represent another big step, sparked by the present work, in unraveling the complexities of compressible turbulence by identifying ranges of validity of different theories, for example.

- We also introduce the concept of trajectories in the new δ-M_t plane which can unify behaviors. We propose that universality may manifest itself as *universal trajectories* for different classes of flows. These trajectories relate M_t and δ in a universal manner for a given flow. This is a completely new perspective which may provide a basis for connecting with statistical mechanics, or more accurate turbulent models.

- Finally, in the δ-M_t plane, we have identified a general pattern leading to the identification of a potential fixed point or ultimate regime at high M_t which is very close to those predicted by sophisticated (but seemingly forgotten) theoretical developments. Here again, this discovery may point to a universal state (δ_∞) around which theories can be developed and provide a deeper connection between the classical description of compressible turbulence and more powerful theoretical frameworks (statistical mechanics and RNG).

5. DISSIPATIVE ANOMALY IN COMPRESSIBLE TURBULENCE

5.1 Introduction

Dissipative anomaly plays a pivotal role in the theory of turbulence and is also known as the "zeroth law of turbulence" [51]. As Saffman epitomized its importance in his remark: "This result (dissipative anomaly) is fundamental to an understanding of turbulence and yet lacks theoretical support". Despite its importance, studies of dissipative anomaly are non-existent in compressible turbulence literature. Thus we devote this chapter to systematically analyze the validity of dissipative anomaly in compressible turbulence.

In incompressible turbulence, Taylor [130] proposed a scaling of dissipation given as

$$C\left(R_\lambda\right) = \langle\epsilon\rangle \frac{L}{u'^3}, \tag{5.1}$$

where $\langle\epsilon\rangle$, L, $R_\lambda = u'\lambda/\langle\mu\rangle$ and u' are the total dissipation, integral length scale, Taylor Reynolds number and root-mean-square (rms) velocity of the flow field respectively. Dissipative anomaly states that at high enough Reynolds number, the above normalized dissipation becomes independent of Reynolds number. The implication is that dissipation, a small scale quantity becomes independent of viscosity and thus imparts support to the K41 framework of small universality and cascade.

The dissipative anomaly in incompressible turbulence has been empirically validated in incompressible turbulence starting from the works of Sreenivasan [122, 124]. Later studies comprised of experimental [98, 134], decaying [89, 148] and forced numerical simulations (DNS) [16, 19, 38, 54, 63, 148, 156]. In all these studies, at high enough Reynolds number ($R_\lambda \geq 100$), $C\left(R_\lambda\right)$ in Eq. 5.1 asymptotes to a constant around $0.4 - 0.65$. Doering and Foias [30] derived an analytical bound for dissipation from incompressible Navier-Stokes and proposed a functional

form for normalized dissipation as below

$$C \equiv \langle \epsilon \rangle \frac{L}{u'^3} = A \left(1 + \sqrt{1 + (B/R_\lambda)^2} \right). \tag{5.2}$$

The accumulated DNS database [38] of homogeneous isotropic incompressible turbulence conforms to the above functional form with empirical constants: $A = 0.2$ and $B = 92$.

For different flows, for example: two-dimensional wakes, grid turbulence, and homogeneous shear [17], C depends on the geometry, boundary and initial conditions consistent with Taylors' [130] proposal. A different scaling $C \propto R_I^m / R_L^m$ was proposed [135] where $m \approx 1 \approx n$, R_I and R_L, an well defined global and local Reynolds number respectively. This scaling for dissipation was reported despite a K41 [70] inertial range scaling of $k^{-5/3}$ for the energy spectrum in these flows. The authors in this reference [135] discuss the implications of the non-universality of C on the cascade dynamics of incompressible turbulence. McComb [88] and Vassilicos [135] have compiled the available data for C in the literature and a more elaborate discussion on dissipative anomaly in incompressible turbulence can be found in these references.

There are theoretical arguments [2] and numerical evidences [143, 146] that confirm a cascade for the dilatational component. Despite of this, the scaling given in Eq. 5.1 have never be validated in compressible turbulence under general conditions of forcing. Moreover, Eyink and Drivas [45] derived scaling exponents for the velocity, temperature and density assuming dissipative anomaly holds for solenoidal, dilatational and entropy modes separately. Due to the presence of vortical (solenoidal: $\nabla \cdot \mathbf{u}_s = 0$), acoustic and entropy (dilatational: $\nabla \times \mathbf{u}_d = 0$) modes, C can depend on how each mode is excited in a particular flow field [124] and thus may not be universal in compressible turbulence.

The available data so far in the literature on dissipative anomaly for compressible turbulence are from solenoidally forced simulations. For weakly compressible turbulence, Pearson *et al.* [99] showed that although there is a time lag between energy injection and dissipation, C asymptotes to 0.5 for the time averaged statically steady flow field at high Reynolds number , $R_\lambda > O(100)$.

For their simulations, M_t, R_λ and δ ranged from $0.13 - 0.15$, $20 - 219$ and $0.01 - 0.1$ respectively. The above study assumed an isothermal fluid with constant viscosity and sound speed.

Jagannathan and Donzis [61] conducted solenoidally forced DNS of complete compressible Navier-Stokes equations resulting in a wider range of M_t $(0.1 - 0.6)$, R_λ $(32 - 430)$ and δ $(10^{-3} - 0.21)$. Consistent with the previous incompressible results for the range of conditions considered in their studies, C approaches an asymptotic of 0.5 at $R_\lambda > 100$. We have seen in Chap. 4 that dissipation can be decomposed into solenoidal and dilatational [118] components similar to the velocity field [118] as below:

$$\langle \epsilon \rangle = \langle \epsilon_s \rangle + \langle \epsilon_d \rangle. \tag{5.3}$$

The relative strength of these dissipation gives the measure of compressibility effects at small scales. Jagannathan and Donzis [61] argued that both components of the dissipation have to reach an asymptotic state to establish that dissipative anomaly holds in compressible turbulence. Apart from R_λ, as we had seen in Chap. 4, compressible parameters such as M_t and δ [35] are needed to characterize the distinct regimes or behaviour manifested in compressible turbulence. Thus, for dissipative anomaly to hold, $R_\lambda \to \infty$ have to supplemented by extra limits in terms of δ and M_t. To verify the possibility of other limits, the authors analyzed the trend of $\langle \epsilon_d \rangle L/u'^3$ with M_t. Due to solenoidal forcing, the relative contribution of dilatational dissipation is less than 5% of the total dissipation. The normalized dilatational dissipation dramatically increased with M_t after a threshold M_t of 0.3. The authors suggested higher M_t and R_λ are required to arrive at a reasonable conclusion on dissipative anomaly in compressible turbulence.

In these above studies, the total flow field is dominated by the solenoidal field. Recent studies [35, 144, 145] confirm that the dilatational part of the velocity field strongly depends on the characteristics of forcing. Thus one can suspect that C may not be universal in compressible turbulence under general conditions of forcing. Thus in this chapter, we systematically study dissipative anomaly for total, solenoidal and dilatational dissipation in compressible turbulence for a wide range of compressibility conditions.

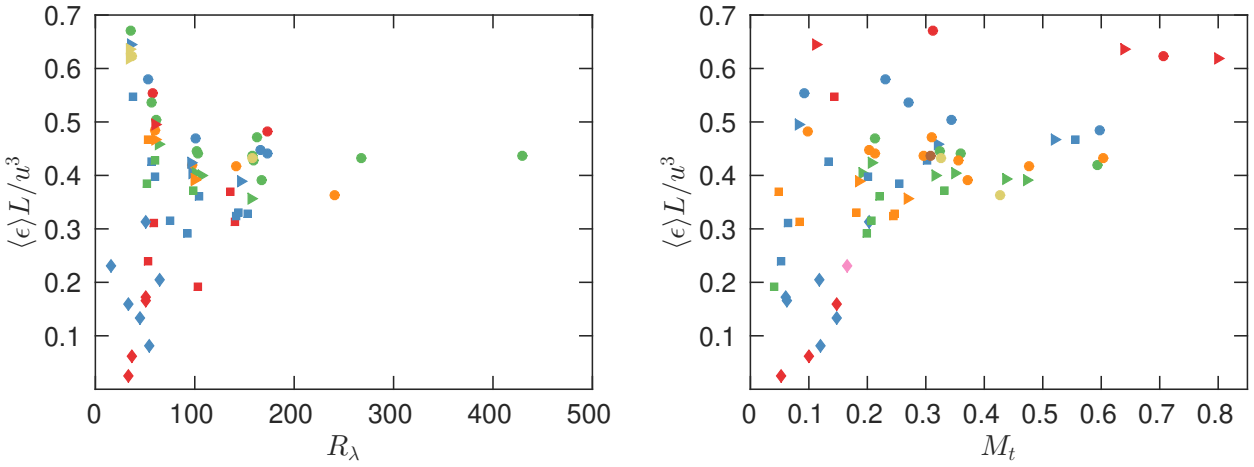

Figure 5.1: (a) Total dissipation normalized by total velocity and integral length scale based on total energy spectrum vs total Taylor Reynolds number. (b) Total dissipation normalized by total velocity and integral length scale based on total energy spectrum vs turbulent Mach number. Here and in all figures to follow in this chapter, circles: pure solenoidal forcing; triangles: percentage of dilatational forcing between 10 to 30 (weak dilatational forcing); squares: percentage of dilatational forcing between 40 to 60 (moderate dilatational forcing); diamonds: percentage of dilatational forcing between 70 to 100 (strong dilatational forcing). In (a), the colors correspond to turbulent Mach number: $M_t < 0.1$, $0.1 < M_t < 0.25$, $0.25 < M_t < 0.4$, $0.4 < M_t < 0.6$, $M_t > 0.6$ and in (b) colors correspond to R_λ: $R_\lambda < 20$, $20 < R_\lambda < 40$, $40 < R_\lambda < 70$, $70 < R_\lambda < 115$, $115 < R_\lambda < 180$, $180 < R_\lambda < 280$, $280 < R_\lambda < 500$.

5.2 Total and Solenoidal Dissipation: Classical scaling

We first study the traditional scaling of total dissipation. The normalized total dissipation, C is plotted against the Taylor Reynolds number in Fig. 5.1 (a). One finds that consistent with previous results [61], the trend is similar to incompressible flow field when forced solenoidally. But dilatational forced cases show considerable compressibility effects as evident from the scatter observed with R_λ. To discover any potential compressibility trend, Fig. 5.1 (b) depicts the behaviour of C with M_t. One cannot find any conceivable trend with M_t for C. The scatter in Fig. 5.1 (b) with M_t is perhaps not surprising since in Chap. 4 we have shown [35] that M_t alone is inadequate to characterize the complex behaviour manifested by compressible turbulence.

To unravel the complicated trends in Figs. 5.1 (a) and (b), we propose to study the different contributions to dissipation separately. We start with solenoidal dissipation, $\langle\epsilon_s\rangle$. We propose a

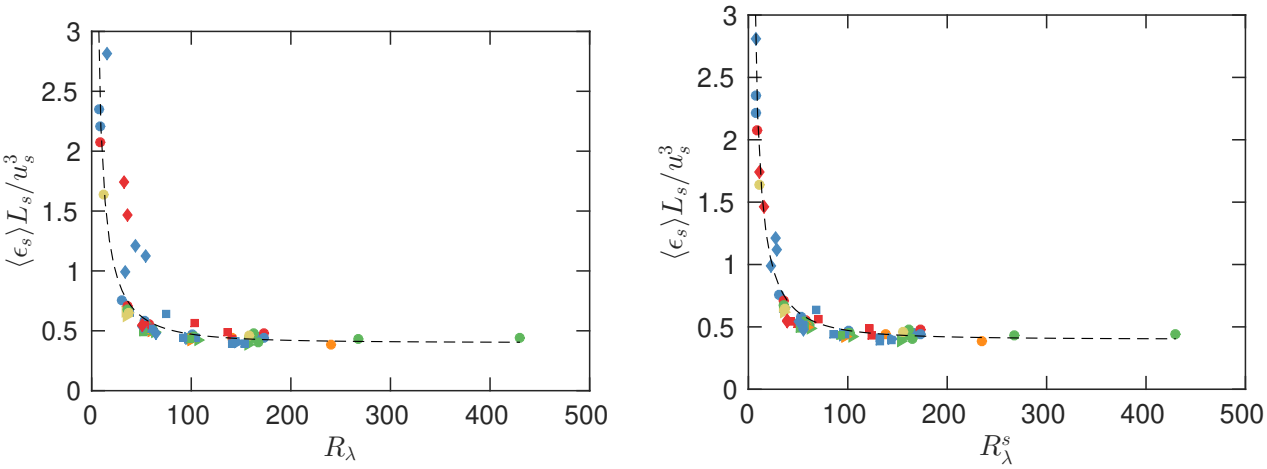

Figure 5.2: (a) Solenoidal dissipation normalized by solenoidal rms velocity and solenoidal integral length scale based on total energy spectrum vs total Taylor Reynolds number. (b) Solenoidal dissipation normalized by solenoidal rms velocity and solenoidal integral length scale based on total energy spectrum vs solenoidal Taylor Reynolds number. In both figures, the color scheme corresponds to M_t as in Fig. 5.1 (a). The dashed line in (a) and (b) correspond to expressions in Eq. 5.2 and Eq. 5.5 respectively.

scaling of the form

$$C_s \equiv \langle\epsilon_s\rangle L_s/u_s'^3, \tag{5.4}$$

since John *et al.* [62] have successfully collapsed the K41 compensated solenoidal energy spectra using just the solenoidal dissipation and Kolmogorov length scale, $\eta_s = (\langle\nu\rangle^3/\langle\epsilon_s\rangle)^{1/4}$ for a wide range of forcing conditions. In the expression Eq. 5.4, u_s' and L_s are the solenoidal rms velocity and longitudinal solenoidal integral length scale based on the solenoidal energy spectrum alone respectively. We plot C_s versus total Taylor Reynolds number in Fig. 5.2 (a). At high R_λ, C_s asymptotes to a constant similar to the incompressible case. Compressibility effects are evident from the figure at low R_λ.

The total Reynolds number has contributions from both solenoidal and dilatational motions. To be completely true to Eq. 5.4, it is logical to define the Reynolds number based on just the solenoidal variables. Therefore, we introduce a new solenoidal Taylor Reynolds number, $R_\lambda^s = u_s'\lambda_s/\langle\nu\rangle$. From the definitions, it is trivial to show that the solenoidal Taylor Reynolds number is

related to the total one as $R_\lambda^s = R_\lambda \left(u_s'/u'\right)\left(\lambda_s/\lambda\right) = R_\lambda \left(u_s'/u'\right)^2 \sqrt{\langle\epsilon\rangle/\langle\epsilon_s\rangle}$. Fig. 5.2 (b) indicates excellent collapse and the scaling of C_s with R_λ^s conforms to the form:

$$C_s \equiv \langle\epsilon_s\rangle \frac{L_s}{u_s'^3} = A\left(1 + \sqrt{1 + \left(B/R_\lambda^s\right)^2}\right), \tag{5.5}$$

with fitting parameters $A = 0.2$ and $B = 92$ identical to the incompressible case.

5.3 Alternate Scaling of Total Dissipation

Before we discuss the results for dilatational dissipation, $\langle\epsilon_d\rangle$, which of course we do not expect to scale with $u_s'^3/L_s$, we analyze the scaling of total dissipation with $u_s'^3/L_s$ as shown below:

$$C' \equiv \langle\epsilon\rangle L_s/u_s'^3. \tag{5.6a}$$

The above equation helps to divide between the solenoidal and dilatational dominant regimes at small scales. We can expand $\langle\epsilon\rangle$ in the above equation and after some minor rearrangement, we get

$$C' \equiv \langle\epsilon\rangle L_s/u_s^3 = \langle\epsilon_s\rangle L_s/u_s^3 \left(1 + \langle\epsilon_d\rangle/\langle\epsilon_s\rangle\right) = C_s\left(R_\lambda^s\right)\left(1 + \langle\epsilon_d\rangle/\langle\epsilon_s\rangle\right). \tag{5.6b}$$

Based on the relation in Eq. 5.5 for C_s, one can arrive at two asymptotic limits at low and high R_λ^s for Eq. 5.6b. The two limits can be written as

$$C' \equiv \langle\epsilon\rangle L_s/u_s^3 = \begin{cases} \left(R_\lambda^s\right)^{-1}\left[1 + \langle\epsilon_d\rangle/\langle\epsilon_s\rangle\right] \text{ for } R_\lambda^s \to 0 \\ 0.5\left[1 + \langle\epsilon_d\rangle/\langle\epsilon_s\rangle\right] \text{ for } R_\lambda^s \to \infty. \end{cases} \tag{5.6c}$$

We propose here to rewrite the R_λ^s limits in terms of δ limits. From the definition, $R_\lambda^s = R_\lambda \left(u_s'/u'\right)^2 \sqrt{\langle\epsilon\rangle/\langle\epsilon_s\rangle}$. We [35] saw in Chap. 4 that to the first order, $\langle\epsilon_d\rangle/\langle\epsilon_s\rangle$ scales as δ^2 and assuming constant total Taylor Reynolds number. When $\delta \to \infty$, we have $R_\lambda^s \propto \delta^{-1}$ and thus is equivalent to the limit

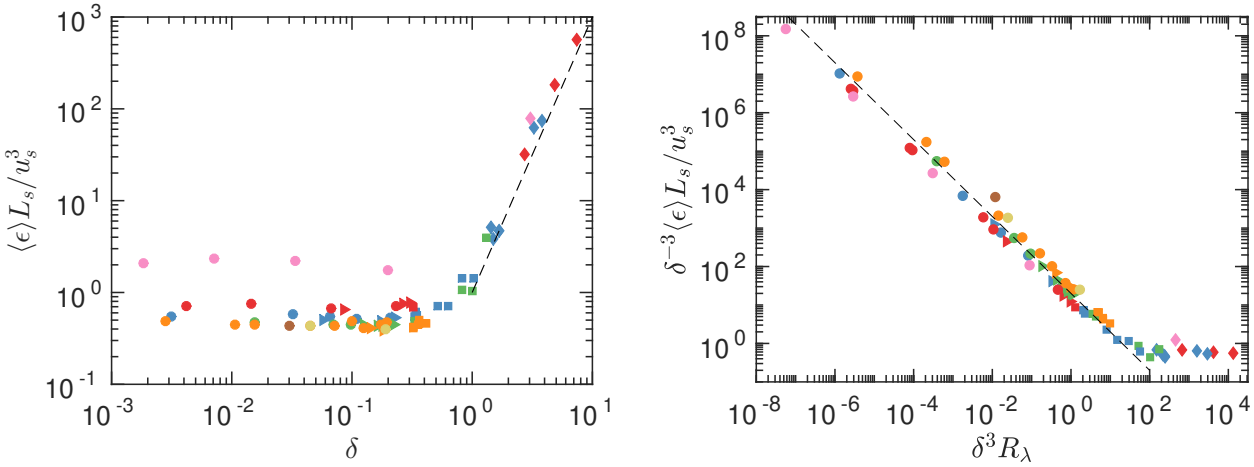

Figure 5.3: (a) Total dissipation normalized by solenoidal rms velocity and solenoidal integral length scale based on total energy spectrum vs δ. (b) Scaling of modified parameters, $\delta^{-3}C'$ vs $\delta^3 R_\lambda$. In both figures, the color scheme corresponds to R_λ as in Fig. 5.1 (b). The dashed lines in (a) and (b) correspond to a power law of 3 and -1 respectively.

$R_\lambda^s \to 0$. Similarly, for the limit $\delta \to 0$, $R_\lambda^s = R_\lambda$. Thus equation in terms of δ limits are

$$C' \equiv \langle\epsilon\rangle L_s/u_s^3 = \begin{cases} (\delta)\,[1 + \langle\epsilon_d\rangle/\langle\epsilon_s\rangle] \approx \delta^3 \text{ for } \delta \to \infty \\ 0.5\,[1 + \langle\epsilon_d\rangle/\langle\epsilon_s\rangle] \approx 0.5 \text{ for } \delta \to 0, R_\lambda \to \infty. \end{cases} \tag{5.6d}$$

This confirms that C' has two asymptotic limits with different scaling. To verify this, in Fig. 5.3 (a), we plot C' verses δ. Indeed, we observe two asymptotic limits. At high δ, from Fig. 5.3 (a), C' scales as δ^3 as predicted by Eq. 5.6d and seems to be independent of R_λ. The implications are that in these conditions, the major contributions to the total dissipation are from dilatational dissipation. As δ decreases, the corresponding contribution from solenoidal dissipation increases. In the other limit of $\delta \to 0$, we recover the incompressible dissipative anomaly trend and C' eventually asymptotes to 0.5. It is interesting to note that the scaling of total dissipation is independent of M_t and the δ^3 scaling regime increases with Reynolds number.

Thus C' exhibits a two parameter (δ and R_λ) dependence where C' has a R_λ dependence at low δ but transitions to a δ dependence at higher δ. This type of scaling in multiple asymptotic

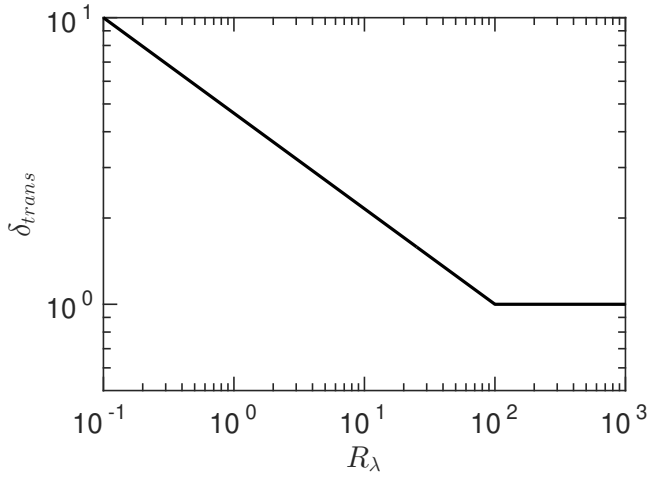

Figure 5.4: Transitional δ as a function of Taylor Reynolds number.

limits can be analyzed using Widom's [151] arguments from statistical mechanics. For examples pertaining to fluid dynamics, Goldfeld [53] and Chen & Donzis [21] used similar techniques to study the transitional behaviour in rough pipes and shock-turbulence interactions respectively. In the latter study, transition from the traditional LIA theory to that proposed by Donzis [31, 32] was successfully predicted. We propose the following functional form for C' aligned with these previous studies:

$$C' = f_1\left(\delta, R_\lambda\right). \tag{5.7a}$$

The scaling at the two asymptotic limits puts constraint on the functional form of f_1. Since C' has to scale as δ^3 at high δ, we assume the following form for f_1:

$$C' = \delta^3 f_2\left(\delta^\alpha, R_\lambda\right). \tag{5.7b}$$

In the opposite limit of $\delta \to 0$, the incompressibility condition has to be satisfied by f_1. Therefore f_2 is constrained such that it has to satisfy $C' \propto R_\lambda^{-1}$ and cancel the δ^3 scaling in Eq. 5.7b. The above constraints are satisfied if $\alpha = 3$. Therefore

$$C' = \delta^3 f_2\left(\delta^3 R_\lambda\right). \tag{5.7c}$$

We can expect universal behaviour if we plot the modified parameters: $C'\delta^{-3}$ and $\delta^3 R_\lambda$. As expected, we see excellent collapse of data in Fig. 5.3 (b). One can find the transition between the two scaling laws from the figure. According to the figure, the transition from solenoidal dominated to dilatational regime happens at around $\delta^3 R_\lambda \approx 100$. The transitional δ for a given R_λ is

$$\delta_{tr} = \left(\frac{100}{R_\lambda}\right)^{1/3}. \tag{5.8}$$

The above equation is valid until we reach dissipative anomaly which correspond to $R_\lambda \approx 100$. The above equation equation suggest the transitional δ decreases with R_λ. The behaviour of δ_{trans} with R_λ is given in Fig. 5.4.

5.4 Dilatational Dissipation

It is hard to conceive a single generalized scaling for the dilatational part of dissipation since as we showed in Chap. 4, there exists distinct regimes with different characteristics. Still, we try to apply the insights gained from the scaling of the total and solenoidal dissipation. Therefore, we define the normalized dilatational dissipation as:

$$C_d \equiv \langle \epsilon_d \rangle L_d / u_d'^3. \tag{5.9}$$

In Fig. 5.5 (a), we plot C_d with Taylor Reynolds number. The figure shows that there is considerable compressibility effects. The scatter in C_d is more evident from the inset where we plot the data in the linear-linear scale. It is difficult to find any systematic trend from this figure.

We introduce a new dilatational Reynolds number, $R_\lambda^d = u_d' \lambda_d / \nu$. It is trivial to get the relation, $R_\lambda^d = R_\lambda (u_d'/u')(\lambda_d/\lambda)$. The physical meaning of R_λ^d is obscure compared to solenoidal Reynolds number. Nevertheless, we see some collapse of C_d with R_d^λ from Fig. 5.5 (b) although an asymptotic state is not reached with R_d^λ. One issue trying to characterize compressibility with R_d^λ is that R_λ^d can tend to ∞ even when both $\delta, M_t \to 0$ provided $R_\lambda \to \infty$. This is also evident from the figure.

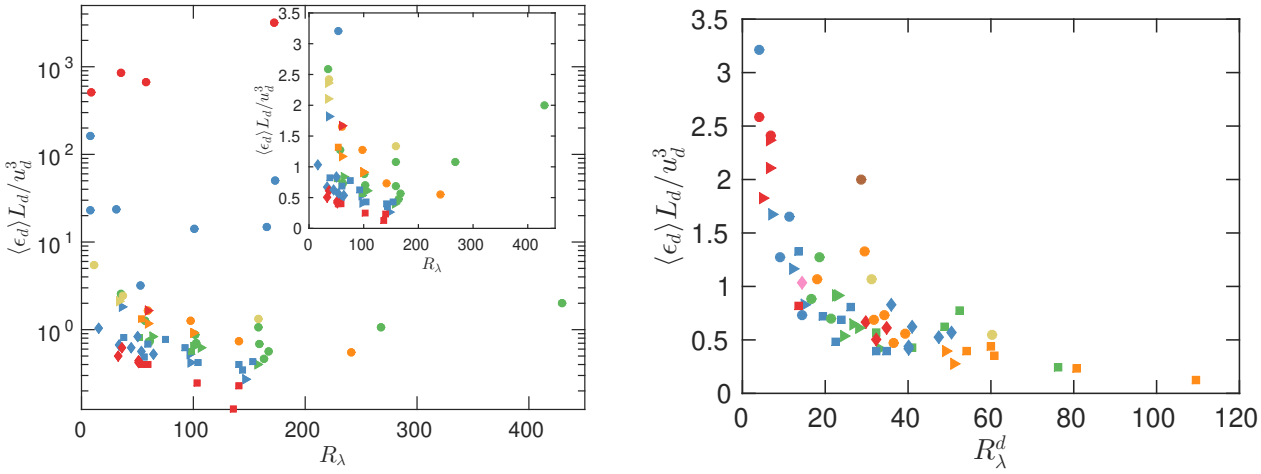

Figure 5.5: Dilatational dissipation normalized by dilatational rms velocity and integral length scale based on dilatational energy spectrum vs (a) total Taylor Reynolds number, R_λ and (b) dilatational Taylor Reynolds number, R_λ^d. In (a) and (b), the color schemes correspond to M_t as in Fig. 5.1 (a) and R_λ as in Fig. 5.1 (b) respectively.

We can rearrange the expression of C_d in terms of C_s as below:

$$C_d \equiv \langle\epsilon_d\rangle \frac{L_d}{u_d^3} \approx \frac{C_s}{\delta}\left(\frac{L_d}{L_s}\right) = \begin{cases} \frac{0.5}{\delta}\frac{L_d}{L_s} \text{ for } R_\lambda^s \to \infty \\ \frac{\left(R_\lambda^s\right)^{-1}}{\delta}\frac{L_d}{L_s} \text{ for } R_\lambda^s \to 0 \end{cases} \tag{5.10}$$

We can see that at high $R_\lambda^s \to \infty$ which corresponds to $\delta \to 0$, $C_d \approx (0.5/\delta)\,(L_d/L_s)$. If at low δ, we assume that L_d and L_s are independent and thus their ratio, L_d/L_s is a constant. In these situation, C_d is inversely proportional to δ. We plot C_d vs δ in Fig. 5.6 (a).

We can see that at low $\delta < 0.1$ and for $R_\lambda > 30$, the normalized dissipation decrease with δ, although with a steeper slope of -1.25 rather that the expected -1 slope. After some considerable scatter at intermediate δ, there seems to be a balance between the dilatational dissipation at small scales and energy at large scales at high δ. For $\delta > 1.0$, the normalized dissipation seems to be hovering around a value which is $O\,(1)$ with no specific trend which might be indicative of a cascade. Further data are required at high R_λ to analyze any scaling in these regions.

The scatter at the intermediate region requires further explanation where δ is less than 0.5

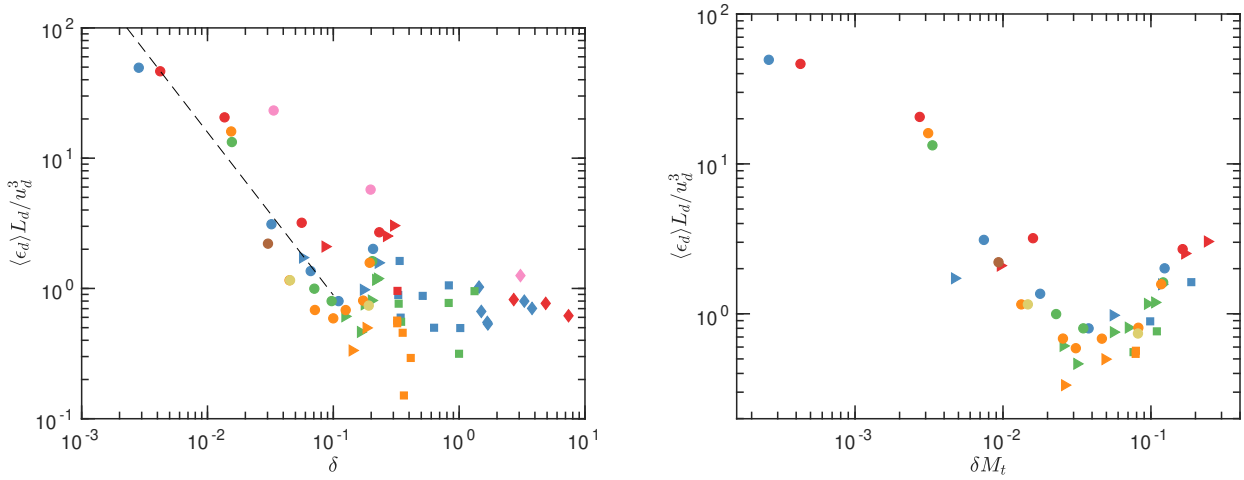

Figure 5.6: Dilatational dissipation normalized by dilatational rms velocity and integral length scale based on dilatational energy spectrum vs (a) δ and (b) δM_t for cases with $D = \delta\sqrt{\delta^2+1}/M_t < 0.5$. In both figures, color scheme corresponds to R_λ as in Fig. 5.1 (b). In (b), the cases where $R_\lambda < 30$ are not plotted. The dashed line in (a) has a power law of -1.25.

and thus the flow field is dominated by the solenoidal velocity field. If modes can interact in these regions, then L_d and L_s are no longer independent. The cascade, if one exists, can then be expected to be driven by the solenoidal mode. The scaling of L_s is assumed to be $u_s'^3/\langle\epsilon_s\rangle$. For the dilatational integral length scale can be assumed to be the product of a characteristic velocity scale and time scale. We assume the mean speed of sound, $\langle c\rangle$ as the velocity scale and the time scale as $u_d'^2/\langle\epsilon_d\rangle$. Thus we assume, L_d as $\langle c\rangle u_d'^2/\langle\epsilon_d\rangle$ and therefore, the ratio L_d/L_s scales as $(M_t^s)^{-1}$ where $M_t^s = u_s'/\langle c\rangle$ is the Mach number based on the solenoidal velocity alone. Since in this regime, δ is still relatively low, we can approximate $M_t^s \approx M_t$. Thus, approximately $L_d/L_s \propto M_t^{-1}$. In the above derivation, we have used the relation $\langle\epsilon_d\rangle/\langle\epsilon_s\rangle \propto \delta^2$. If we substitute the above scaling of L_d/L_s into Eq. 5.10 for high R_λ^s, $R_\lambda^s \to \infty$, we get

$$C_d \equiv \langle\epsilon_d\rangle \frac{L_d}{u_d'^3} \propto 0.5\,(\delta M_t)^{-1} \tag{5.11}$$

Since we assume that the solenoidal mode drives the cascade of dilatational mode if any, we consider the cases where $D < 0.5$, the criterion we derived in Chap. 4 where the solenoidal

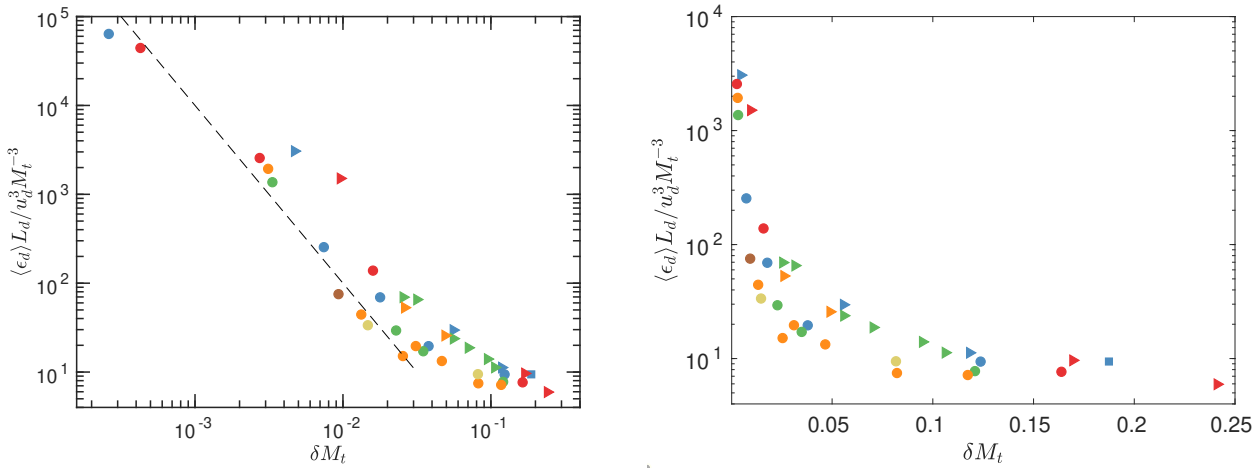

Figure 5.7: Normalized dilatational dissipation with shocklet strength for $D < 0.5$ and $R_\lambda > 30$ vs δM_t (a) in log-log scale and (b) log-linear scale. In both figures, color schemes corresponds to R_λ as in Fig. 5.1 (b). The dashed line in (a) has a power law of -2.

pressure dominates over the acoustic dilatational pressure. We plot the normalized dilatational dissipation versus δM_t for these cases in Fig. 5.6 (b). From the figure, we observe that at low δM_t, the normalized dilatational dissipation decreases with δM_t. This means the large scale motions dominate over small-scale dissipation motions as compressibility increases. This implies that there is no cascade at low δM_t. However, C_d increases with δM_t after a transitional $\delta M_t \approx 0.05$. After this transition, it seems that dissipation dominates over large scale motions indicating there is some sort transfer of energy from large to small scales, perhaps a cascade.

5.5 Criterion for Cascade and Dilatational Dissipative Anomaly

It seems that for $\delta M_t > 0.05$, when dilatational dissipation is normalized by large scale dilatational quantities, the normalized dissipation increases with δM_t. DNS of Wang *et al.* [139] showed that the shocklet strength is proportional to M_t^3. If we can assume that the contributions to dilatational dissipation mainly come from shocklets, one need to normalize the dilatational dissipation taking into account the shocklet strength. Thus we define the new normalized dilatational dissipation as

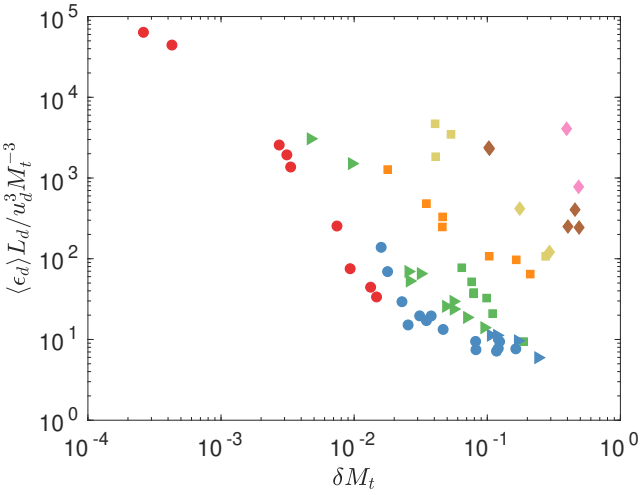

Figure 5.8: Normalized dilatational dissipation with shocklet strength for all cases vs δM_t. In the figure, color scheme corresponds to $D < 0.16$, $0.16 < D < 0.5$, $0.5 < D < 2.25$, $2.25 < D < 10$, $10 < D < 50$, $50 < D < 150$, $150 < D < 1100$.

$$C_d' \equiv M_t^{-3} \langle \epsilon_d \rangle \frac{L_d}{u_d'^3}. \tag{5.12}$$

We plot C_d' versus δM_t for $D < 0.5$ in Figs. 5.7. From the first figure in the log-log plot, C_d' decreases with a power law of -2 but, from the second figure, we can see that after $\delta M_t > 0.1$, the new normalized dilatational dissipation, C_d' approaches to a constant of the $O\,(10)$. Thus we argue that the dissipative anomaly may be possible for the dilatational field when $\delta M_t > 0.1$ at least for cases with $D > 0.5$. In future studies, it would be also be insighful to analyze the spectra of dissipation which might corroborate some of the findings observed here.

In Fig. 5.8, we plot C_d' versus δM_t for all the cases. It is hard to deduce any meaningful conclusions from this figure but one may conjecture that even for all cases, at high δM_t, C_d' seems to asymptote to different constants. Further studies are required to understand the trends.

5.6 Summary

In this chapter, we discussed the scaling of dissipation or dissipative anomaly in compressible turbulence. The major findings are

- We showed that the classical incompressible dissipative anomaly does not hold for compressible turbulence under general compressibility conditions for the total dissipation.

- Dissipative anomaly holds for the solenoidal part of the velocity field when the solenoidal dissipation is normalized using just the solenoidal variables.

- We derived the conditions in terms of δ and M_t where the flow field transitions from solenoidal dissipation dominated regimes to dilatational dominated regimes.

- For the dilatational dissipation, when rescaled with dilatational variables and taking into account the shocklet strength, at least for cases with $D < 0.5$, we might have a cascade for the dilatational part of the velocity field and thus, dissipative anomaly may exist for the dilatational field when $\delta M_t > 0.1$.

6. SPECTRA AND REGIMES IN COMPRESSIBLE TURBULENCE

6.1 Introduction

Turbulence being a multi-scale phenomena, the measure of kinetic energy distribution across scales, the energy spectrum, is pivotal in improving our fundamental understanding. Much less is known about the spectra of compressible turbulence and a clear understanding of its scaling is still missing even after decades of accumulated research.

For homogeneous compressible turbulence, it is convenient to analyze the energy spectrum via Helmholtz decomposition where the velocity field is split into solenoidal ($\nabla.\mathbf{u_s} = \mathbf{0}$) and dilatational ($\nabla \times \mathbf{u_d} = \mathbf{0}$) components. The solenoidal (vortical) part of the energy spectrum is approximately universal when the system is forced solenoidally only [34, 61, 141, 140]. Recently we [35] showed that this aspect is valid even under more general conditions of forcing, provided the spectrum is compensated correctly. The solenoidal energy spectra were found to be similar to that observed for incompressible turbulence. But for the dilatational component, no such collapse was observed.

Numerous scaling laws for the dilatational spectra have been proposed depending on different flow conditions. The turbulent Mach number, $M_t = \langle u_i u_i \rangle^{1/2} / \langle c \rangle$ along with the Taylor Reynolds number, $R_\lambda = \langle \rho \rangle \langle u_i u_i \rangle^{1/2} \lambda / \sqrt{3} \langle \mu \rangle$ have been traditionally used as the parameters to characterize compressible turbulence for the idealized case of homogeneous isotropic turbulence. M_t is also used in the current literature to classify different regimes in compressible turbulence [112]. As an example, recent DNS studies involving both solenoidally forced isotropic and homogeneous shear driven [61, 140] cases report for the dilatational flow field, a transition from pseudosound to acoustic dominated regime. Interestingly, this transitional M_t is non-universal even for solenoidally forced cases. Furthermore, the qualitative effect of M_t on the major dilatational statistics are diminished when the flow field is forced equally in both solenoidal and dilatational modes [144].

From the asymptotic scaling arguments in Chap. 4, Donzis and John [35] have showed that the

parameter space (M_t, R_λ) is insufficient to characterize the complex and rich behavior exhibited by compressible turbulence. We extended the parameter space to include, $\delta = u'_d/u'_s$, the ratio of dilatational to solenoidal rms velocity. In that work and in Chap. 4 , we demonstrated that universal scaling laws can be derived for compressible turbulence by successfully collapsing few major one-point dilatational statistics with non-trivial combinations of δ and M_t. This corresponds to self-similarity of the second kind [6] where pure dimensional analysis cannot be used to derive the scaling exponents. We extend this concept here using the asymptotic and dominant term analysis in Chap. 3 to divide the $\delta - M_t$ phase plane into different physical regimes. We show that the scaling of the dilatational spectra can be explained through this dominant term analysis and our conjectures are supported by high fidelity DNS data which covers a wide range of parameter space comprising of M_t, δ and R_λ.

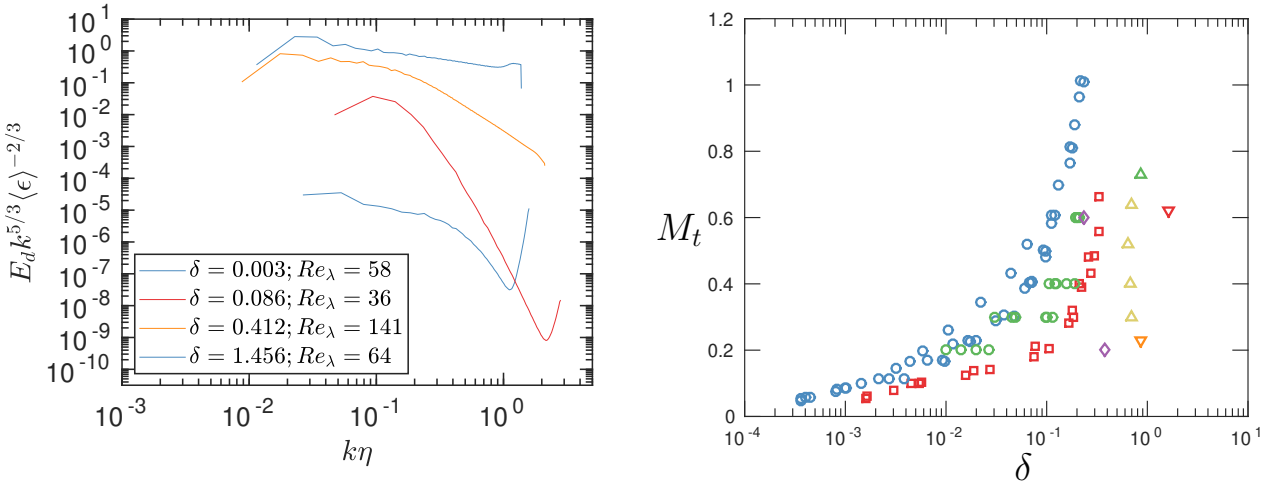

Figure 6.1: (a) Dilatational energy spectra at $M_t \approx 0.1$ for different magnitudes of δ. (b) Current stationary homogeneous simulations in literature discussing dilatational energy spectra on $\delta - M_t$ phase plane.

From a few data from our simulations in Fig .6.1 (a), we can deduce that even at constant $M_t \approx 0.1$, consistent with previous research, the scaling of dilatational energy spectra is contrastingly different at various values of δ which implies that the characteristics of compressible

Turbulence Type	α_p	M_t	Re_λ	Symbol
HIT, S [61]	1.0	0.05-1.02	38-430	○
HIT, S [140]	1.0	0.05-1.02	38-370	○
HIT, S [142]	1.0	1.03	254	○
HIT, S (Present data)	100	0.05-0.6	38-430	●●●●
HIT, D [147]	0.33	0.73	210	▽
HIT, D [144]	0.50	0.30-0.65	196-234	△
HIT, D [83]	0.01	0.23	65	▽
HIT, D [146]	...	0.64	160	▽
HIT, D (Present data)	0.70-0.90	0.04-0.8	30-160	▶▶▶▶
HIT, D (Present data)	0.35-0.70	0.05-0.55	38-154	▲▲▲▲
HIT, D (Present data)	0.1-0.35	0.04-0.25	16-77	▼▼▼
HST[22]	...	0.03-0.66	32-220	□
TF [145]	1.0	0.2,0.6	250	◇

Table 6.1: Available dataset of homogeneous compressible turbulence in the literature and current study; Driving mechanisms are HIT,S (homogeneous isotropic turbulence, solenoidal forcing, circles), HIT, D (homogeneous isotropic turbulence, dilatational forcing, triangles depending on α_p), HST (homogeneous shear, squares) and TF (thermal forcing, rhombus). Color schemes of present data based on R_λ with $R_\lambda < 40$ $40 < R_\lambda < 70$, $70 < R_\lambda < 115$, $115 < R_\lambda < 180$

turbulence depends on both forcing or initial conditions [61, 145, 22, 147, 144, 35]. So far to our best knowledge, there are no satisfactory theoretical analyses to explain the transition observed in these studies. We have compiled the current available data in the literature regarding the energy spectra of homogeneous compressible turbulence and is shown in Fig .6.1 (b) in the $\delta - M_t$ phase plane. The compiled data along with our DNS data used in this section are summarized in Table 6.1. For all figures in this section, the coloring schemes and symbols in Table 6.1 are used unless otherwise specified.

6.2 Background

Many inertial range scaling theories for the dilatational energy spectrum have been proposed. A scaling of k^{-3} is predicted by pseudosound theory [110]. DNS study of Wang *et al.* [140] supports this scaling at low M_t. In their study, the pseudosound part of the dilatational spectra always satisfy the k^{-3} scaling after they split the dilatational spectrum into acoustic and pseudosound components. This scaling of k^{-3} was also predicted by EDQNM studies [112], however the scaling

depends on the particular choice of the damping factor used in their model. The theory predicts a different scaling of $k^{-11/3}$ for a different damping factor which corresponds to the acoustic scaling seen in equipartition. Due to the presence of many complex phenomena in the same flow field, it is indeed expected that dilatational energy spectrum can exhibit multiple scaling laws. Fauchet [112] demonstrated this for low M_t and high R_λ. He found multiple scaling regimes for dilatational spectrum with the acoustic regime at low wavenumbers and pseudo sound at high wavenumbers after assuming that the solenoidal part has a $k^{-5/3}$ scaling. The same observation was made by Wang *et al.* [140] where the pseudosound and acoustic modes dominate at high and low wavenumbers respectively. In fact, they derived a critical wavenumber k_c where this transition occurs which depends on M_t. Beyond a critical $M_t > 0.5$, acoustic mode dominates the entire scaling regime. A similar critical turbulent Mach number, but somewhat smaller (M_t) was reported by Jagannathan and Donzis [61] where the acoustic mode starts to dominate. The high resolution DNS by the same authors at $R_\lambda \approx 430$ and $M_t \approx 0.3$ on a 2048^3 grid did not exhibit a clear plateau that would correspond to a $k^{-5/3}$ inertial range scaling for the dilatational energy spectrum. But for thermally forced simulations [145], a $k^{-5/3}$ scaling was observed. These discrepancies can be resolved when we consider δ as an additional parameter.

These differences have been reported even for mixed solenoidal and dilatational forced simulations. In many simulations, [146, 144, 147, 83] for $M_t \approx 0.2 - 0.75$, a power law scaling of k^{-2} similar to that of Burger's turbulence was observed. Experiments of supersonic compressible plasma turbulence [150] at high M_t have observed a transition from a Kolmogorov like $k^{-5/3}$ scaling to k^{-2} corresponding to Burgers. DNS of compressible turbulence based on Euler equations [49, 76] for isothermal flows popular in astrophysical contexts have observed a k^{-2} scaling at high M_t only under dilatational forcing. The flow we are considering have fluctuations in temperature thus is different from the above flows. Nevertheless our results can help in understanding the trends observed for these astrophysical flows.

So far these discussions point that at same M_t, we can expect multiple scaling for the dilatational energy spectrum depending on the characteristics of forcing. The distribution of energy

across scales would depend on the relative importance of the terms such as advection, pressure dilatation and dissipation terms in the kinetic energy budget equation. Thus it is important to understand the scaling and characteristics of these processes.

The advection terms involve the triple correlation of velocities, thus are non-linear and are responsible for the cascade of energy from large scales to small scales. These terms also drive the transfer between the solenoidal and dilatational modes. Unlike in incompressible turbulence [51, 104], the cascade mechanisms and inertial range dynamics are not well understood in compressible turbulence. Aluie [2, 3] argued for a inertial range cascade similar to incompressible turbulence. DIA and two point EDQM based numerical simulations also supported cascade for compressible turbulence at high M_t [8]. Similar observations were made by Wang *et.al* [143] from their solenoidally forced DNS.

Many studies [42, 114, 61, 118, 108, 3] have been done on the pressure dilatation term which is absent in incompressible turbulence. This term can be split as follows: $\langle p'\theta \rangle = \langle p'_s\theta \rangle + \langle p'_d\theta \rangle$ where $\theta = \partial u'_i/\partial x_i$ is the instantaneous dilatation in the flow field. Here p'_s is the solenoidal pressure obtained by solving the Poisson equation using the solenoidal velocity alone and p'_d is the dilatational pressure, the difference between total and solenoidal pressure [112]. It is important to distinguish the two modes of pressure as both have different effects on the flow evolution [114]. Therefore the ratio of pressure rms (p'_d/p'_s) plays a pivotal in the scaling of dilatational energy spectrum. Refs [61, 140] have studied this ratio for solenoidally forced simulations. Donzis and John [35], based on asymptotic arguments, derived the ratio of pressure in terms of δ and M_t as

$$\frac{p_d^{'}}{p_s^{'}} = D = \frac{\delta\sqrt{\delta^2+1}}{M_t}. \tag{6.1}$$

From the above expression, at low and high δ, D tends to $D \rightarrow \delta/M_t$ and $D \rightarrow \delta^2/M_t$ respectively. Scaling of the ratio of dissipation was already discussed in Chap. 4 .

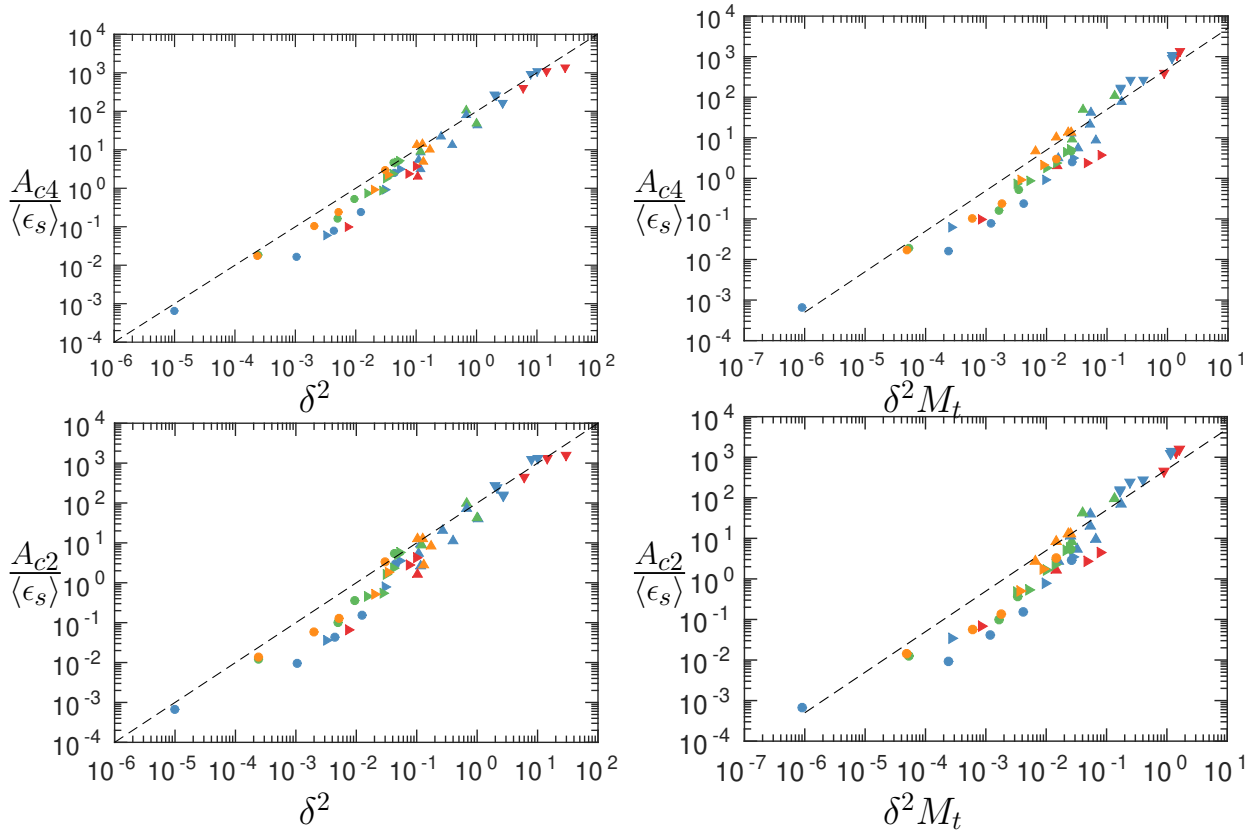

Figure 6.2: Scaling of advection terms. (a) A_{c4} vs δ^2 (b) A_{c4} vs $\delta^2 M_t$ (c) A_{c2} vs δ^2 (d) A_{c2} vs $\delta^2 M_t$. Dashed lines are power law scaling in (a) $(\delta^2)^1$, (b) $(\delta^2 M_t)^{1.0}$, (c) $(\delta^2)^1$ and (d) $(\delta^2 M_t)^{1.0}$.

6.3 Global Scaling Results

Before we discuss the regimes and spectra in compressible turbulence, we first discuss the global scaling of the advection terms given below:

$$A_s : O(1) \tag{6.2a}$$

$$A_{c1} : O(\delta) \tag{6.2b}$$

$$A_{c2} : O\left(\delta^2, \delta^2 M_t\right) \tag{6.2c}$$

$$A_{c3} : O(\delta) \tag{6.2d}$$

$$A_{c4} : O\left(\delta^2, \delta^2 M_t\right) \tag{6.2e}$$

$$A_d : O\left(\delta^3\right). \tag{6.2f}$$

These are from our asymptotic analysis in Chap. 3. Here the notation $O\left(A, B, C, D, ...\right)$ means the variable can have one of the order of magnitude from $O\left(A\right)$, $O\left(B\right)$, $O\left(C\right)$, $O\left(D\right)$, ... depending of flow conditions. The order of magnitude terms with a combination of both δ and M_t correspond to large wavelength whereas terms with only δ correspond to small wavelength. We have neglected those order of magnitude terms where the term equates itself to zero. For example, the scaling of solenoidal viscous term, $\langle \epsilon_s \rangle$ is $O\left(1, M_t, M_t^2\right)$. But from Eq. A.2g that for $O\left(M_t^2\right)$, the solenoidal viscous term equates to zero. Since for our cases, $M_t < 1.0$, scaling of the solenoidal dissipation can be written as

$$\langle \epsilon_s \rangle = O\left(1\right) \tag{6.3a}$$

Similarly for the dilatational dissipation, the scaling is $\langle \epsilon_d \rangle = O\left(\delta^2, \delta^2 M_t, \delta^2 M_t^2\right)$ but similar to solenoidal dissipation, the $O\left(\delta^2 M_t^2\right)$ term equates itself to zero from Eq. 3.18f. Therefore

$$\langle \epsilon_d \rangle = O\left(\delta^2, \delta^2 M_t\right) \tag{6.3b}$$

To test Eq. 6.2a to Eq. 6.2f, in Figs. 6.2 and 6.3, we plot the standard deviation of the advection terms normalized with the mean solenoidal dissipation. In incompressible turbulence, it is common to use total dissipation to normalize the energy budget terms. Instead of total dissipation, we use solenoidal dissipation here since it is least affected by compressibility from the asymptotic analysis. The pure dilatational advection, $A_d / \langle \epsilon_s \rangle$ scales as δ^3 from Eq. 6.2f. Similarly, the scaling of other advection terms can be found out. From 6.3 (a), we observe that $A_d / \langle \epsilon_s \rangle$ scales well with δ^3 with some scatter at high δ. The scaling of the term at intermediate δ has a power law slightly greater than one with δ^3.

From Fig.6.2 (b), A_{c4} seems to scale well with $\delta^2 M_t$. There seems to be a slight R_λ effect at

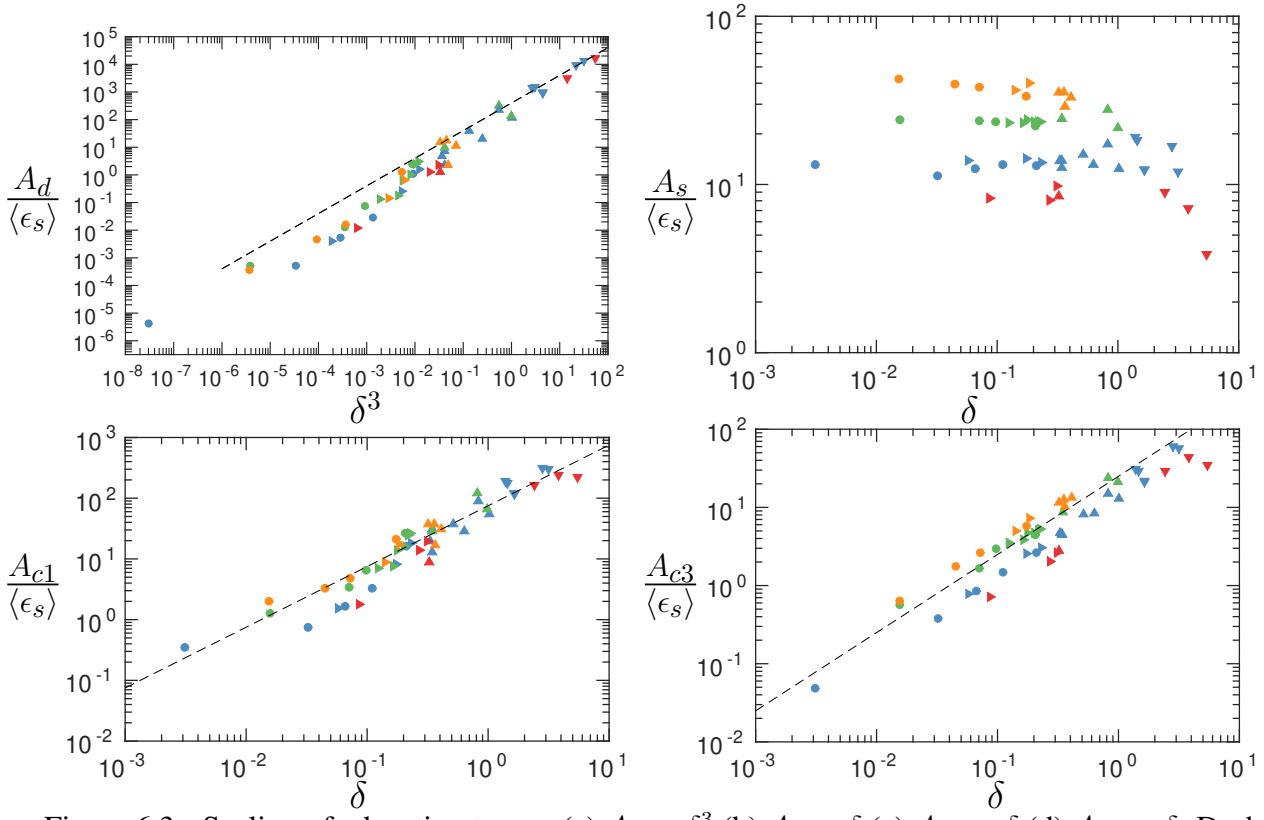

Figure 6.3: Scaling of advection terms. (a) A_d vs δ^3 (b) A_s vs δ (c) A_{c1} vs δ (d) A_{c3} vs δ. Dashed lines are power law scaling in (a) $(\delta)^3$, (c) $(\delta)^1$ and (d) $(\delta)^1$.

intermediate values of $\delta^2 M_t$ around $10^{-4} - 10^{-1}$. Apart from this range, we observe good collapse of data at low and high $\delta^2 M_t$. There is some scatter for A_{c4} with δ^3 as seen in Fig .6.2 (b). The scaling of A_{c2} appearing in the solenoidal kinetic energy equation is similar to that of A_{c4} in the dilatational kinetic energy in Figs. 6.2 (c-d). It is expected since these terms are responsible for the inter-modal transfer.

As expected, the pure solenoidal advection term is independent of compressibility in Fig. 6.3 (b), however its strength increases with R_λ. However terms A_{c3} and A_{c1} scale well with δ. Later we demonstrate that these terms correspond to the pseudosound theory. It is consistent that A_{c3} and A_{c1} terms scale well with δ since the pseudosound is a high wavenumber phenomena.

We analyze the scaling of the ratio of dissipation and is shown in Fig. 6.4. In the earlier Chap. 4, we arrived at δ^2 scaling using phenomenological arguments but here we got the scaling laws of

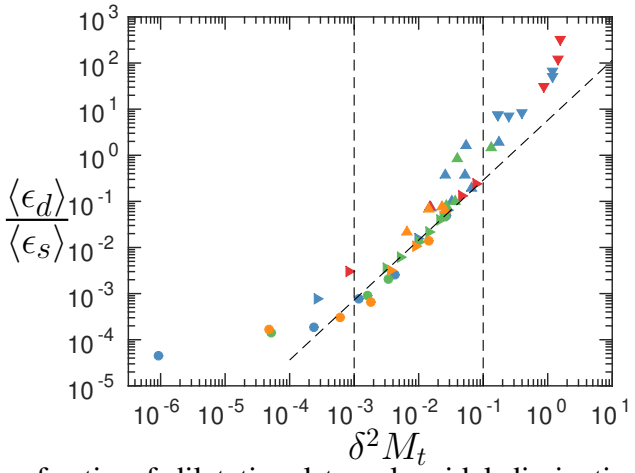

Figure 6.4: Scaling of ratio of dilatational to solenoidal dissipation ratio: $\langle \epsilon_d \rangle / \langle \epsilon_s \rangle$ vs $\delta^2 M_t$. Dashed line is power law scaling corresponding to $(\delta^2 M_t)^{1.3}$.

δ^2 and $\delta^2 M_t$ from the asymptotic analysis in Chap. 3 as seen from Eq. 6.3a and Eq. 6.3b. The ratio scales with δ^2 but with some scatter at intermediate δ as we saw in Chap. 4. But these cases seems to scale well with $\delta^2 M_t$ in Fig. 6.4.

In conclusion, it can be concluded that the scaling from the asymptotic analysis agrees with DNS data and assumptions made so far are justified for this range of parameters considered. This multiple scaling regimes observed for dissipation and advection terms will be used to divide the $\delta - M_t$ phase plane.

6.4 Energy Spectra

We demonstrate that the classical scaling laws based on K41 self-similarity theory of incompressible turbulence for energy spectrum in compressible turbulence are inadequate. The K41 theory suggests a universal behaviour when the total energy spectrum,

$$E(k) = \langle \rho \rangle \oint_{|k-dk'|<|k'|<|k+dk'|} \hat{u}_i(k)\, \hat{u}_i^*(k)\, dk' \tag{6.4}$$

is compensated using the total dissipation, $\langle \epsilon \rangle$ and the Kolmogorov length scale based on total flow field variables, $\eta = (\mu^3 / \langle \epsilon \rangle)^{1/4}$ where "*" is the complex conjugate. Previous research [61, 141,

140] have shown that the total spectra collapse for solenoidally forced cases and compressibility effects are confined to high wavenumbers. In these studies, the strength of dilatational motions was much lower than solenoidal motions, ie $\delta \ll 1$. However recently we showed [62] that under general conditions of forcing and when the dilatational component is at least as dominant as the solenoidal mode, both the compensated total and solenoidal spectra $\left(\int_0^\infty E_s\left(k\right) dk = \langle\rho\rangle\langle \mathbf{u_s} \cdot \mathbf{u_s}\rangle/2\right)$ based on the total flow field do not collapse the data.

We can define a solenoidal Kolmogorov length scale, $\eta_s = \left(\mu^3/\langle\rho\rangle\langle\epsilon_s\rangle\right)^{1/4}$ based on solenoidal dissipation alone if we can assume Kolmogorov like cascade for the solenoidal mode independent of the dilatational mode. We can relate them to the total variables as: $\langle\epsilon\rangle/\langle\epsilon_s\rangle \propto \left(\delta^2 + 1\right)$ or $\left(\delta^2 M_t + 1\right)$ and $\eta/\eta_s \propto 1/\left(1+\delta^2\right)^{1/4}$ or $1/\left(1+\delta^2 M_t\right)^{1/4}$. These relations can be derived from the scaling of the dissipation from our asymptotic analysis. In the limit $\delta^2, \delta^2 M_t \to 0$, both the solenoidal and total viscous length scales are almost the same whereas in the other limit of $\delta^2, \delta^2 M_t \gg 0$, the solenoidal and total viscous length scales are different. Therefore when comparing a particular mode of the energy spectra across different flow conditions, the spectra have to be compensated with its own respective mode as opposed to the total field commonly done in the literature.

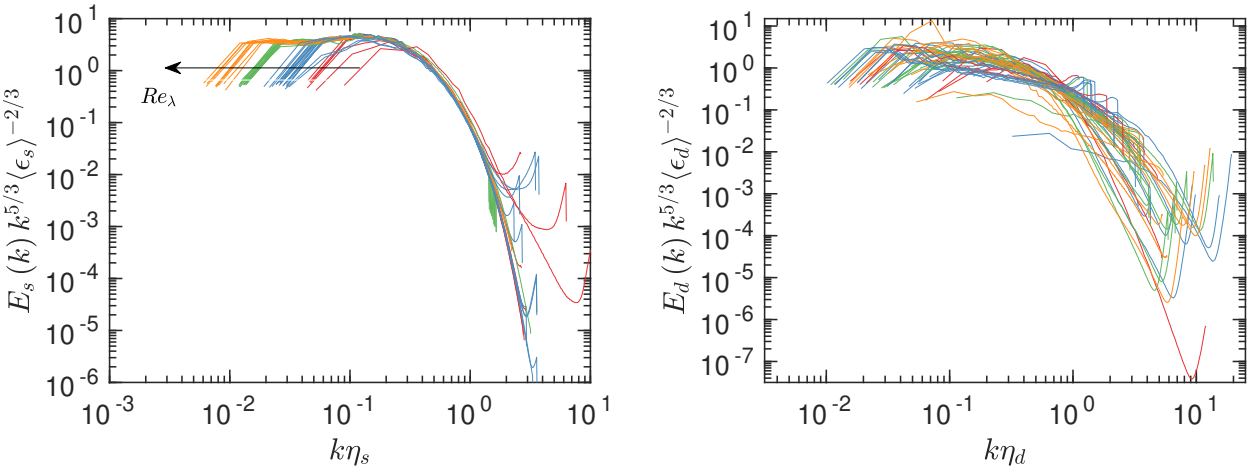

Figure 6.5: Kolmogorov compensated solenoidal (a) and dilatational (b) spectra.

We find excellent collapse of solenoidal energy spectra in Fig. 6.5 (a) when they are compensated using just the solenoidal dissipation, $\langle \epsilon_s \rangle$ and η_s for the wide range of conditions considered in this study. The spectra are similar to the incompressible energy spectrum with the inertial range increasing with Taylor Reynolds number, R_λ. Thus, we can conclude that the effect of compressibility on the solenoidal spectra in general is weak, at least for $k\eta_s < 2.0$.

It is intuitive to adopt a similar strategy for the dilatational part of the energy spectrum. From Fig. 6.5 (b), we observe no such collapse for the compensated dilatational energy spectra $\left(\int_0^\infty E_d\left(k\right) dk = \langle\rho\rangle\langle \mathbf{u_d} \cdot \mathbf{u_d} \rangle/2\right)$ although we used just the $\langle \epsilon_d \rangle$ and $\eta_d = \left(\mu^3/\langle\rho\rangle\langle \epsilon_d \rangle\right)^{1/4}$ for normalization. The dilatationally forced cases (high δ) show higher energy content at low wavenumbes compared to solenoidally forced cases. In addition, we also see different scaling behaviors depending on the flow conditions. Therefore, the data seem to suggest different physical regimes in the parameter space in which distinct characteristics can be observed. In the reminder of this section, we isolate particular scaling patterns by delineating the parameter space into different regimes.

The definition of the energy spectrum is straightforward in the incompressible case since density is constant. But in compressible turbulence, density is no longer a constant which leads multiple ways of defining the kinetic energy spectrum. The most common ways to define energy spectrum are

$$E_d^r\left(k\right) = \langle\rho\rangle \oint_{|k-dk'|<|k'|<|k+dk'|} \hat{u}_{di}(k)\, \hat{u}_{di}^*(k)\, dk' \tag{6.5a}$$

$$E_d^w\left(k\right) = \oint_{|k-dk'|<|k'|<|k+dk'|} \widehat{\sqrt{\rho}u}_{di}(k)\, \widehat{\sqrt{\rho}u}_{di}^{\,*}(k)\, dk' \tag{6.5b}$$

which correspond to Reynolds and the average introduced by Kida and Orszag [65] respectively. Since for homogeneous turbulence, the Favre and Reynolds averaging are the same [14, 52, 121], we do not discuss the Favre averaging here. We compare both types of averaging and the compressibility effects on it.

6.5 Compressible Regimes and Dilatational Energy Spectrum

We divide the $\delta - M_t$ phase into different physical regimes to explain the diverse behaviour exhibited by the dilatational energy spectra. For this, using our asymptotic analysis developed in Chap. 3, we systematically study the order of magnitude equations. We neglect the pure dilatational term, A_d, which is $O(\delta^3)$ to simplify the analysis and establish the conditions where dilatational kinetic energy cascade is possible by studying the different terms at increasing order of δ in the expansion. The lowest order is $O(\delta)$ in these equations from Eq. 3.18a to Eq. 3.18g. We reproduce it below:

$$O(\delta) : \left\langle \widehat{w}_i^d \left\{ v_j^s \widehat{\frac{\partial w_i^s}{\partial \eta_j}} \right\}^d \right\rangle_k = \left\langle - \widehat{w}_i^d \left\{ \frac{1}{\sqrt{\rho}} \widehat{\frac{\partial p^s}{\partial \eta_i}} \right\}^d \right\rangle_k. \tag{6.6a}$$

The above equation states that the correlation between the dilatational velocity and the solenoidal mode of velocity is balanced by the pressure strain correlation consisting of dilatational velocity and solenoidal pressure. Since in the current database, M_t is less than unity for all cases, the only other term that can be $O(\delta)$ is

$$O\left(\frac{\delta^2}{M_t}\right) : \left\langle w_i^d \frac{\partial w_i^d}{\partial \tau'} \right\rangle = \left\langle - \widehat{w}_i^d \left\{ \frac{1}{\sqrt{\rho}} \widehat{\frac{\partial p^d}{\partial \eta_i}} \right\}^d \right\rangle_k. \tag{6.6b}$$

This equation can be $O(\delta)$ when $\delta/M_t \approx O(1)$ and it represent simply acoustic oscillations. We can deduce from these equations, a cascade mechanism cannot be supported since all terms are predominantly at small scales and there is no dissipation term in these equations.

The next order in δ in the dilatational kinetic energy equations reads as:

$$\begin{aligned} O(\delta^2) : \left\langle w_i^d \frac{\partial w_i^d}{\partial \tau} \right\rangle + \left\langle w_i^d \left\{ v_j^d \widehat{\frac{\partial w_i^s}{\partial \eta_j}} + v_j^s \widehat{\frac{\partial w_i^d}{\partial \eta_j}} + w_i^s \widehat{\frac{\partial v_j^d}{\partial \eta_j}} \right\}^d \right\rangle_k = \left\langle - \widehat{w}_i^d \left\{ \frac{1}{\sqrt{\rho}} \widehat{\frac{\partial p^d}{\partial \xi_i}} \right\}^d \right\rangle_k + \\ \left\langle \frac{\widehat{w}_i^d}{\sqrt{\rho}} \left\{ \frac{\partial}{\partial \eta_j} \frac{\partial \widehat{v}_i^d}{\partial \eta_j} + \frac{\partial}{\partial \eta_j} \frac{\partial \widehat{v}_j^d}{\partial \eta_i} + \frac{\partial}{\partial \eta_i} \frac{\partial \widehat{v}_j^d}{\partial \eta_j} \right\}^d \right\rangle_k \end{aligned} \tag{6.6c}$$

$$O\left(\delta^2 M_t\right) : \left\langle \widehat{w}_i^d \left\{ w_i^s \widehat{\frac{\partial v_j^d}{\partial \xi_j}} + v_j^d \widehat{\frac{\partial w_i^s}{\partial \xi_j}} + v_j^s \widehat{\frac{\partial w_j^d}{\partial \xi_j}} \right\}^d \right\rangle_k = 2 \left\langle \widehat{w}_i^d \left\{ \frac{\partial}{\partial \xi_j} \frac{\partial \widehat{v}_i^d}{\partial \eta_j} + \frac{\partial}{\partial \xi_i} \frac{\partial \widehat{v}_j^d}{\partial \eta_j} + \frac{\partial}{\partial \eta_i} \frac{\partial \widehat{v}_j^d}{\partial \xi_j} \right\}^d \right\rangle_k . \tag{6.6d}$$

Here in these equations, we do see the viscous dissipation terms needed for a cascade and also the multi-scale nature is apparent. The coupling between scales can be seen in Eq. 6.6d where the A_{c4} term corresponding to low wavenumber is balanced by the $\langle \epsilon_d \rangle$ in the RHS that has mixed derivatives in both large and small wavelengths. Although the kinetic energy is not a conserved quantity in compressible turbulence, Aluie [2] argues for an inertial range similar to that of incompressible turbulence. We can interpret Eq. 6.6d as the balance between a transfer term represented by the A_{c4} and dilatational dissipation, $\langle \epsilon_d \rangle$. Thus when $\delta^2 M_t$ is large, motions corresponding to different wavelengths in the dilatational flow field are coupled as they interact with each other similar to incompressible turbulence. Thus we can expect a cascade of dilatational kinetic energy from large to small scales with dilatational dissipation as the rate of energy transfer.

But the actual dissipation has to happen at high wavenumbers and that can be observed in Eq. 6.6c where dilatational dissipation is at high wavenumbers. We thus can surmise that the cascade would be more efficient when these two equations are of the same order. Such a scenario is possible when

$$\frac{\delta^2 M_t}{\delta^2} \approx O(1) \equiv M_t \approx O(1). \tag{6.7}$$

This conclusion is consistent with previous simulations which have reported a transition from pseudosound to cascade like phenomenon at high M_t [143, 146, 140, 61, 22]. But the transition M_t in these studies is non-universal and would depend on the exact nature of forcing and viscous property of the gas. This we argue is because the above criterion does not have a δ dependency.

If one can conceive a situation where $\delta \ll 1$ but with high M_t, the non-cascade physics represented by $0\,(\delta)$ in Eq. 6.6a will always dominate over cascade physics represented by higher order δ equations of Eq. 6.6c and Eq. 6.6d. This is indeed what we observe in the simulations of Wang

et al.[23] with bulk viscosity. The bulk viscosity in the flow field results in more efficient damping of the dilatational motions resulting in a much lower δ compared to simulations with no bulk viscosity. No transition was observed and pseudosound scaling continued for M_t as high as 0.6 for HIT simulations with bulk viscosity.

Thus in order to separate the non-cascade and cascade regimes, one should compare the relative magnitude of the different orders in δ. Both $O(\delta^2 M_t)$ and $O(\delta^2)$ have to greater than $O(\delta)$ for cascade to occur. In all the cases we are currently studying with $M_t < 1.0$, always $\delta^2 M_t < \delta^2$. Thus $\delta - M_t$ phase plane is divided based on the relative strength of $O(\delta^2 M_t)$ and $O(\delta)$ resulting in

$$\frac{\delta^2 M_t}{\delta} = \delta M_t. \tag{6.8}$$

When this criterion δM_t is less than a particular threshold, non-cascade physics would dominate but the cascade mechanisms start to become prominent as δM_t increases. Therefore we divide the $\delta - M_t$ phase plane broadly into three regimes based on the δM_t as below using our DNS data:

- $\delta M_t < 0.01$: No cascade regime
    1. Pseudosound regime
    2. Weak equipartition
- $0.01 < \delta M_t < 0.1$: Transition regime
- $\delta M_t > 0.1$: Cascade regime
    1. Solenoidal driven cascade regime
    2. Wave steepening regime

Extra criteria other than δM_t are required to further subdivide the regimes. We depict the divided $\delta - M_t$ phase plane in Figs .6.6 along with the physical regimes before we proceed further. Fig .6.6 (a) is the intermediate phase plane. Here we have excluded the regimes $0.3 < \delta < 1.0$. We assume that the pure dilatational advection, $A_d \ll 1$ and $A_d \gg 1$ in the limits $\delta < 0.3$ and $\delta > 1$

respectively. The final $\delta - M_t$ decomposition is given in Fig.6.6 (b) with all flow configurations. In the rest of this chapter, we explain systematically on how we divided the $\delta - M_t$ phase plane.

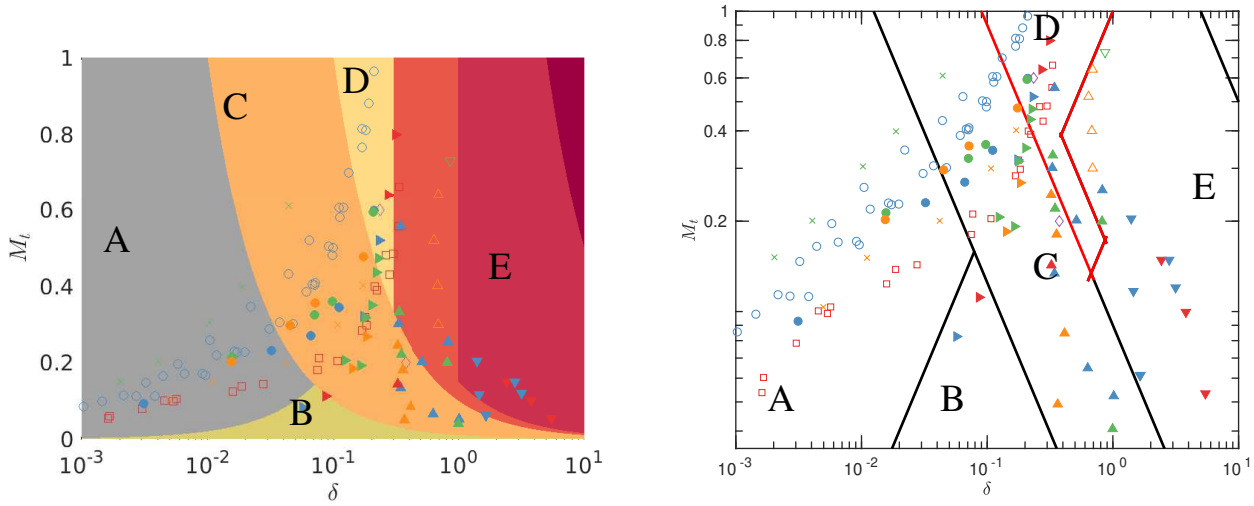

Figure 6.6: $\delta - M_t$ phase plane, intermediate division (a) and final division (b); In both figures, A: pseudosound regime, B: classical weak equipartition, C: transition regime from non-cascade to cascade, D: solenoidal dominated cascade regime, E: wave steepening regime.

6.5.1 No Cascade Regime

This non-cascade regime of low δM_t can be further classified into two. For $\delta M_t < 0.01$, one of the most dominant term in the dilatational kinetic energy equations (Eq. 3.18a -Eq. 3.18f) is $O(\delta)$ and we reproduce it below:

$$O(\delta) : \left\langle \widehat{w}_i^d \left\{ v_j^s \widehat{\frac{\partial w_i^s}{\partial \eta_j}} \right\}^d \right\rangle_k = \left\langle -\widehat{w}_i^d \left\{ \widehat{\frac{1}{\sqrt{\rho}} \frac{\partial p^s}{\partial \eta_i}} \right\}^d \right\rangle_k \tag{6.9a}$$

Previously we have seen that this equation cannot support a cascade. The equation corresponding to $O(\delta)$ in the solenoidal kinetic energy equation is given below:

$$\left\langle \widehat{w}_i^s \left\{ v_j^d \widehat{\frac{\partial \widehat{w}_i^s}{\partial \eta_j}} + v_j^s \widehat{\frac{\partial \widehat{w}_i^d}{\partial \eta_j}} + w_i^s \widehat{\frac{\partial v_j^d}{\partial \eta_j}} \right\}^s \right\rangle_k = -\left\langle \widehat{w}_i^s \left\{ \widehat{\frac{1}{\sqrt{\rho}} \frac{\partial p^d}{\partial \xi_i}} \right\}^s \right\rangle_k \tag{6.9b}$$

Turbulence Type	M_t	δ	δM_t	Symbol
HIT, S [61]	0.3	0.09	0.02	N/A
HIT, S [140]	0.3-0.4	0.037-0.068	0.01-0.03	○
HIT, S,BV [23]	0.4-0.6	0.019-0.044	0.007-0.026	×
HST[22]	0.14-0.21	0.019-0.076	0.002-0.015	□
HST, BV[23]	0.20	0.042	0.008	×

Table 6.2: Table illustrating the transition from pseudosound for a wide range of driving mechanisms. Driving mechanisms are HIT,S (homogeneous isotropic turbulence, solenoidal forcing, circles), HIT, S, BV (homogeneous isotropic turbulence, solenoidal forcing with ratio of bulk to shear viscosity equals 30, crosses), HST (homogeneous shear, squares) and HST,BV (homogeneous shear with ratio of bulk to shear viscosity equals 30.)

This equation looks very similar to the governing equation derived by Wang *et al.* [140] for the dilatational pressure in the pseudo-sound regime in terms of u^d and u^s. The dilatational pressure here does not involve any time derivative thus dilatational pressure does not have the acoustic nature of pressure in the weak equipartition regime. If we assume $\delta \approx M_t^2$, one can use the energy equation to derive the governing equation for the dilatational velocity [140] in terms of solenoidal pressure and velocity. The dilatational components in this regime are in equilibrium with the solenoidal field and important dilatational flow statistics can be completely derived from the solenoidal flow field alone. Wang *et al.* [140] has the detailed derivation of the pseudosound velocity and pressure.

The other possible dominant term in the regime, $\delta M_t < 0.01$ corresponds to the $O\left(\delta^2/M_t\right)$ and is given below:

$$O\left(\frac{\delta^2}{M_t}\right) : \left\langle w_i^d \frac{\partial w_i^d}{\partial \tau'} \right\rangle = \left\langle - \widehat{w}_i^d \left\{ \frac{1}{\sqrt{\rho}} \widehat{\frac{\partial p^d}{\partial \eta_i}} \right\}^d \right\rangle_k \tag{6.9c}$$

This equation is the wave equation corresponding to weak equipartition where there is oscillatory exchange of energy between dilatational pressure and velocity. For a given δ, in the low δ regime, this equation can be $O\left(\delta\right)$ when $M_t \ll 1$ for a given δ. Next we discuss the spectral behavior of the dilatational spectrum corresponding to these two non-cascade regimes in detail.

6.5.1.1 *Pseudosound Regime*

This regime can be classified as the region in the $\delta - M_t$ phase plane where along with criterion $\delta M_t < 0.01$, an extra condition has to be satisfied. It can be derived by comparing the relative magnitude of Eq. 6.9a and Eq. 6.9c. It is

$$\delta / \frac{\delta^2}{M_t} > 1/C \implies \frac{\delta}{M_t} < C \tag{6.10}$$

The parameter $D = \delta \left(\sqrt{\delta^2 + 1}\right) / M_t \rightarrow \delta / M_t$ when $\delta \rightarrow 0$ or at low δ. Thus we can combine the two criteria for pseudosound as

$$(\delta, M_t) : [\delta M_t < 0.01, D < 0.5] \tag{6.11}$$

The notation "[]" implies that both the conditions inside the brackets must be satisfied. The pseudosound regime is depicted in Figs.6.6 (a) and (b) as regime "A". Pseudosound regime is also highlighed in Fig. 6.9 (a). We have also included the pseudosound scaling cases from other studies [140, 22, 23] for reference. We summarize the transitional parameters where the system diverges from the pseudosound phenomena in the Table 6.2. We observe from the table that in the available literature, the transitional M_t ranges from as low as 0.2 for the homogeneous shear forced turbulence [22] to 0.6 for homogeneous isotropic turbulence with the ratio $\mu_b/\mu = 30$ [23]. This shows that under general conditions of forcing, even at low compressibility levels, M_t alone is insufficient to characterize this transition. However, for all cases, $\delta M_t \approx 0.01$ at the transition which we are proposing.

In Figs. 6.7 (a-d), we plot the dilatational energy spectra based on Reynolds and Kida averaging in the pseudosound regime. In the top figures, the normalization proposed by Wang *et al.* [140] is used for the pseudosound regime. For the Reynolds averaged spectra in Fig.6.7 (a), there seems to be a weak Reynolds number effect. The spectra in this figure look consistent with that reported in Wang *et al.* [140] and the k^{-3} scaling regime increases with R_λ. The spectral bump in the figure is similar to that observed in the solenoidal pressure which again points to the direct effect of the

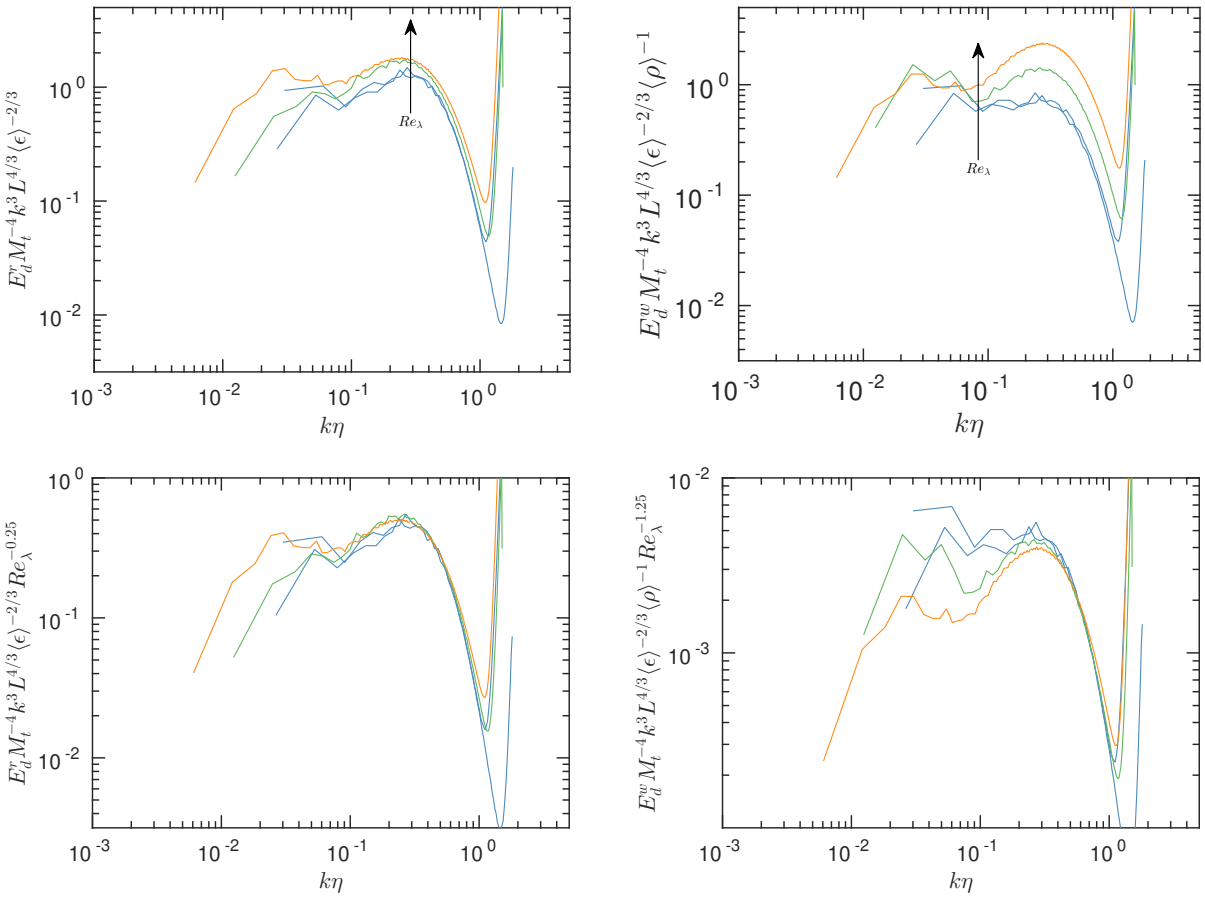

Figure 6.7: Dilatational spectra in the pseudo sound regime, $(\delta, M_t)\, d : [\delta M_t < 0.01, D < 0.5]$, Reynolds averaged compensated spectra (a),(c) and Kida averaged compensated spectra (b),(d).

solenoidal field on the dilatational spectra in this regime. The Reynolds number dependence is more prominent for Kida averaging as seen in Fig. 6.7 (b). For both averages, we try to include the R_λ effects in Figs .6.7 (c-d). The spectra collapse for both averages at high wavenumbers. However a strong power law of $R_\lambda^{-5/4}$ is required for Kida averaged spectra compared to a milder power law of $R_\lambda^{-1/4}$ for Reynolds averaged spectra. This apparent difference in power law and minor qualitative changes in the two averages have to be investigated thoroughly in the future.

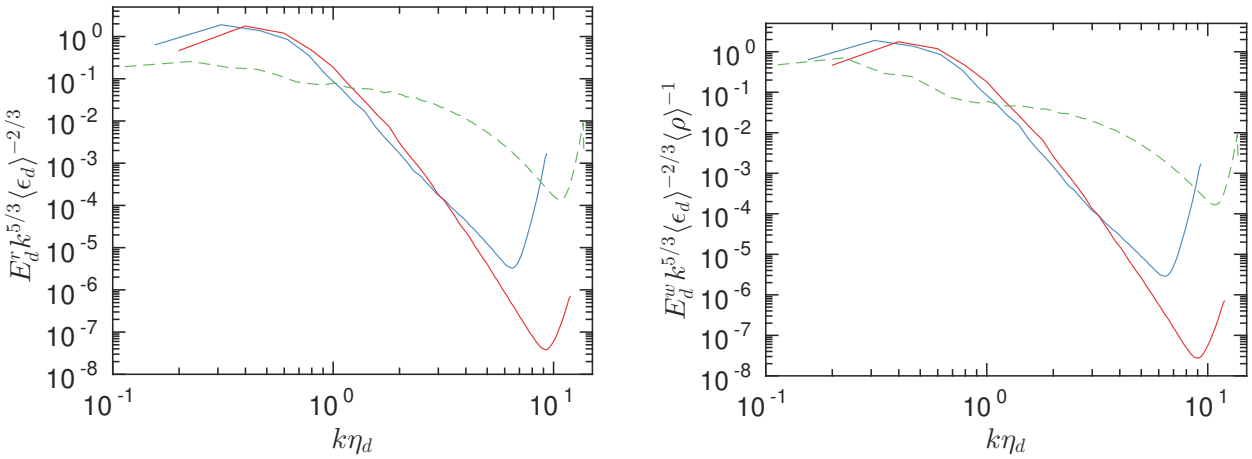

Figure 6.8: Dilatational spectra in the equipartition regime, (δ, M_t) : $[\delta M_t < 0.01, D > 0.5]$, Reynolds averaged compensated spectra (a) and Kida averaged compensated spectra (b).

6.5.1.2 Classical Weak Equipartition

The criteria for classical weak equipartition is defined as

$$(\delta, M_t) : [\delta M_t < 0.01, D > 0.5] \,. \tag{6.12}$$

The dilatational spectra in the equipartition regime along with a pseudosound case for reference is shown in Figs. 6.8 (a-b). In Figs. 6.6 (a-b), we identify weak equipartition regime as "B" in the $\delta - M_t$ phase plane. The regime is also shown in Fig. 6.9 (b). Here, we normalize the dilatational spectra using K41 theory but with just using dilatational dissipation, $\langle \epsilon_d \rangle$ and Kolmogorov length scale, $\eta_d = (\langle \mu \rangle^3 / \langle \epsilon_d \rangle)^{1/4}$. From the figures, it is clear that the differences between the two averages are negligible. For the pseudosound regime, most of the energy reside at high wavenumbers. On the contrary, in the classical weak equipartition regime, most of the energy are in the low wavenumbers of the spectra. And there is negligible energy content at high wavenumbers pointing to the absence of cascade. This corresponds physically to the acoustic oscillations at low wavenumbers where the energy is transferred to and fro between the potential energy stored in dilatational pressure and the kinetic energy corresponding to dilatational velocity

field as proposed by Erlebacher and Sarkar [118, 43]. We have a scale separation between the acoustic and turbulent time scales in this regime. Therefore, dilatational flow field is completely independent of the solenoidal flow field contrary to what we see in the pseudosound regime. We highlight the non-cascade regimes–pseudosound and weak equipartition– in Figs. 6.9 (a) and (b) respectively.

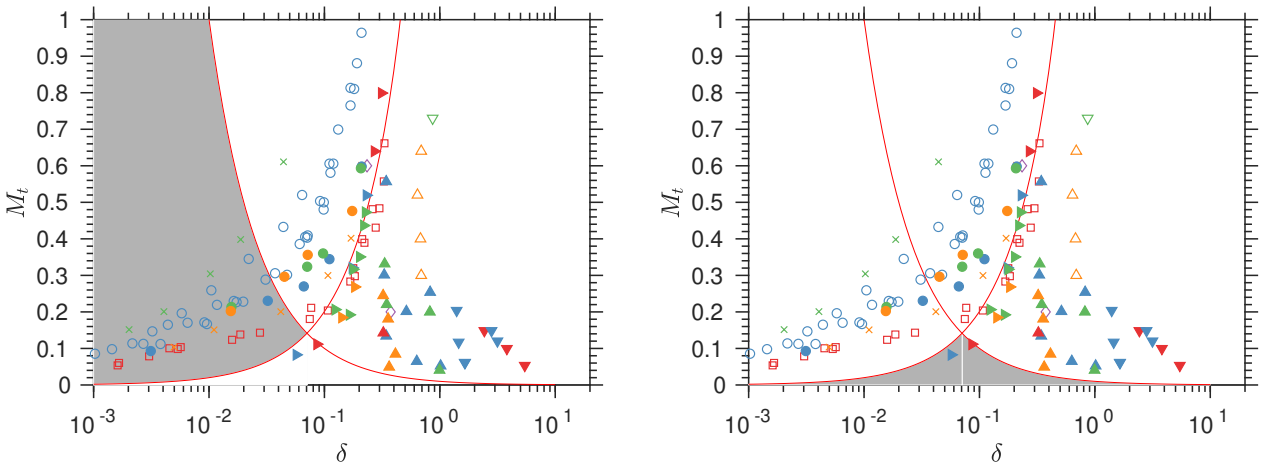

Figure 6.9: Non-cascade regimes in $\delta - M_t$ phase plane. (a) Pseudosound and (b) Weak equipartition.

6.5.2 Cascade Regime: Solenoidally Driven Cascade

The $O\left(\delta^2 M_t\right)$ or other higher order terms begin to dominate over the $O\left(\delta\right)$ for the regimes $\delta M_t > 0.1$ and $\delta < 0.3$. The dominant equations at the higher $O\left(\delta^2\right)$ in the dilatational kinetic energy from Eq. 3.18a to Eq. 3.18g are

$$O\left(\delta^2 M_t\right) : \left\langle \widehat{w}_i^d \left\{ w_i^s \widehat{\frac{\partial v_j^d}{\partial \xi_j}} + v_j^d \widehat{\frac{\partial w_i^s}{\partial \xi_j}} + v_j^s \widehat{\frac{\partial w_j^d}{\partial \xi_j}} \right\}^d \right\rangle_k = 2 \left\langle \widehat{w}_i^d \left\{ \frac{\partial}{\partial \xi_j} \frac{\partial \widehat{v}_i^d}{\partial \eta_j} + \frac{\partial}{\partial \xi_i} \frac{\partial \widehat{v}_j^d}{\partial \eta_j} + \frac{\partial}{\partial \eta_i} \frac{\partial \widehat{v}_j^d}{\partial \xi_j} \right\}^d \right\rangle_k \tag{6.13a}$$

$$O\left(\delta^2\right) : \left\langle w_i^d \frac{\partial w_i^d}{\partial \tau} \right\rangle + \left\langle w_i^d \left\{ v_j^d \widehat{\frac{\partial w_i^s}{\partial \eta_j}} + v_j^s \widehat{\frac{\partial w_i^d}{\partial \eta_j}} + w_i^s \widehat{\frac{\partial v_j^d}{\partial \eta_j}} \right\}^d \right\rangle_k = \left\langle - \widehat{w}_i^d \left\{ \frac{1}{\sqrt{\rho}} \widehat{\frac{\partial p^d}{\partial \xi_i}} \right\}^d \right\rangle_k + \left\langle \frac{\widehat{w}_i^d}{\sqrt{\rho}} \left\{ \frac{\partial}{\partial \eta_j} \frac{\partial \widehat{v}_i^d}{\partial \eta_j} + \frac{\partial}{\partial \eta_j} \frac{\partial \widehat{v}_j^d}{\partial \eta_i} + \frac{\partial}{\partial \eta_i} \frac{\partial \widehat{v}_j^d}{\partial \eta_j} \right\}^d \right\rangle_k \tag{6.13b}$$

$$O\left(\frac{\delta^2}{M_t}\right) : \left\langle w_i^d \frac{\partial w_i^d}{\partial \tau'} \right\rangle = \left\langle - \widehat{w}_i^d \left\{ \frac{1}{\sqrt{\rho}} \widehat{\frac{\partial p^d}{\partial \eta_i}} \right\}^d \right\rangle_k \tag{6.13c}$$

The first equation above is the bridge between large and small wavelengths where the energy at large scales is transferred to smaller scales. All the equations above become the same order of magnitude when $M_t \approx 0\,(1)$ and at such a situation, we get complete coupling of the scales through the cross advection and dissipation terms. These cross terms appear in both solenoidal and dilatational part of the kinetic energy equations and are responsible for the transfer of energy between the two modes. In these situations where $M_t \approx 0\,(1)$, the acoustic oscillations corresponding to δ^2/M_t become the same order as the turbulent time scale and thus acoustic oscillations are present at all scales.

Even at extreme compressibility conditions such as high δ and M_t [62, 141] as high as 1.1, the solenoidal part of the flow field statistics seem to be largely invariant. In this mode, through the cross advection term, A_{c4}, the dilatational mode is largely driven by solenoidal motions. Thus analogous to a passive scalar in an incompressible turbulent medium, we can assume the dilatational mode to be a “passive vector" in the solenoidal flow field. Eq. 6.13a seems to represent a balance between the advection term consisting of one solenoidal mode and two dilatational mode and the dilatational viscous term. This equation interestingly is very similar to the “4/3 law" of passive scalars at sufficiently high Reynolds and Peclet numbers where the scalar variance is driven by the solenoidal flow field balanced by scalar dissipation.

Thus we use the Obukhov-Corrsin normalization of passive scalars for the dilatational energy spectra in this regime. Thus we normalize the dilatational energy spectra as $E_d \langle \epsilon_d \rangle^{-1} \langle \epsilon_s \rangle^{1/3} k^{5/3}$

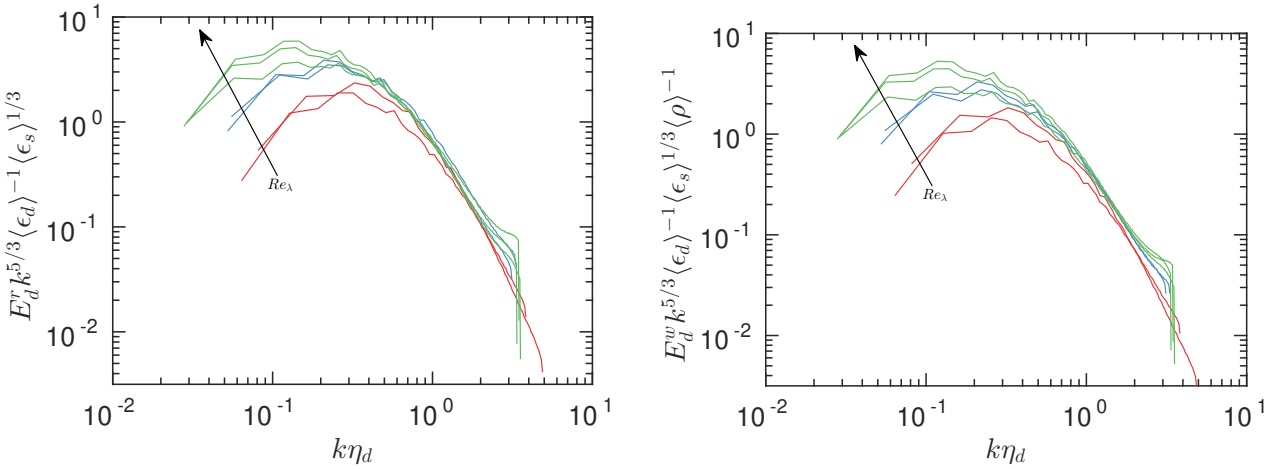

Figure 6.10: Dilatational spectra in the full developed solenoidal driven cascade regime; (δ, M_t) : $[\delta M_t > 0.1, \delta < 0.3]$; Reynolds averaged spectra (a) Kida averaged spectra (b).

with $\langle \epsilon_d \rangle$ and $\langle \epsilon_s \rangle$ playing role of scalar and turbulent dissipations respectively. Once again, the wavenumber is normalized by dilatational Kolmogorov length scale, $\eta_d = (\langle \mu \rangle^3 / \langle \epsilon_d \rangle)^{1/4}$. The compensated spectra in this regime is denoted as "D" in Fig. 6.6 (a) in the $\delta - M_t$ phase plane and are plotted in Figs. 6.10. Once again, the differences between the two averages are negligible. We indeed see that satisfactory collapse with universal behavior at small scales and the scale separation increases with R_λ similar to incompressible turbulence. Thus we conclude that in this regime, we expect an independent cascade for the dilatational field driven by the solenoidal flow field. We compare the dilatational spectra with passive scalar spectrum in incompressible turbulence later in the chapter.

6.5.3 Acoustic Cascade / Wave Steepening Regime

Now we consider the situations where the pure dilatational advection term dominates over the other advection terms. Thus we analyze the next order in δ and thus $\delta > 1$ and $M_t < 1.0$. The relevant equations from Eq. 3.18a to Eq. 3.18g are

$$O\left(\frac{\delta^2}{M_t}\right) : \left\langle w_i^d \frac{\partial w_i^d}{\partial \tau'} \right\rangle = \left\langle - \widehat{w}_i^d \left\{ \frac{1}{\sqrt{\rho}} \widehat{\frac{\partial p^d}{\partial \eta_i}} \right\}^d \right\rangle_k \tag{6.14a}$$

$$O\left(\delta^3\right) : \left\langle \widehat{w}_i^d \left\{ v_j^d \widehat{\frac{\partial w_i^d}{\partial \eta_j}} + w_i^d \widehat{\frac{\partial v_j^d}{\partial \eta_j}} \right\}^d \right\rangle_k = \left\langle -\widehat{w}_i^d \left\{ \frac{1}{\sqrt{\rho}} \widehat{\frac{\partial p^d}{\partial \xi_i}} \right\}^d \right\rangle_k \tag{6.14b}$$

$$O\left(\delta^3 M_t\right) : \left\langle \widehat{w}_i^d \left\{ v_j^d \widehat{\frac{\partial w_i^d}{\partial \xi_j}} + w_i^d \widehat{\frac{\partial v_j^d}{\partial \xi_j}} \right\}^d \right\rangle_k = 0. \tag{6.14c}$$

We see from these equations that in these high dilatational dominated regimes, the cascade if any will be driven by acoustic processes independent of the solenoidal motions. It is clear that Eq. 6.14a alone cannot support a cascade in the acoustic time scale since a mechanism to transfer energy from large to small scales is absent. Erlebacher *et al.* [43] derived the conditions when shocks can be formed in terms of initial flow conditions, specifically χ_0, the distribution of initial dilatational to total kinetic energy. They argued that shocklets or shock waves can form only when the advection terms have the same order of magnitude as that of time period of acoustic oscillations. In their analysis, they did not split the advection terms. It is possible that all advection terms can take part in the acoustic time scale cascade. A_{c3} cannot support cascade since it is confined to high wavenumbers. A_{c4} has an order of magnitude appearing in both solenoidal and dilatational kinetic energy budgets equations and thus the most probable advection term that can interact with acoustic time scale can be assumed to be the pure dilatational advection term, A_d. From the asymptotic analysis, the order of magnitude for A_d are $O\left(\delta^3 M_t\right)$ and $O\left(\delta^3\right)$ for large and small wavelength respectively. Thus we propose that acoustic cascade occurs when the dilatational advection is the same order of magnitude as that of acoustic time scale and thus the criterion can be written as

$$O\left(\delta^3\right) \approx O\left(\frac{\delta^2}{M_t}\right) \implies \delta M_t \approx O\left(1\right) \tag{6.15}$$

Although there are two orders of magnitude for A_d, we have chosen the $O\left(\delta^3\right)$ which corresponds to high wavenumber over $O\left(\delta^3 M_t\right)$. The choice can be justified as follows: for both $O\left(\delta^2/M_t\right)$ and $\left(\delta^3\right)$ in Eq. 6.14a and Eq. 6.14b respectively, there exists the pressure term that can possibly connect the two terms. Secondly, we can use simple scaling arguments to justify the $O\left(\delta^3\right)$ for A_d. When $M_t \approx 0\left(1\right)$, the order of magnitudes, $O\left(\delta^3 M_t\right)$ and $O\left(\delta^3\right)$ are sim-

ilar and thus does not make a difference. For cases with $M_t \ll 1.0$, the acoustic time scale, $O(\delta^2/M_t) \approx O(\delta^3)$ whereas $O(\delta^2 M_t)$ becomes $O(\delta^2)$. In our study where all cases are $M_t < 1.0$, it is highly probable for the acoustic time scale to be in the same order of magnitude as that of the advection term corresponding to high wavenumbers as seen in Eq. 6.15 whereas $O(\delta^2 M_t)$ becomes $O(\delta^2)$. In our study where all cases are $M_t < 1.0$, it is highly probable for the acoustic time scale to be in the same order of magnitude as that of the advection term corresponding to high wavenumbers as seen in Eq. 6.15.

We show that acoustic cascade or wave steepening may not be possible at high δ and $M_t \gg 1.0$. At such conditions, the order of magnitude of the acoustic time scale, $O(\delta^2/M_t)$ becomes $O(\delta)$ which is less than $O(\delta^3 M_t)$ or $O(\delta^3)$. It is clear that under these conditions, the interaction between advection and acoustic oscillations are weakened. Interestingly, at such situations, the order of magnitude of advection term A_{C4}, $O(\delta^2 M_t)$ (responsible for the solenoidal driven cascade), becomes $O(\delta^3)$, similar to that of pure dilatational advection, A_d at high wavenumbers. Ironically, at high compressibility (both high M_t and δ), a probable cascade, if it can exist, is the solenoidal driven one. We should remember that these conditions may not be physically realizable since we have shown that at high dilatational forced cases, δ decreases with M_t. This reinforces that M_t in general is not a measure of strength of compressibility but is a parameter that strengthens the interaction between the solenoidal and dilatational mode.

This regime is shown as "E" in Fig. 6.6 (a). This regime corresponds to the phase plane where $\delta > 1.0$ and $\delta M_t \approx O(1)$ or $0.15 < \delta M_t < 5.0$. We plot the spectra of dilatational spectra in this regime in Figs. 6.11. In the first picture, we normalize the spectra according to K41 theory using dilatational Kolmogorov variables. We see that spectra do not collapse and the slope of the normalized spectra is close to $k^{0.-433}$ which implies that in this regime, the slope of the spectra is close to $k^{-2.1} \approx k^{-2}$ observed in Burger's turbulence. Previous simulations of compressible turbulence have also reported k^{-2} scaling. Wang [147] observed k^{-2} scaling when $\delta M_t \approx 0.63 \approx O(1)$ ($\delta = 0.866$ and $M_t = 0.73$). Wang *et al* [144] also reported k^{-2} scaling when δM_t ranged from 0.2 to 0.455 ($\delta = 0.64 - 0.69$ and $M_t = 0.2 - 0.65$) . In both cases, $\delta M_t \approx O(1)$ which

agrees with our criterion for wave steepening. But these examples show that wave steepening can occur even for $\delta < 1.0$ and thus acoustic cascade regime needs to be modified.

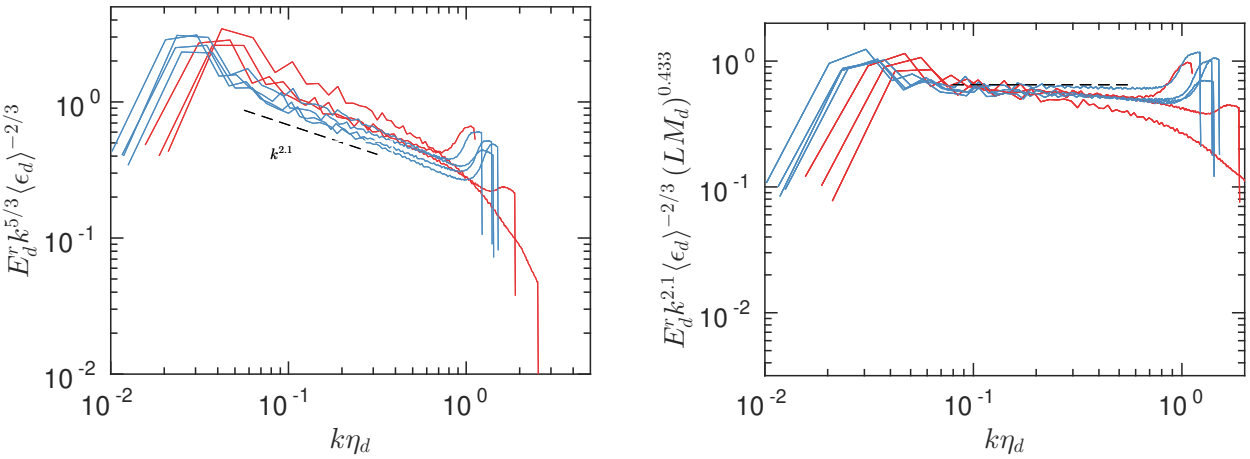

Figure 6.11: Dilatational energy spectra at wave steepening regime; $\delta M_t \approx O(1)$ and $\delta > 1.0$; Kolmogorov normalization (a) new normalization (b) dashed line in (a) correspond to power law of $k^{2.1}$ and in (b), a constant line.

This cascade occurs in the time scale of acoustic oscillations which is responsible for the exchange of energy between dilatational kinetic and potential energy. In this regime, we can expect that apart from the Kolmogorov variables, the spectra should also depend on dilatational velocity and time period of oscillation, $\tau = L/\langle c \rangle$. Here “L" and “$\langle c \rangle$" are the integral length scale and speed of sound respectively. Thus we write

$$E_d = F\left(\langle \epsilon_d \rangle, k, u_d, \tau\right). \tag{6.16a}$$

Using dimensional analysis, we can write the above equation as

$$E_d \approx k^{-5/3} \langle \epsilon_d \rangle^{2/3} \Pi\left(\tau u_d k\right) \tag{6.16b}$$

which we rearrange as

$$E_d \approx k^{-5/3} \langle \epsilon_d \rangle^{2/3} \Pi \left(\frac{u_d}{\langle c \rangle} kL \right) \tag{6.16c}$$

The expression, $u_d'/\langle c \rangle = M_d$ is the Mach number based on dilatational velocity and if we assume a power law for Π for simplicity and the power law exponent to be -0.433 so as to get $k^{-2.1}$ scaling. We get

$$E_d \approx k^{-2.1} \langle \epsilon_d \rangle^{2/3} \left(L M_d \right)^{-0.433} \tag{6.16d}$$

When the dilatational spectra in this regime are normalized according to the above equation as in Fig.6.11, the spectra approaches a plateau of constant around 0.65 at high R_λ and δM_t.

6.5.4 Solenoidally Driven Cascade vs Acoustic Cascade

So far, we have excluded the regime, $0.3 < \delta < 1.0$ where we can expect both advection terms to be equally dominant and therefore, both Kolmogorov and acoustic cascade can occur simultaneously. Therefore we compare the relative strength of the advection terms, A_{c4} and A_d responsible for solenoidal driven and acoustic cascade:

$$\frac{\delta^3}{\delta^2 M_t} = \frac{\delta}{M_t}. \tag{6.17a}$$

We expect dilatational advection to dominate when

$$\frac{\delta}{M_t} > 1.0 \tag{6.17b}$$

We saw wave steepening occurs when $\delta M_t > 0.15$ which implies $\delta M_t \approx O\left(1\right)$ where we also expect to see the fully developed Kolmogorov cascade regime. We propose to demarcate the solenoidal driven and acoustic cascade regime on the $\delta - M_t$ phase plane based on the relative strength of the advection terms. Thus wave steepening will dominate over the Kolmogorov cascade when both $O\left(\delta M_t\right) \approx 1$ and $\delta / M_t > 1$. We modify the $\delta - M_t$ phase plane as follows: we expect

the solenoidal driven cascade to occur when:

$$(\delta, M_t) : \left[0.15 > \delta M_t > 0.09, \frac{\delta}{M_t} < 5.0\right] \text{ or } \left[\delta M_t > 0.15, \frac{\delta}{M_t} < 1.0\right] \tag{6.18a}$$

Both the conditions inside [] have to be satisfied. In the same way, acoustic cascade regime is modified as

$$(\delta, M_t) : \left[0.15 < \delta M_t < 5, \frac{\delta}{M_t} > 1.0\right] \text{ or } \left[0.1 < \delta M_t < 0.15, \frac{\delta}{M_t} > 5.0\right] \tag{6.18b}$$

These regimes are marked as “D" and “E" corresponding to solenoidal driven cascade and acoustic cascade respectively in Fig. 6.6 (b). The cascade regimes–fully developed cascade regime and wave steepening– are also shown in Fig. 6.13 (a) and (b) respectively. We see two conditions in Eq. 6.18a and Eq. 6.18b. In the first condition– $0.15 < \delta M_t < 5.0$–the wave steepening mechanism is strong thus a milder dominance of A_d over A_{c4} $(\delta/M_t > 1.0)$ is only required. Whereas in the other condition–$0.1 < \delta M_t < 0.15$–the wave steepening mechanism may be relatively weak compared to solenoidal driven cascade when M_t is high at similar condition. Thus a stronger dominance of A_d over A_{C4} $(\delta/M_t > 5.0)$ is required for acoustic cascade to dominate over solenoidal driven cascade.

The Obukhov-Corrsin [26, 96] compensated dilatational energy spectra for all cases in the solenoidal driven cascade regime are shown in Fig. 6.12 (a). We observe satisfactory collapse of the dilatational energy spectra under this normalization. We also compare the spectra with solenoidal spectrum and the passive scalar spectrum in incompressible turbulence. Our results seem to be consistent with the “solenoidal passive vector" study [154]. The dilatational spectra are similar to passive scalars at high wavenumbers but is similar to solenoidal (incompressible) spectra at large scales. In Yang *et al.* [154], the compensated constant of the passive vector was approximately 0.99 in between the Obukhov-Corrsin and Kolmogorov constant for the passive scalars and velocities in incompressible turbulence respectively. In our case, Reynolds number is not high enough to evaluate the compensated constant for the dilatational spectra. Also, the bot-

tleneck is more pronounced for dilatational spectra indicative of high non-local spectral transfer [37]. Donzis and Sreenivasan [37] found that height of the spectral bump decrease with Reynolds number. The more pronounced spectral bump in the dilatational spectra might be due to the effective low Reynolds number in the dilatational part of the flow field. The similarities between the dilatational spectra and passive scalars are indeed interesting and thus the high intermittency observed in compressible turbulence at high M_t [139] probably might be a manifestation of the passive nature of the dilatational velocity field. The accumulated knowledge of passive scalars can act as guide to understand compressible turbulence at least in this regime.

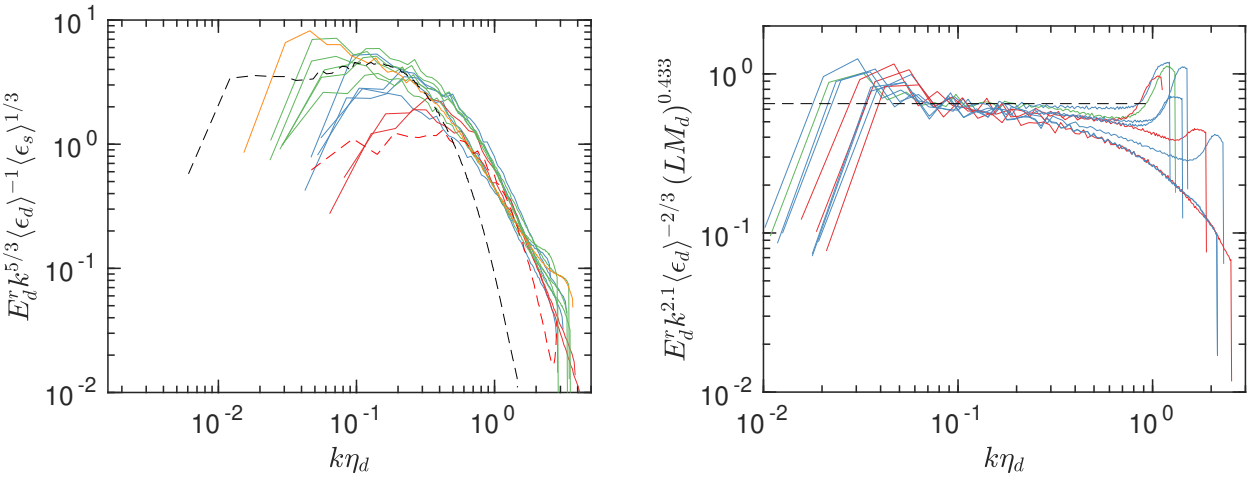

Figure 6.12: (a) Dilatational energy spectra at fully developed solenoidally driven cascade regime: $\left[0.15 < \delta M_t < 0.09, \frac{\delta}{M_t} < 5.0\right]$ or $\left[\delta M_t > 0.15, \frac{\delta}{M_t} < 1.0\right]$. The red and black dashed lines correspond to a passive scalar and solenoidal spectrum respectively. (b) Dilatational energy spectra at Wave steepening regime: $\left[0.15 < \delta M_t < 0.09, \frac{\delta}{M_t} > 5.0\right]$ or $\left[\delta M_t > 0.15, \frac{\delta}{M_t} > 1.0\right]$ (b).

In the wave steepening regime, along with our cases, we include the data from previous simulations [147, 144, 83] (see the region "E" of Fig. 6.6(b)) which have observed k^{-2} scaling. We find that they fit inside our criteria for wave steepening regime. The dilatational energy spectra for all our cases are given in Fig. 6.12 (b). From the figure, we observe that all cases approach a slope of $k^{-2.1}$ similar to Burgers turbulence at high R_λ and δM_t.

There can be transition between these two scaling regimes but more data are needed to validate if such a smooth transition is sudden or smooth. We stress that our analysis was based on a global order of magnitude analysis. The criteria we have proposed are based on the best available current simulation data. Furthermore, it is a possibility that two cascades can coexist in a single spectrum with multiple scaling regimes. In such a case, acoustic and solenoidal cascade may dominate in small and large scales respectively with a transition in between. The Reynolds number in our simulations is not high enough to investigate such a possibility.

The cascade regimes are depicted in Figs. 6.13 (a-b) below

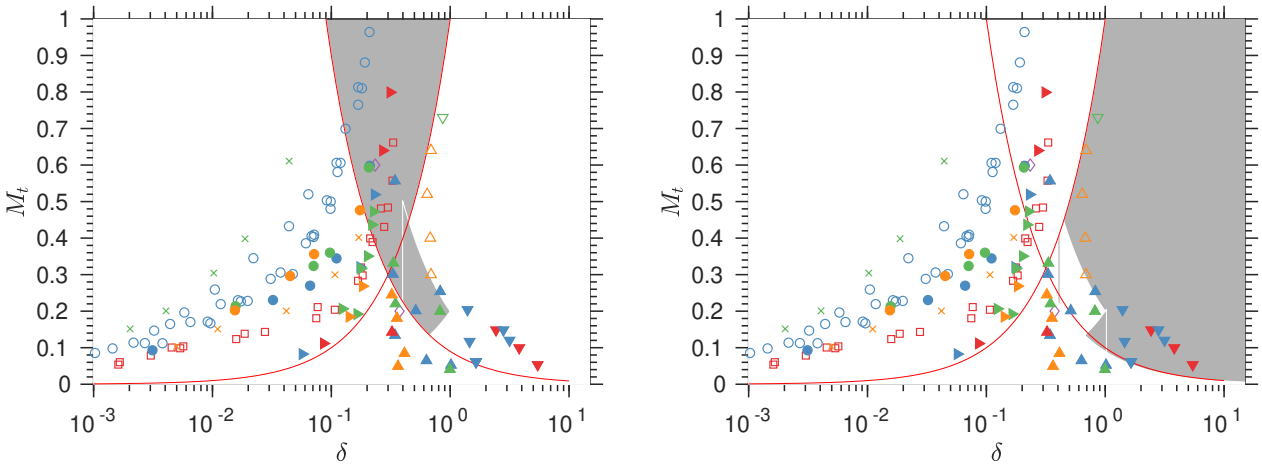

Figure 6.13: Cascade regimes in $\delta - M_t$ phase plane. (a) Fully developed solenoidal driven cascade and (b) Wave steepening.

6.6 Intermediate Cascade Regime

We call the transitional regime between the “non-cascade regimes" and “cascade regimes" as the intermediate cascade regime. This regime is depicted as “C" in both Figs. 6.6 (a-b) and also in Fig. 6.16 (a). The criterion for this regime in the $\delta - M_t$ phase plane as

$$(\delta, M_t) : [0.01 < \delta M_t < 0.1] \tag{6.19}$$

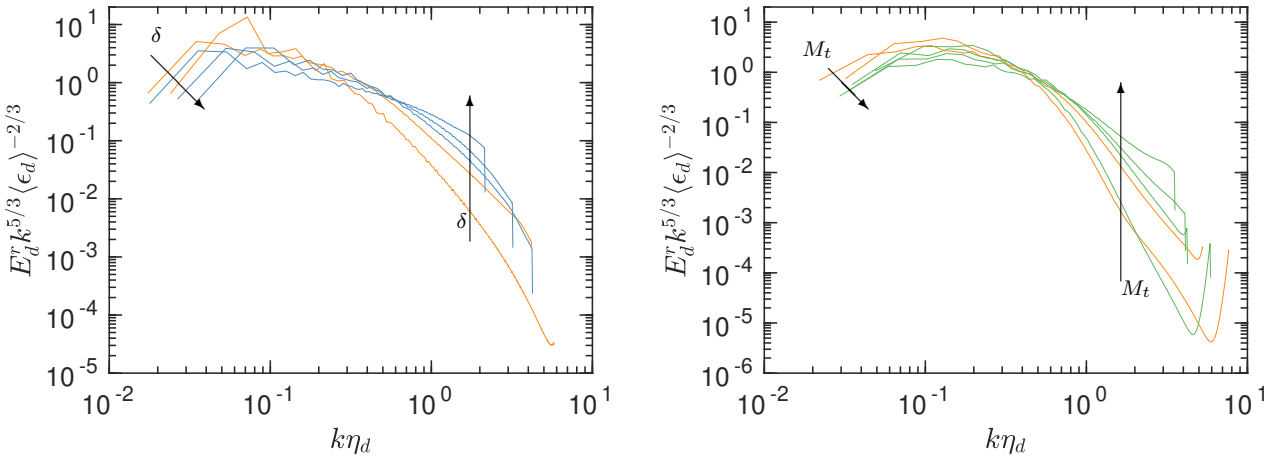

Figure 6.14: Dilatational spectra in transition regime from "non-cascade" regimes to "cascade" regimes, $0.01 < \delta M_t < 0.1$. $D > 0.5$, variation with δ at constant $M_t \approx 0.1$ (a) $D > 0.5$, variation with M_t with constant $\delta \approx 0.1$ (b).

In this intermediate region, we see the transition from pure oscillatory motion in acoustic time scale or pseudo sound to a solenoidal driven cascade or wave steepening regime. As δM_t increases, a cascade of energy happens from large to small scales compared to pure oscillatory motions confined at large scales at low δM_t. At low $\delta M_t < 0.01$, these acoustic motions or the pseudosound dominates over the cascade regimes, $\delta M_t > 0.1$. Thus in between $0.01 < \delta M_t < 0.1$, both these physical process can coexist. Thus the relative strength of these competing mechanisms would determine the scaling of the dilatational spectra at inertial ranges.

The K41 normalized Reynolds averaged dilatational energy spectra for these regime are plotted in Figs. 6.14. We plot the spectra at constant $M_t = 0.1$ in the first figure. In this figure, we see the transition from pure acoustic oscillations to wave steepening since $D > 0.5$ in all cases. As we increase δ or compressibility, there is transfer of energy from lower wavenumbers to higher wavenumbers since we see high energy content at high wavenumbers for high δ compared to that of low δ. Furthermore, we see the spectra approach the Burgers' k^{-2} scaling as we increase δ. In Fig. 6.14 (b), we plot the dilatational energy spectra for constant $\delta \approx 0.1$ but with increasing M_t, again for cases with $D > 0.5$. Similar to Fig.6.14 (a), as we increase M_t, there is more energy

at high wavenumbers indicating the development of a cascade. The spectra approach the fully developed solenoidal driven cascade spectrum, at high M_t.

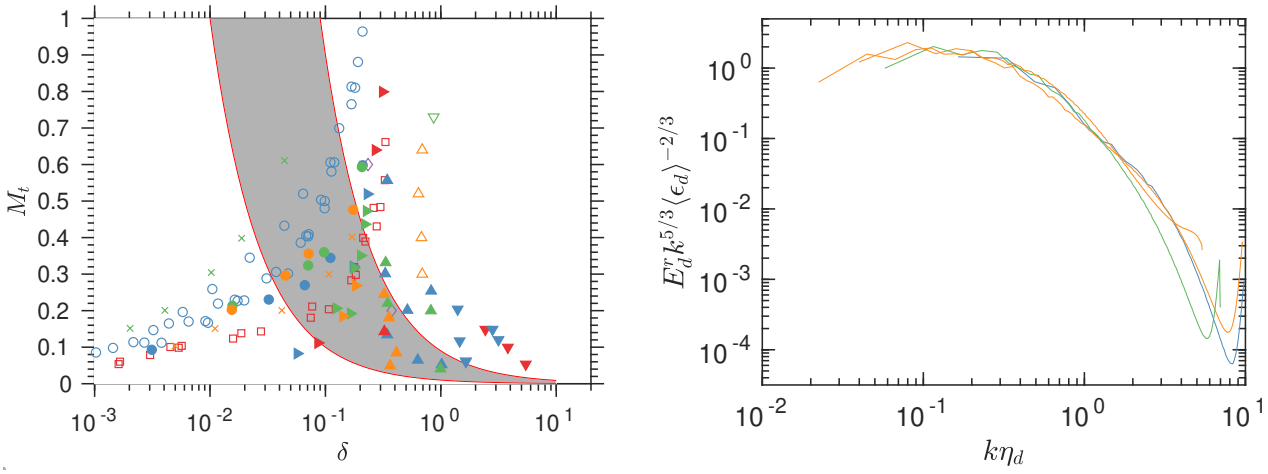

Figure 6.15: (a) Transition regime from non-cascade to cascade in the $\delta - M_t$ phase plane. (b) Dilatational spectra in transition regime from "non-cascade" regimes to "cascade" regimes, $0.01 < \delta M_t < 0.1$ and $D < 0.5$.

One can infer from the two plots in Fig. 6.14 that the effects of δ and M_t on the dilatational energy spectra are completely different. When δ increases, the spectra asymptote to a state where there is negligible interaction between the vortical and compressible modes, in contrast, at high M_t, the spectra approach a state where there is strong interaction between the modes. Thus it is evident that δ and M_t have to be considered as independent parameters.

Finally in Fig. 6.16 (b), we depict the dilatational energy spectra for cases with $D < 0.5$ where pseudosound phenomena are dominant. We cannot observe a clear transition for these particular cases compared to Figs .6.14. The obvious reason for this is that even at low δM_t for the pseudosound regime, there is energy at high wavenumbers even in the absence of a cascade process.

6.7 Summary

We summarize the main ideas and findings below:

- We showed that the order of magnitudes derived from the asymptotic analysis developed in Chap. 3 agrees with the DNS data.
- Based on the dominant term analysis, we divide the $\delta - M_t$ phase into distinct physical regimes where we can observe distinct compressible behaviours
- The compressible regimes are divided as follows:

    1. Non-cascade regime $(\delta M_t < 0.01)$
        - Pseudosound regime: we derived the conditions for pseudosound regime and verified with spectra in this regime agrees with pseudosound scaling. Moreover past studies that reported pseudosound scaling agrees with our criteria.
        - Weak equipartition: we derived the conditions for weak equipartition that corresponds to acoustic oscillations.
    2. Cascade regime $(\delta M_t > 0.1)$
        - Solenoidally driven cascade regime: The conditions for this regime were derived. Moreover new compensation for the dilatational energy spectra is proposed. The new normalization is similar to the Obukhov-Corrsin scaling for passive scalars in incompressible turbulence. The spectra showed excellent collapse under the new normalization.
        - Wave steepening regime: The conditions for this regime was derived based on the argument that magnitude of time scales of acoustic oscillations must be comparable to that of pure dilatational advection. The spectra in this regime showed a k^{-2} scaling similar to that Burgers' turbulence.
    3. Intermediate regime $(0.01 < \delta M_t < 0.1)$: Demonstrated the transition from non-cascade regimes to cascade regimes. Highlighted the distinct effect of δ and M_t on the evolution of the dilatational spectra.

The final $\delta - M_t$ phase along with the regimes are reproduced below in Fig. 6.16

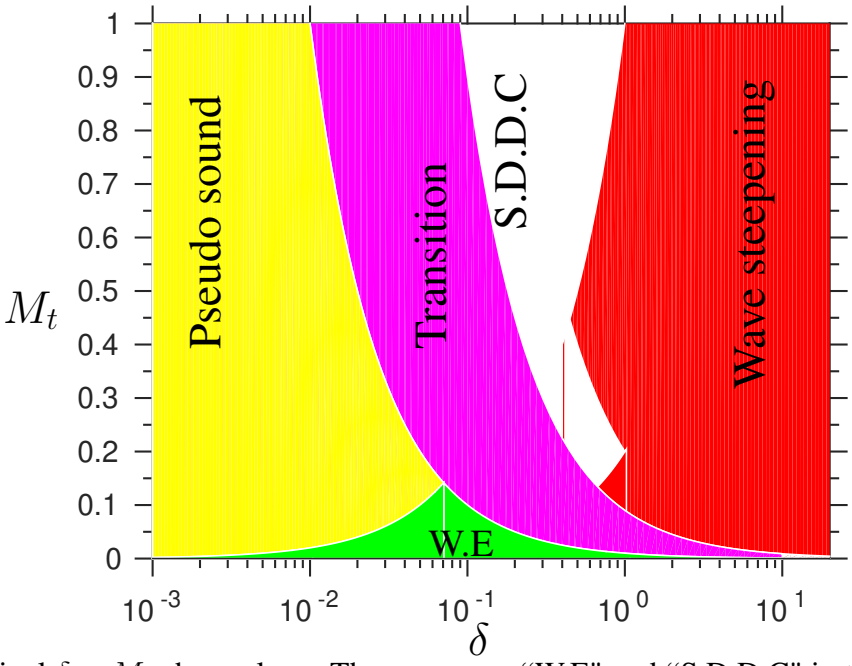

Figure 6.16: Final $\delta - M_t$ phase plane. The acronyms “W.E" and “S.D.D.C" in the figure correspond to weak equipartition and solenoidal driven dilatational cascade respectively.

7. MIXING IN COMPRESSIBLE TURBULENCE

7.1 Introduction

One of the defining features of turbulence is its ability to mix substances with great efficiency of the order of magnitudes greater than molecular mixing. A vast amount of literature exist for this subject when the fluid is incompressible [125]. In its own right, it is a fundamentally important problem and a great paradigm for many practical circumstances. However compared to incompressible turbulence, the results of mixing in compressible turbulence is very sparse. Thus, in this chapter, we extend our analysis to understand the effects of compressibility and implications of our results in the previous chapters, on mixing.

An important application of high-speed mixing is in supersonic combustion encountered in air breathing propulsion systems such as scram jets used for hypersonic flights. Mixing at these extreme conditions is challenging since the residence time required for combustion is low. In most designs, to ensure sufficient residence time for combustion to occur, turbulence is generated through shear layers [90] or from the wake created from an obstacle [138] such that cascade mechanism will result in molecular mixing of species for combustion to occur. At least in canonical settings of supersonic combustion, the mixing controlled combustion regimes corresponding to large Damköhler number, $Da = t_d/t_{ch} \to \infty$ dominate the flow field. It is usually assumed that the most dominant mode of combustion in supersonic conditions is the non-premixed one although the premixed mode plays an important role in flame stabilization near the walls and recirculation zones [133].

In non-premixed flames, combustion occurs concomitantly with mixing since the fuel and oxidant are initially separated. For many practical low speed combustion systems such as gas turbines and diesel engines, they act as a model problem. Passive scalar field plays a pivotal role in non-premixed combustion and its importance has been recognized for a long time [12]. This is epitomized in Pitsch and Steiner's [103] remark: "The rate of molecular scalar mixing is rep-

resented by the scalar dissipation rate which can be identified as the most important parameter in the description of non-premixed combustion". For the cases of fast chemistry where chemical reaction rates are much larger compared to the rates of molecular mixing, an equivalence relation between the mean reaction rate and the passive or conserved scalar dissipation rate (independent of chemical reactions) was derived by Bilger [12]. The scalar dissipation rate is considered as a major parameter even for finite-rate chemistry in many common combustion models such as flamelet model, transport probability density function model and conditional moment closure model. Thus combustion researchers are greatly interested in the characteristics of the mixing and have been the subject of many research studies, for example from early to recent studies [127, 125].

Compressibility effects on the dynamics of turbulence has to be taken into account for proper modeling of mixing in these high-speed propulsion systems. However, today's existing models do not explicitly account for compressibility effects. For example, compressibility effects on scalar dissipation are not considered in Bilger's relation. Studies of compressibility effects on scalar dissipation have been sparse and should be distinguished from the effects on the scalar field or turbulence in general by dilatational motions induced in the flow field as result of the heat release from combustion. In general, these combustion induced motions can modify the structure of turbulence and have been studied extensively in the literature for both non-premixed and premixed configurations. The theoretical analysis by Bilger [13] has shown that these combustion induced effects are prominent for the premixed mode of combustion compared to the non-premixed mode. For example, except for the diffusion sub-range of the temperature spectra, the combustion induced dilatational motions can be taken into account by rescaling the spectra such as energy and mixture fraction using Favre averages [68]. The premixed DNS combustion study [56] points that at low Karlovitz number –the ratio of chemical to Kolmogorov time scale– the heat release can have a very strong effect on the structure of turbulence and can thus modify the interaction between turbulence and the flame front or the reactive scalars.

One of the well known effect of compressibility on turbulence is the reduced growth rate of turbulence in mixing or shear layers [115, 137]. Similar global effect such as the inhibition of

growth rate was seen for reactive mixing layers irrespective of compressibility effects [87]. It should be emphasized that although the global effects are the same, the physical mechanisms responsible for the reduced growth rate are distinctly different for the reacting and inert cases. However, our understanding of the effects of compressibility on the cascade of scalar field and the small scale features such as intermittent dilatations, shocklets (which are absent in incompressible flow field) on the fine scale features of the scalar field are not clear. Compressible turbulence even in the absence of combustion is by itself a very complex phenomenon. on The study by Ni [95] has shown that mixing efficiency cannot be characterized by M_t alone but rather it heavily depends on the nature of forcing too. We have seen in Chap. 4 that even for a fixed M_t, the characteristics of the flow field depend on the details on forcing. Further progress have been made recently in Ref. [35] and as seen in Chap. 4 that by adding an additional parameter, δ into the governing parameters, one can discover some aspects of universality in compressible turbulence. In order to characterize mixing, one also needs an additional parameter, Schmidt number, $S = \mu/\left[\langle\rho\rangle D\right]$ where D is the diffusivity of the scalar field. Thus, Schmidt number is the ratio of strength of the momentum to scalar diffusivity. For the current study, we analyze the DNS data where $S = 1.0$ for a wide range of compressibility conditions.

7.2 Failure of Classical Scaling

We saw the inadequacy of the incompressible scaling for the dilatational energy spectra in Chap. 6 compensated according to Ref [70]. In fact we also showed in our recent work [62] (see Chap. 6) that even the solenoidal spectra do not collapse under the classical incompressible scaling. However a robust collapse can be achieved if we include only the solenoidal contributions to the total dissipation and use a solenoidal Kolmogorov length scale based on solenoidal dissipation alone.

The behaviour of scalars in incompressible turbulence is reasonably well known at least at the phenomenological level [9, 26, 75, 123, 125, 155]. For Schmidt number of unity, the Obukhov-Corrsin scaling, $E_\phi(k) = C_{oc}\langle\epsilon_\phi\rangle\langle\epsilon\rangle^{-1/3}k^{-5/3}$ is the appropriate normalization for the passive scalars. In the Obukhov-Corrsin scaling definition, E_ϕ is defined such that $\int_0^\infty E_\phi(k)\,dk = \langle\phi^2\rangle/2$

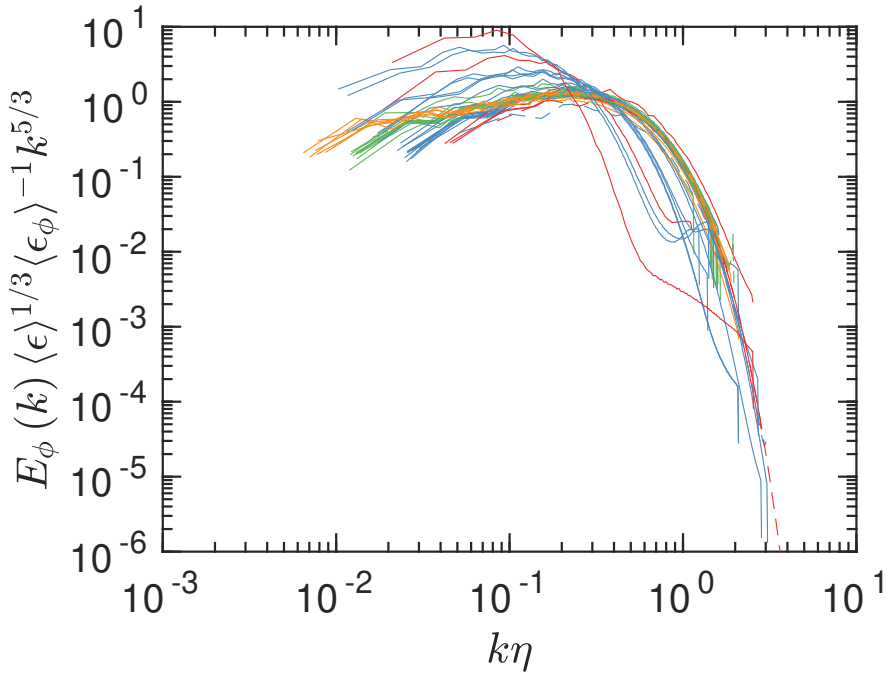

Figure 7.1: The Obukhov-Corrsin compensated scalar spectra using total dissipation and Kolmogorov length scale based on the total energy dissipation. No scaling is observed. Dashed line is for the incompressible case. In this figure and rest of the figures in this chapter unless otherwise stated, colors correspond to R_λ: $R_\lambda < 40$, $40 < R_\lambda < 70$, $70 < R_\lambda < 115$, $115 < R_\lambda < 180$.

and $\langle\epsilon_\phi\rangle$ is the mean scalar dissipation and C_{oc} is the Obukhov-Corrsin constant. We see in Fig. 7.3 that there is no collapse of data which indicates that incompressible scaling fails for the compensated scalar spectra. It does seem that compressibility have a first order effect on the passive scalar spectra.

The spectrum reveals the behaviour of the scalar at the large and inertial scales. The interaction of the scalars with the velocity field at small scales can be understood by analyzing the alignment of the scalar gradient with the directions of eigenvectors of the strain field. In incompressible turbulence, the stirring action of the turbulent velocity plays a major role in bringing iso-surfaces of the scalars close together [29, 125, 149]. This stirring action facilitates the mixing process by creating high scalar gradient across the scalar field ultimately enabling the molecular diffusion to act. Batchelor [9] proposed for Schmidt numbers greater that unity that the scalar gradient gets itself aligned with the direction corresponding to the most compressive eigenvalue. Perhaps

surprisingly, DNS studies [39, 136] tend to show that even for Schmidt number of unity, this aspect of the theory remains valid. For decaying compressible turbulence, Danish *et al.* [27], for a narrow range of initial $M_t\,(0.50-0.70)$ and $R_\lambda\,(18-24)$ found that the topology and alignment were universal. The data in our study cover a wider ranger of compressible turbulent states in M_t, R_λ and δ.

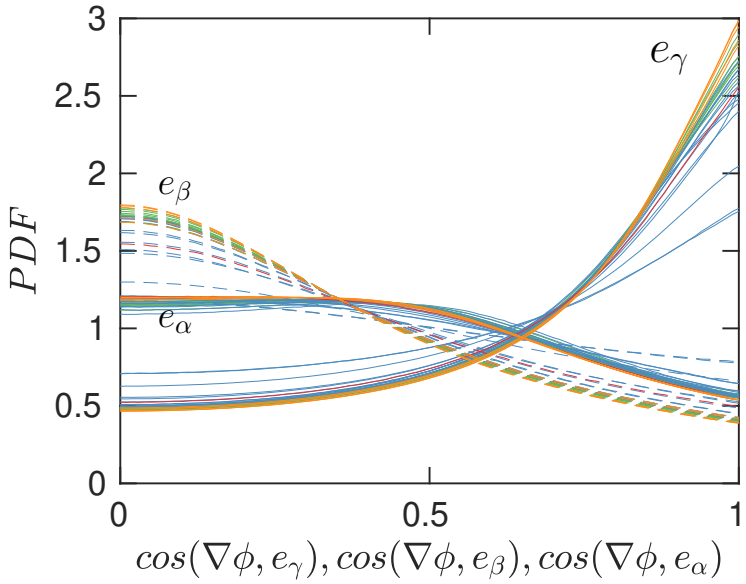

Figure 7.2: Alignment of scalar gradient $(\nabla\phi)$ with the eigen-directions of the S_{ij}, i.e. $e_\gamma, e_\beta, e_\alpha$ which correspond to the eigenvalues (γ, β, α) with $\gamma < \beta < \alpha$.

Fig. 7.2 depicts the alignment of scalar gradient, $\nabla\phi = \partial\phi/\partial x_i$, with the eigendirections of the symmetric velocity gradient, S_{ij}, where

$$S_{ij} = \frac{1}{2}\left(\frac{\partial u_i}{\partial x_j} + \frac{\partial u_j}{\partial x_i}\right).$$

In the figure, e_α, e_β and e_γ are the eigenvectors of S_{ij} corresponding to the maximum, intermediate and minimum eigenvalues $(\alpha > \beta > \gamma)$ respectively. For incompressible turbulence, $\alpha + \beta + \gamma = 0$ due to the constraint $\nabla \cdot \mathbf{u} = 0$. For a very narrow range of compressibility

conditions, studies by Blaisdell *et al.* [15] and more recently Ni [95] showed that the contributions from the dilatational field to the scalar flux are negligible. Indeed one sees from the figure that, the Batchelor theorem and the behaviour of passive scalars at small scales are not universal in compressible turbulence.

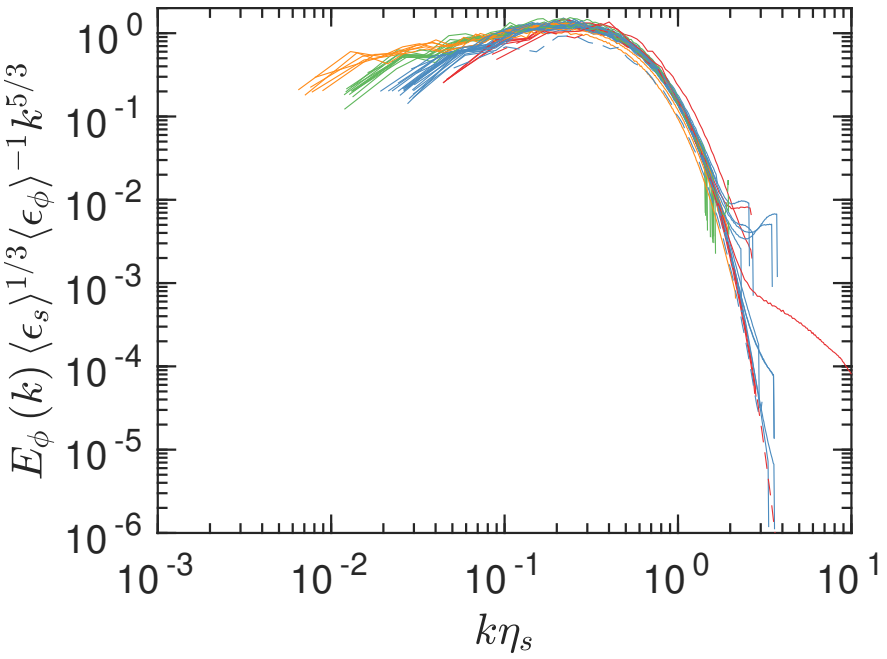

Figure 7.3: The Obukhov-Corrsin compensated scalar spectra using solenoidal dissipation $\langle\epsilon_s\rangle$ and solenoidal Kolmogorov length scale based on the solenoidal energy dissipation. Excellent collapse is observed. Dashed line is for the incompressible case.

7.3 Rescaling with the Solenoidal Variables

We have seen the collapse of the solenoidal spectra when the normalization is rescaled with just the solenoidal variables. Although for a very narrow range of compressibility conditions, there are studies [15, 95] which showed that contributions to scalar flux from the dilatational part of the velocity field are negligible. We had seen in the previous section that solenoidal energy spectra collapsed under K41 normalization when we used just the solenoidal variables, η_s and $\langle\epsilon_s\rangle$.

Therefore in Fig. 7.3, similar to the solenoidal spectra, we plot the Obukhov-Corrsin compensated scalar spectra using just the solenoidal flow field. We observe a remarkably robust collapse for the scalar spectra for a wide range of compressibility conditions in terms of parameters δ and M_t. The spectra looks similar to the incompressible scalar spectra which hints that the interaction between the scalar and solenoidal field is universal despite the fact flow field is dominated by high levels of dilatational motions. A possible explanation for this collapse is that the large scale motions of the scalar and its cascade to smaller scales are driven mainly by the vortical (solenoidal) motions in the flow field, and thus is independent of compressibility or dilatational motions. Thus when the classical scaling laws are applied after rescaling with solenoidal variables even for highly dilatational flow content due to compressibility effects, the incompressible models can be successfully applied.

It can be concluded from the discussions so far that the large and inertial range scales of the scalar field are driven by the solenoidal field. But the small scale motions of scalar field can be affected by compressibility. Therefore we assess the effects of compressibility on the small scale motions of the solenoidal flow field which can have a direct effect on the scalar field. Thus we analyze the symmetric solenoidal velocity gradient,

$$S_{ij}^s = \frac{1}{2}\left(\frac{\partial u_i^s}{\partial x_j} + \frac{\partial u_j^s}{\partial x_i}\right). \tag{7.1}$$

We examine the statistics of the normalized eigenvalues, (β_s) [136] given as $\hat{\beta}_s = \sqrt{6}\beta_s/\sqrt{\alpha_s^2 + \beta_s^2 + \gamma_s^2}$, such that $-1 < \hat{\beta}_s < 1$ is bounded.

The probability density function (PDF) of the normalized eigenvalue, $\left(\hat{\beta}_s\right)$ is plotted in Fig. 7.4 for a wide range of compressibility conditions. One observes excellent collapse for curve (i) which indicates that the ratio of solenoidal eigenvalues is not affected by compressibility. For curve (ii), the ratio β_s/γ_s in the same figure, we observe similar universal behaviour. It should also be noted that the maximum probable value of β_s/γ_s is approximately 0.28 corresponding to the ratio $\gamma_s/\beta_s = 3.7$ close to the value for incompressible turbulence [4] and consistent with results obtained by solenoidal forcing. This implicitly suggests that, although compressibility may change

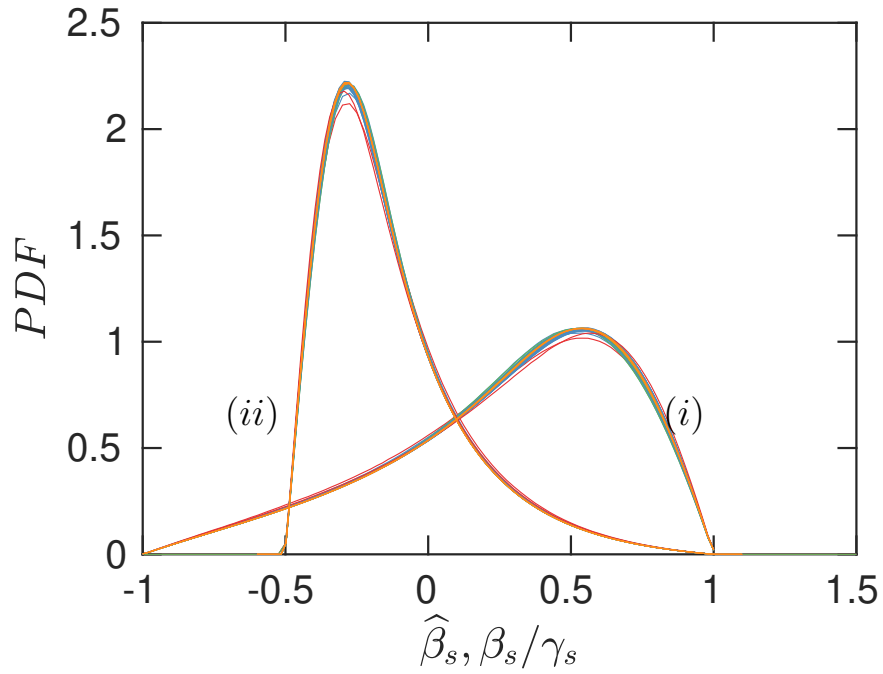

Figure 7.4: Normalized eigenvalues of the solenoidal symmetric velocity gradient tensor S^s_{ij}: (i) $\hat{\beta}_s = \sqrt{6}\beta_s/\sqrt{\alpha_s^2 + \beta_s^s + \gamma_s^2}$; (ii) β_s/γ_s.

the solenoidal field itself, it does not alter its mixing capability and would remain as efficient as incompressible turbulence.

The alignment of scalar gradient with the solenoidal frame of reference is plotted in Fig. 7.5 (a). Similar to the incompressible case [136], the scalar gradient is aligned with the direction corresponding to the most compressive eigenvalue of the symmetric solenoidal velocity gradient tensor. Compared to the larger DNS database and wider range of conditions considered in this study, similar behaviour was reported by Foysi *et al.* [50] for $R_\lambda \approx 50$ and M_t in between $0.05 - 0.63$ for solenoidally forced simulations. We do observe some weak compressibility effects at small scales. To illustrate this and understand the behaviour qualitatively, we plot in Fig. 7.5 (b), the PDF values for $cos\left(\nabla\phi, e^s_\gamma\right) \in [0.995, 1]$– that is when the two vectors are perfectly aligned– as a function of the turbulent Mach number, M_t. We can observe from the figure that the major effects are due to R_λ although there is a weak compressibility effect where the alignment decreases with

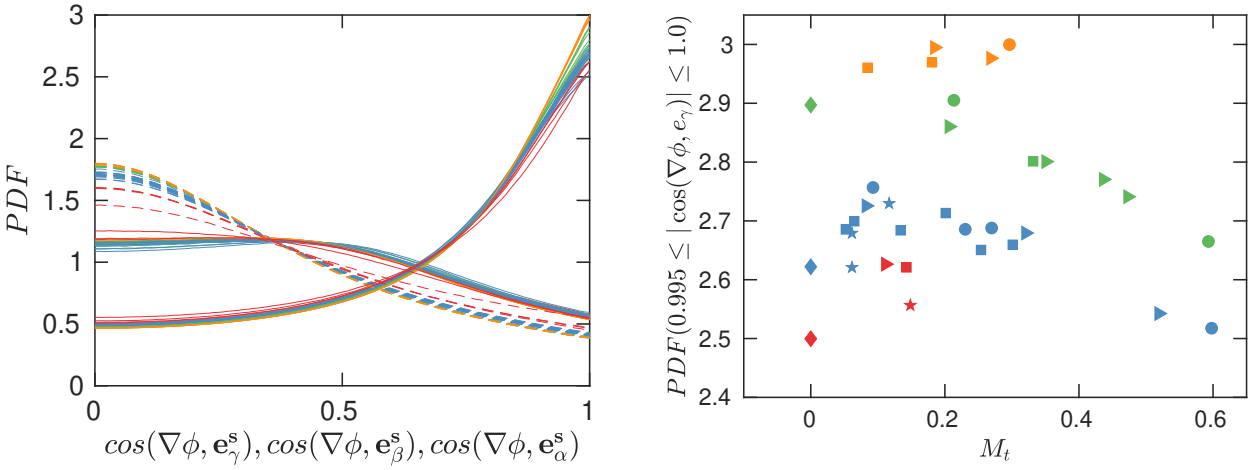

Figure 7.5: (a) Alignment of scalar gradient $(\nabla\phi)$ with e^s_α, e^s_β and e^s_γ, the eigenvectors of S^s_{ij}. (b) Probability that the scalar gradient $(\nabla\phi)$ aligns perfectly with the eigendirection e^s_γ corresponding to the most compressive eigenvalue. In (b), the symbols correspond to % of dilatational forcing: circles: 0% dilatational forcing; triangles: $10 - 30\%$ dilatational forcing; squares: $30 - 60\%$ dilatational forcing; diamonds: $70 - 80$ % dilatational forcing; stars: $80 - 100$ % dilatational forcing.

M_t for $M_t > 0.1$. This implies that unlike the inertial range motions, the dissipative motions can be modestly affected by shocklets formed in compressible turbulence. Even at the most extreme dilatational conditions, the volume fraction of the flow field occupied by shocklets are small (less than 3 %) which probably might be the reason for the modest effect of compressibility. In addition to this, under theses circumstances, solenoidal Kolmogorov length scale is larger than that corresponding to pure solenoidal forcing. This results in a scale separation between the smallest scales of scalar motion and shocklets which might also contribute towards the weak interaction between scalar and dilatational flow field at small scales.

7.4 Alignment of Scalar Gradient with Dilatational Flow Field

The interaction of the scalar with dilatational flow field at small scales might help us to understand the trend in Fig. 7.5 (b). Thus similar to the solenoidal strain rate tensor, we can define the

dilatational strain-rate tensor, S^d_{ij} as

$$S^d_{ij} = \frac{1}{2}\left(\frac{\partial u^d_i}{\partial x_j} + \frac{\partial u^d_j}{\partial x_i}\right). \tag{7.2}$$

Unlike the solenoidal case, the trace of S^d_{ij} tensor is not zero. To distinguish the difference in behaviour, we divide the $\delta - M_t$ phase plane into four distinct regimes.

1. $M_t < 0.1$, low δ (completely solenoidal forcing)
2. $M_t < 0.1$, high δ (more than 50 % dilatational forcing)
3. $M_t > 0.1$, low δ (completely solenoidal forcing)
4. $M_t > 0.1$, high δ (more than 50 % dilatational forcing)

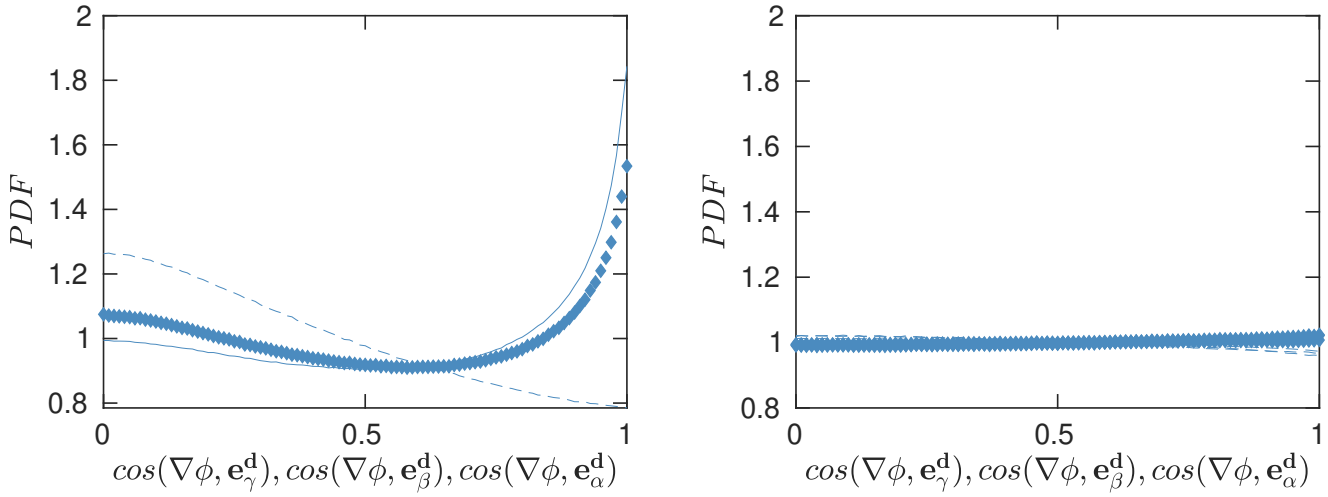

Figure 7.6: Fine scale structure of scalar dissipation using dilatational variables. Alignment of scalar gradient $(\nabla\phi)$ with the eigendirections of the symmetric part of the dilatational velocity gradient S^d_{ij} at $M_t < 0.1$ for (a) purely solenoidal forcing (low δ) and (b) more than 50% dilatational forcing. Here and in the figure to follow, 'diamonds', 'dashed lines' and 'solid lines correspond to most compressive $\left(\mathbf{e}^{\mathbf{d}}_\gamma\right)$, intermediate $\left(\mathbf{e}^{\mathbf{d}}_\beta\right)$ and most expansive directions $\left(\mathbf{e}^{\mathbf{d}}_\alpha\right)$, respectively.

The forcing conditions required to achieve the compressible turbulent state above is given in-

side the parentheses. The alignment of the scalar gradient with dilatational flow field for $M_t < 0.1$ is given in Figs. 7.6. From the first figure, for the purely solenoidal forced case, we see that there is equal propensity for the scalar gradient to get itself aligned with the most compressive and expansive direction. Whereas for the highly dilatational case shown in Fig. 7.6 (b), for all directions, we see a uniform probability. This suggests that at these compressibility conditions, there is no preferred direction for the alignment of the scalar gradient which means the fine scale structures of the scalar field are independent of compressibility. A possible explanation for this, is that at low M_t and δ achieved through pure solenoidal forcing, the system is in the pseudo-sound regime where most of the dilatational motions are active at high wavenumbers [140, 110] and thus the dilatational field can directly interfere with scalar field. In contrast, under dilatational forcing, we expect to have acoustic motions at low wavenumbers, and at low M_t, these acoustic motions are decoupled from the vortical motions. This incapacitates the dilatational motions from affecting the dynamics of the scalar field.

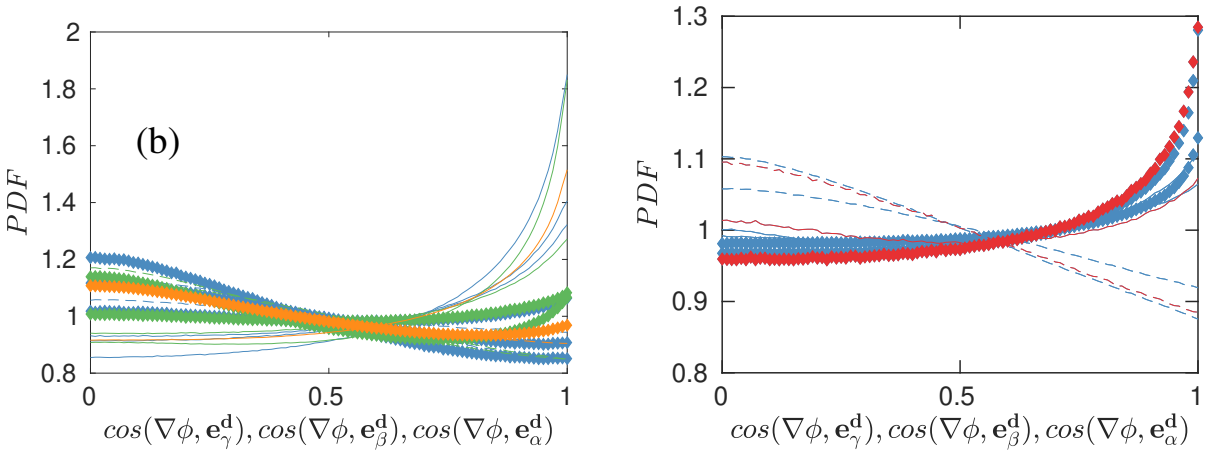

Figure 7.7: Fine scale structure of scalar dissipation for dilatationally-dominated conditions. The alignment of scalar gradient $(\nabla\phi)$ with eigendirections of the symmetric part of the dilatational velocity gradient tensor, S^d_{ij} at $M_t > 0.1$ for (a) purely solenoidal forcing (low δ) and (b) more than 50% dilatational forcing (high δ).

As M_t increases, we expect both solenoidal and dilatational modes to interact with each other

resulting in comparable time and length scales for both modes. As a consequence, the time scales of scalar motions are commensurate with those of both vortical and dilatational motions. Thus we can expect the dilatational motions to interact with the scalars directly, as a result, stronger compressibility effects on the scalar field. Indeed this is what we observe at high M_t in Figs .7.7. For the pure solenoidal forced cases, thus low δ in Fig .7.7 (a), we can see that the scalar gradient is aligned with the most expansive direction consistent with the results from Foysi *et al* [50]. In contrast, for the diltationally forced cases in Fig. 7.7 (b), it is more probable for the scalar gradient to get aligned with the compressive direction similar to incompressible turbulence. It is interesting to note that the alignment is weaker for the dilatational forced cases when compared to the solenoidally forced cases.

The DNS of premixed combustion conducted by Kolla *et al.* [69] has shown that for a reactive scalar, classic Kolmogorov scaling may not hold at diffusive-reactive range for Damköhler number spanning between 0.13 and 0.54. Numerical studies of premixed combustion [20, 56, 57, 67, 129] showed that the dilatational motions due to heat release cause the gradient of the reactive scalar or the progress variable to align with the most expansive direction of the strain rate tensor. For example, in the reaction zone of low turbulence intensities or Karlovitz number, the reactive scalar gradient aligns with the expansive direction[56]. As our results demonstrate, this behavior can be observed for even passive scalar solely due to compressibility effects in a non-reacting flow field. However the alignment of the scalar gradient with the most expansive direction is not universal in the dilatational frame when compared to the solenoidal frame, which is similar to that observed in incompressible turbulence.

To summarize, we have identified in terms of δ and M_t, the regimes where we can expect the scalar gradient to align with most expansive direction. This behavior observed in the above combustion studies may just correspond to some particular δ, M_t conditions but other generic behaviours are also possible. Finally, our work can act as a baseline to compare and isolate heat release effects by combustion from pure flow compressibility effects in the non-reacting cases.

7.5 Summary

The current work proposes new scaling laws for mixing in compressible turbulence and can have major impact in the modeling of passive scalars which are critical for many paradigms in turbulent combustion. We summarize below the main findings and ideas in this section.

- Classical scaling laws proposed for incompressible turbulence fail in compressible turbulence under general compressibility conditions. For example, the Obukhov-Corrsin normalization failed to collapse the spectra. Also we showed that the Batchelor theory for passive scalars is not universal.

- The scalar spectra can be collapsed when compensated with Obukhov-Corrsin scaling using just the solenoidal variables. This suggest that at large and inertial scales, the scalar field is oblivious to the presence of the dilatational motions but are mainly driven by the vortical modes similar to incompressible turbulence.

- Similarly we found that the Batchelor theory is universal in the solenoidal frame of reference: the scalar gradient gets aligned with the most compressive direction similar to incompressible turbulence. Reynolds number has a first order effect but there are secondary M_t (compressibility) effects on the fine-scale structures of scalars.

- In contrast to the solenoidal frame of reference, the Batchelor theory in the dilatational frame of reference is not universal. But the behaviour strongly depends on the values of δ and M_t.

8. CONCLUSIONS AND FUTURE WORK

8.1 Conclusions

Turbulence is a phenomenon on which despite having been studied for more than a century eludes a general theory that can explain and predict flow features, and ultimately provide venues for control in engineering devices. From a practical perspective, it is of paramount importance in many industrial sectors including automotive, aerospace, energy, medical to name a few. Mixing, one of the defining features of turbulence has a critical role in many natural processes that occur in both terrestrial and astrophysical ecosystems. In some of these, such as, flows in astrophysics and aerospace domains, compressibility effects on turbulence have to been taken into account to understand and model the flow realistically. Unfortunately, our fundamental understanding of these flows is inadequate compared to its incompressible counterpart. This work attempts to present a step in this direction and towards deeper contributions to the fundamental understanding of compressible turbulence and mixing.

The current effort is based on previous work done by Dr. Jagannathan which was mainly confined to solenoidally forced cases. Using the massively parallel cDNS code developed as part of Dr. Jagannathan's dissertation [59], a massive database of compressible homogeneous isotropic turbulence was created under a wide range of forcing conditions encompassing all the widest range of compressibility conditions for $M_t < 1$ in terms of the governing parameters, namely, M_t, δ and R_λ.

The need to push the Reynolds numbers close to those seen in engineering applications for DNS of turbulence is a grand computational challenge. As a result, some efforts were made to remove the bottlenecks that degrade the scalability of the code, in particular, optimization studies. A particular aspect that required special attention was the performance of I/O at very large scales. Furthermore, the first strides towards exploiting the massive computational power of GPUs were also made to further speed up the code.

The majority of the research in this dissertation was devoted to unravelling specific aspects associated with the physics of compressible turbulence and mixing. We briefly summarize the main conclusions from this study.

Incompressible turbulence as a scientific subject has been extensively studied for almost a century. A major breakthrough in the field was the statistical theories proposed by Kolmogorov popularly known as K41 and K62 theories [70, 71]. The main tenets of the theories were the self-similarity scaling and universality of the flows where the external conditions that sustain turbulence become irrelevant. This apparent simplification has spurred tremendous research becoming the backbone of fundamental research in turbulence even today. In terms of more applied research, these statistical theories are the base for the development of subgrid and turbulence models for LES and RANS respectively.

Unfortunately, compressible turbulence has been fraught and plagued with observations that led the community to believe in the non-existence of universality in general. This is in part due to the fact that the suggested intrinsic parameters, namely, the turbulent Mach number, M_t and Taylor Reynolds number, R_λ are unable to completely characterize the complicated physical behaviour manifested by the phenomenon even for the idealized case of homogeneous isotropic turbulence. Very often, to explain the characteristics, one has to supplement the intrinsic parameters with those that depend on external factors such as boundary conditions, mean flow and initial conditions. A well known examples are the gradient and convective Mach numbers for homogeneous shear flows and mixing layers respectively [52, 112]

We argue here that this gloomy state of affairs is due to the incomplete set of intrinsic parameter space used to describe the compressible turbulent system. We show that universal aspects of compressible turbulence can be discovered when we consider δ, the ratio of dilatational to solenoidal rms velocities as an intrinsic parameter in addition to the traditional parameters, M_t and R_λ using our own HIT simulation data with a wide of range of dilatational forcing conditions and the compiled data from the literature consisting of HIT, HST (which are anisotropic), thermally forced simulations and even fluids with different molecular properties.

These results highlight the importance of the dilatational motions in compressible turbulence. Using the scaling of pressure corresponding to solenoidal and equipartition pressure at two asymptotic limits of $\delta \to 0$ and $\delta \to \infty$ respectively and comparing their relative magnitude, we are able to derive the scaling law for the ratio of dilatational to solenoidal pressure. The scaling law is a complex combination of δ and M_t suggesting self-similarity of the second kind where the scaling laws cannot be derived by trivial non-dimensional analysis. We observe a robust collapse of data and sudden transition from solenoidal dominated pressure regime to weak equipartition regime at $D_{crit} = \delta\sqrt{\delta^2+1}/M_t = 0.5$. In the process, we derive the condition for weak equipartition proposed for low M_t. The criterion for equipartition also depends on δ, thus helping to resolve the apparent discrepancy of observing equipartition at high M_t for solenoidally forced DNS [61, 140].

We demonstrate small-scale universality for the wide range of forcing conditions by successfully collapsing the ratio of dilatational to solenoidal dissipation and the skewness of the velocity gradient. To the first order, the ratio of dissipations scales as δ^2 and the scaling laws based on M_t proposed by theories such as pseudosound and weak equipartition, and observed in DNS are subsets of this general scaling. Skewness of the velocity gradient is an important parameter in incompressible turbulence whose value is -0.5 for fully developed turbulence and is often used as a robust measure for deciding if the flow field is turbulent or not. Thus a value other than -0.5 can be deemed as compressibility effects. In fact, the larger negative value of skewness at high M_t has been attributed to shocklets in the flow field. Large negative skewness is possible even at low M_t when forced dilatationally. Moreover, yet again, it is seen that skewness scales as $\delta^2 M_t$ and skewness diverges from the incompressible value at around $\delta^2 M_t = 0.03$ and we call this phenomena as “S-divergence".

We introduce the concept of trajectories in the $\delta - M_t$ phase plane. There is no one to one relation between δ and M_t. In fact, the exact trajectory traversed by the system in the $\delta - M_t$ phase plane depends on the exact details of forcing. Thus, in general, M_t is not a measure of compressibility strength but rather, it is a measure of the interactions between the solenoidal and dilatational modes. We have discussed above the various transitions that can occur in compressible

turbulence. Interestingly the system may have crossed one transitional regime but not the other and it depends on the exact trajectory, thus on the specific details of forcing.

Dissipative anomaly is a pivotal result in incompressible turbulence with implications to Kolmogorov theory. The fact that the normalized dissipation becomes independent of Reynolds number (viscosity) is related to the energy cascade from large to small scales, and has been tested thoroughly in incompressible turbulence. Dissipative anomaly in compressible turbulence, on the other hand, is not well understood. For the solenoidal part of the velocity field, we observe dissipative anomaly similar to incompressible turbulence provided only the solenoidal variables are used which indicates that the cascade properties of the solenoidal velocity are not affected by compressibility. The total dissipation exhibits two asymptotic scaling regimes corresponding to the solenoidal and dilatational dissipation dominated regimes. From the data, we estimate the criterion for this transition in terms of δ and R_λ. At low $\delta < 0.1$, we show that the normalized dilatational dissipation scales inversely with δ. Assuming that most of the dissipation occur through shocklets, we derive a criteria for the dilatational cascade for those flow regimes where the solenoidal pressure dominates. A new normalization for the dilatational dissipation which takes into account the shocklet strength is proposed and found that it asymptotes to a constant when $\delta M_t > 0.1$ suggesting a cascade for the dilatational flow field

The energy spectrum is a measure of the energy content across scales, thus is an important parameter in turbulence theory. Although different scaling laws for energy spectra in compressible turbulence have been proposed, conflicting evidence in the literature has cast doubts on the validity of these scaling laws at different compressible regimes. The solenoidal spectra collapse under K41 scaling provided only the vortical modes are used for scaling even for cases with very high dilatational forcing. But no such collapse is observed for the dilatational spectra. Using a novel asymptotic analysis developed in Chap. 3, and analyzing the resulting equations, we divide the $\delta - M_t$ phase plane into distinct physical regimes. Each physical regime corresponds to a specific characteristic of compressible turbulence. We divide the phase plane into non-cascade and cascade regimes. The non-cascade regime consists of pseudosound [110] and weak equipartition [118]

regimes, the two low M_t theories proposed in the literature. The cascade regime is further classified into solenoidally driven cascade and wave steepening regimes. In the former, the dilatational flow field is largely driven by the solenoidal motions analogous to passive scalars in incompressible turbulence. Whereas in the wave steepening regime, dilatational modes are independent of the solenoidal motions and the energy spectra exhibit a k^{-2} scaling similar to Burgers turbulence. For each regime, we validate the scaling proposed in the literature. For example, the spectra in the pseudosound regime obey k^{-3} [110, 140] scaling as predicted. For those regimes, where the scaling laws are unknown, we propose new scaling laws and satisfactory collapse is seen.

The classical Obukhov-Corrsin scaling for passive scalars in incompressible turbulence fails for scalars in compressible turbulence. However when rescaled with solenoidal variables, the passive scalar spectra collapse under O-C scaling. The scalar gradient aligns preferentially with the compressive direction of the symmetric solenoidal velocity gradient tensor. This behavior was also found to be universal but secondary compressibility effects were seen. The alignment of the scalar gradient with the dilatational symmetric velocity gradient is non-universal and its interactions depend on the values of δ and M_t.

In short, we successfully showed that universal behaviours can be found in compressible turbulence if we extend the intrinsic parameter space to explicitly include δ, the ratio of dilatational and solenoidal rms velocity along with the other traditional parameters, M_t and R_λ. Different characteristics of compressible turbulence have been proposed by theories and observed in DNS simulations depending on initial and forcing conditions. This has resulted in discrepancies and contradictory observations in the literature even for similar forcing conditions. We showed that after an exhaustive compilation of available data in the literature, such discrepancies can be resolved by dividing the $\delta - M_t$ phase into distinct physical regimes with corresponding physical characteristics. Through our novel two parameter expansion asymptotic analysis, we isolate the dominant equations for each regime and thus explain the physical behaviour in these regimes. The study was also extended to passive scalars where we showed that large and inertial range scales of scalar motions are primarily driven by solenoidal motions. Secondary compressibility effects at

smaller scales, but important are also explained. The universality principles and the $\delta - M_t$ phase plane proposed in our work can provide a robust framework to compare across different flow configurations and pave the road towards more general turbulence models and rigorous theories.

8.2 Future Research Directions

We finish this dissertation by pondering on some plausible future research directions that can stem out from our present work. Since the equations governing turbulence are so complicated, most theories are asymptotic in nature at high $R_\lambda \to \infty$, and of course, this condition is of immense importance and relevance to engineering. Thus the validity and refinement of the theory depend on the availability of high-fidelity simulation data which depends on the improvements in computational hardware and methods. Thus, in most cases, progress in our physical understanding are driven by advancements in the computational realm. Thus we discuss the future research directions from both perspectives below.

8.2.1 Computational Perspective

- The current simulation code solves the Navier-Stokes equations and includes a forcing scheme in physical space. We need to introduce other driving mechanics to assess in what sense small scales, for example, are independent of forcing details. One common alternative is the so-called deterministic forcing [41, 37]. However, this approach requires fields to be in spectral space since we have to freeze the energy at lower modes. The required Fourier transforms can be efficiently done using P3DFFT [100] but have potential overheads due to communications needed to perform the transforms. Nevertheless, implementing this deterministic forcing scheme will provide new capabilities that can help resolve some further long-standing and new issues in compressible turbulence:

    1. With the current approaches, one cannot estimate δ accurately during simulations. One has to checkpoint and compute it afterwards during post-processing. Since the deterministic forcing is in spectral space, it is a more robust way to control the value of δ by simply fixing the ratio of the amplitude of the solenoidal and dilatatational Fourier

modes of the spectra.

2. Due to the multi-scale nature of turbulence, most of the important statistics are in the spectral space. Again in the current state of affairs, as before one has to checkpoint frequently and post-process later to calculate these physical significant statistics. In the next generation exascale machines, at large scales, the writing to file I/O operation during simulations would be exorbitantly expensive and might not be feasible. Thus researchers are planning to do in-situ visualization and data analysis to avoid I/O operations. The in-situ data analysis is possible when forcing is only possible in the spectral space.

3. Finally, in this approach, the entire randomness will be exclusively due to Navier-Stokes dynamics. This would help to arrive at converged statistics much faster and further studies on universality can be done.

- The next generation DOE sponsored exascale supercomputers are based on GPU architecture. Thus it is pivotal to extend pilot study on GPU in the current dissertation to multiple GPU-MPI configurations. It might also be worthwhile to port the entire cDNS code into GPUs and explore more portable options like OPENACC, OpenMP, Kokkos or Rajas which can work on any GPU architectural platforms.

- The major bottleneck in large-scale simulations are communication overheads ultimately resulting in the loss of scalability when overheads dominate over computational time. For faster simulations, one can rely on the improvements in the hardware. Another route is modifying the computational algorithm by relaxing communications as in the so called asynchronous schemes [1, 33]. Recently, Komal and Donzis [77] used higher-order asynchronous schemes for compressible direct numerical simulations with very encouraging prospects in terms of accuracy and performance. But definitely further research is needed to evaluate the possibility of this approach.

8.2.2 Physics Perspective

- In the current study, we demonstrated universality in compressible turbulence for homogeneous flows including both isotropic and anisotropic flows. However these are idealized canonical flows designed to study concepts such as universality. Having established that universality is possible for these canonical flows, it is imperative to extend these studies or ideas to general flows such as shear layers, mixing layers and flows with complex geometries. Of course, in such configurations, one expects large scale flow statistics to depend on external conditions such as geometry, boundary, initial conditions. Due to the non-linearity and multi-scale nature of turbulence, it is reasonable to expect universality and the flow to be locally isotropic at smaller scales of motion. Further research in these directions are needed to establish universality in compressible turbulence for a wider range of flow conditions.

- Most of the compressible theories are confined to low M_t and a general satisfactory theory of compressible is still lacking for general compressibility conditions. Our work has pointed out the relevance of almost forgotten theories such as the statistical mechanics theory by Kriachnan and the renormalization group at high M_t using high fidelity DNS data. We believe that our systematic study on universality and the division of $\delta - M_t$ phase plane into physical regimes has simplified the problem to such an extent that there are prospects of making concrete progress on the validation and refinement of compressible theories which is definitely a possible line of research.

- The progress in the development of theories will ultimately lead way to more general robust compressible turbulence models. Our work has shown that a single unique compressible model may not be possible but different turbulence models are required for distinct physical regimes in the $\delta - M_t$ phase plane. Using a combination of statistical theories and DNS data at higher R_λ, a detailed analysis of inter-scale and inter-modal energy should be done to develop subgrid and turbulence models for LES and RANS simulations.

- The results here can be extended to incorporate more complicated physics. In this disserta-

tion, we have neglected bulk viscosity in our simulations. In reality, the high speed flows through atmosphere involve real gases. At such high speeds encountered in hypersonic contexts, other modes of energy such as vibrational and rotational in the molecule other than translational mode will be excited. At such conditions, effects of non-equilibrium thermodynamics on turbulence and vice-versa have to be taken into account. Although, some work has been done in this area in the past [5, 36, 64], further research needs to be done in this area and an improved understanding of compressible turbulence from this study will help in understanding and isolating effects pertaining to thermal non-equilibrium.

REFERENCES

[1] ADITYA, K., AND DONZIS, D. A. High-order asynchrony-tolerant finite difference schemes for partial differential equations. *J. Comp. Phys. 350* (2017), 550 – 572.

[2] ALUIE, H. Compressible turbulence: the cascade and its locality. *Phys. Rev. Lett 106*, 17 (2011), 174502.

[3] ALUIE, H., LI, S., AND LI, H. Conservative cascade of kinetic energy in compressible turbulence. *Astrophys. J. Lett. 751*, 2 (2012), L29.

[4] ASHURST, W. T., KERSTEIN, A. R., KERR, R. M., AND GIBSON, C. H. Alignment of vorticity and scalar gradient with strain rate in simulated Navier-Stokes turbulence. *Phys. Fluids 30* (1987), 2343–2353.

[5] BARANWAL, A., DONZIS, D. A., AND BOWERSOX, R. D. Vibrational turbulent Prandtl number in flows with thermal non-equilibrium. In *AIAA Scitech 2020 Forum, Orlando, FL, USA* (2020), p. 2052.

[6] BARENBLATT, G. I. *Scaling, Self-similarity, and Intermediate Asymptotics*. Cambridge University Press, New York, 1996.

[7] BARENBLATT, G. I., AND ZELDOVICH, Y. B. Self-similar solutions as intermediate asymptotics. *Annu. Rev. Fluid Mech. 4* (1972), 285–312.

[8] BATAILLE, F., AND ZHOU, Y. Nature of the energy transfer process in compressible turbulence. *Phys. Rev. E 59*, 5 (1999), 5417.

[9] BATCHELOR, G. K. Small-scale variation of convected quantities like temperature in turbulent fluid .1. General discussion and the case of small conductivity. *J. Fluid Mech. 5* (1959), 113–133.

[10] BAYLY, B. J., LEVERMORE, C. D., AND PASSOT, T. Density variations in weakly compressible flows. *Phys. Fluids 4* (1992), 945–954.

[11] BERTSCH, R. L., SUMAN, S., AND GIRIMAJI, S. S. Rapid distortion analysis of high Mach number homogeneous shear flows: characterization of flow-thermodynamics interaction regimes. *Phys. Fluids 24*, 12 (2012), 125106.

[12] BILGER, R. The structure of diffusion flames. *Comb. Sci. Tech. 13*, 1-6 (1976), 155–170.

[13] BILGER, R. W. Some aspects of scalar dissipation. *Flow. Turb. Comb. 72*, 2-4 (2004), 93–114.

[14] BLAISDELL, G. A., MANSOUR, N. N., AND REYNOLDS, W. C. Compressibility effects on the growth and structure of homogeneous turbulent shear-flow. *J. Fluid Mech. 256* (1993), 443–485.

[15] BLAISDELL, G. A., MANSOUR, N. N., AND REYNOLDS, W. C. Compressibility effects on the passive scalar flux within homogeneous turbulence. *Phys. Fluids 6* (1994), 3498–3500.

[16] BOS, W. J., SHAO, L., AND BERTOGLIO, J.-P. Spectral imbalance and the normalized dissipation rate of turbulence. *Phys. Fluids 19*, 4 (2007), 045101.

[17] BURATTINI, P., LAVOIE, P., AND ANTONIA, R. A. On the normalized turbulent energy dissipation rate. *Phys. Fluids 17*, 9 (2005), 098103.

[18] CAI, X. D., O'BRIEN, E. E., AND LADEINDE, F. Advection of mass fraction in forced, homogeneous, compressible turbulence. *Phys. Fluids 10* (1998), 2249–2259.

[19] CAO, N., CHEN, S., AND DOOLEN, G. D. Statistics and structures of pressure in isotropic turbulence. *Phys. Fluids 11*, 8 (1999), 2235–2250.

[20] CHAKRABORTY, N., AND SWAMINATHAN, N. Influence of the Damköhler number on turbulence-scalar interaction in premixed flames. i. physical insight. *Phys. Fluids 19*, 4 (2007), 045103.

[21] CHEN, C. H., AND DONZIS, D. A. Shock-turbulence interactions at high turbulence intensities. *J. Fluid Mech. 870* (2019), 813–847.

[22] CHEN, S., WANG, J., LI, H., WAN, M., AND CHEN, S. Spectra and Mach number scaling in compressible homogeneous shear turbulence. *Phys. Fluids 30*, 6 (2018), 065109.

[23] CHEN, S., WANG, X., WANG, J., WAN, M., LI, H., AND CHEN, S. Effects of bulk viscosity on compressible homogeneous turbulence. *Phys. Fluids 31*, 8 (2019), 085115.

[24] CHU, B.-T., AND KOVÁSZNAY, L. S. Non-linear interactions in a viscous heat-conducting compressible gas. *J. Fluid Mech. 3*, 5 (1958), 494–514.

[25] CLAY, M., BUARIA, D., YEUNG, P., AND GOTOH, T. GPU acceleration of a petascale application for turbulent mixing at high Schmidt number using OpenMP 4.5. *Comp. Phys. Comm. 228* (2018), 100–114.

[26] CORRSIN, S. On the spectrum of isotropic temperature fluctuations in an isotropic turbulence. *J. Appl. Phys. 22* (1951), 469–473.

[27] DANISH, M., S., S., AND S., G. S. Influence of flow topology and dilatation on scalar mixing in compressible turbulence. *J. Fluid Mech. 793* (2016), 633–655.

[28] DAVIDSON, P. A. *Turbulence: an introduction for scientists and engineers*. Oxford University Press, NewYork, 2015.

[29] DIMOTAKIS, P. E. Turbulent mixing. *Annu. Rev. Fluid Mech. 37* (2005), 329–356.

[30] DOERING, C. R., AND FOIAS, C. Energy dissipation in body-forced turbulence. *J. Fluid Mech. 467* (2002), 289–306.

[31] DONZIS, D. A. Amplification factors in shock-turbulence interactions: effect of shock thickness. *Phys. Fluids 24* (2012), 011705.

[32] DONZIS, D. A. Shock structure in shock-turbulence interactions. *Phys. Fluids 24* (2012), 126101.

[33] DONZIS, D. A., AND ADITYA, K. Asynchronous finite-difference schemes for partial differential equations. *J. Comp. Phys. 274*, 0 (2014), 370 – 392.

[34] DONZIS, D. A., AND JAGANNATHAN, S. Fluctuations of thermodynamic variables in stationary compressible turbulence. *J. Fluid Mech. 733* (2013), 221–244.

[35] DONZIS, D. A., AND JOHN, J. P. Universality and scaling in compressible turbulence. *arXiv preprint arXiv:1907.07871* (2019).

[36] DONZIS, D. A., AND MAQUI, A. F. Statistically steady states of forced isotropic turbulence in thermal equilibrium and non-equilibrium. *J. Fluid Mech. 797* (2016), 181–200.

[37] DONZIS, D. A., AND SREENIVASAN, K. R. The bottleneck effect and the Kolmogorov constant in isotropic turbulence. *J. Fluid Mech. 657* (2010), 171–188.

[38] DONZIS, D. A., SREENIVASAN, K. R., AND YEUNG, P. K. Scalar dissipation rate and dissipative anomaly in isotropic turbulence. *J. Fluid Mech. 532* (2005), 199–216.

[39] DONZIS, D. A., SREENIVASAN, K. R., AND YEUNG, P. K. The Batchelor spectrum for mixing of passive scalars in isotropic turbulence. *Flow, Turb. Comb. 85* (2010), 549–566.

[40] DONZIS, D. A., SREENIVASAN, K. R., AND YEUNG, P. K. Some results on the Reynolds number scaling of pressure statistics in isotropic turbulence. *Physica D 241* (2012), 164 – 168.

[41] DONZIS, D. A., AND YEUNG, P. K. Resolution effects and scaling in numerical simulations of passive scalar mixing in turbulence. *Physica D 239* (2010), 1278–1287.

[42] DURBIN, P. A., AND ZEMAN, O. Rapid distortion theory for homogeneous compressed turbulence with application to modeling. *J. Fluid Mech. 242* (1992), 349–370.

[43] ERLEBACHER, G., HUSSAINI, M. Y., KREISS, H. O., AND SARKAR, S. The analysis and simulation of compressible turbulence. *Theoret. Comput. Fluid Dynamics 2* (1990), 73–95.

[44] ESWARAN, V., AND POPE, S. B. An examination of forcing in direct numerical simulations of turbulence. *Comput. Fluids 16* (1988), 257–278.

[45] EYINK, G. L., AND DRIVAS, T. D. Cascades and dissipative anomalies in compressible fluid turbulence. *Phys. Rev. X 8* (Feb 2018), 011022.

[46] FARBER, R. *Parallel programming with OpenACC*. Elsevier, 50 Hampshire Street, 5th Floor, Cambridge, MA 02139, United States, 2016.

[47] FEDERRATH, C., KLESSEN, R. S., AND SCHMIDT, W. The density probability distribution in compressible isothermal turbulence: solenoidal versus compressive forcing. *Astrophys. J. Lett. 688* (2008), L79–L82.

[48] FEDERRATH, C., KLESSEN, R. S., AND SCHMIDT, W. The fractal density structure in supersonic isothermal turbulence: solenoidal versus compressive energy injection. *Astrophys. J. 692* (2009), 364–374.

[49] FEDERRATH, C., ROMAN-DUVAL, J., KLESSEN, R. S., SCHMIDT, W., AND LOW, M.-M. M. Comparing the statistics of interstellar turbulence in simulations and observations-solenoidal versus compressive turbulence forcing. *Astro. & Astrophys. 512* (2010), A81.

[50] FOYSI, H., FRIEDRICH, R., AND SARKAR, S. On the micro-structure of the scalar field in compressible forced isotropic turbulence and supersonic channel flow. In *TSFP DIGITAL LIBRARY ONLINE* (2005), Begel House Inc.

[51] FRISCH, U. *Turbulence*. Cambridge University Press, the Edinburgh building, Shaftesbury road, Cambridge CB2 2RU, UK, 1995.

[52] GATSKI, T. B., AND BONNET, J.-P. *Compressibility, turbulence and high speed flow*, second ed. Elsevier, the Boulevard, Langford lane, Kidlington, Oxford OX5 1GB,UK, 2013.

[53] GOLDENFELD, N. Roughness-induced critical phenomena in a turbulent flow. *Phys. Rev. Lett. 96* (2006), 044503.

[54] GOTOH, G., FUKAYAMA, D., AND NAKANO, T. Velocity field statistics in homogeneous steady turbulence obtained using a high-resolution direct numerical simulation. *Phys. Fluids 14* (2002), 1065–1081.

[55] HADRI, B. Introduction to parallel I/O. *Online at https://www.nics.tennessee.edu/files/pdf/hpcss13_14/04_08_Parallel_IO_Part1.pdf* (2011).

[56] HAMLINGTON, P. E., POLUDNENKO, A. Y., AND ORAN, E. S. Interactions between turbulence and flames in premixed reacting flows. *Phys. Fluids 23*, 12 (2011), 125111.

[57] HARTUNG, G., HULT, J., KAMINSKI, C., ROGERSON, J., AND SWAMINATHAN, N. Effect of heat release on turbulence and scalar-turbulence interaction in premixed combustion. *Phys. Fluids 20*, 3 (2008), 035110.

[58] ISHIHARA, T., GOTOH, T., AND KANEDA, Y. Study of high-Reynolds number isotropic turbulence by direct numerical simulation. *Annu. Rev. Fluid Mech. 41* (2009), 165–180.

[59] JAGANNATHAN, S. Reynolds and Mach number scaling in stationary compressible turbulence using massively parallel high resolution direct numerical simulations. *Ph.D. dissertation, Texas A & M University* (2014).

[60] JAGANNATHAN, S., AND DONZIS, D. A. Massively parallel direct numerical simulations of forced compressible turbulence: a hybrid MPI/OpenMP approach. *Proceedings of the 1st Conference of the XSEDE, Chicago, IL* (2012), 23.

[61] JAGANNATHAN, S., AND DONZIS, D. A. Reynolds and Mach number scaling in solenoidally-forced compressible turbulence using high-resolution direct numerical simulations. *J. Fluid Mech. 789* (2016), 669–707.

[62] JOHN, J. P., DONZIS, D. A., AND SREENIVASAN, K. R. Solenoidal scaling laws for compressible mixing. *Phys. Rev. Lett. 123*, 22 (2019), 224501.

[63] KANEDA, Y., ISHIHARA, T., YOKOKAWA, M., ITAKURA, K., AND UNO, A. Energy dissipation rate and energy spectrum in high resolution direct numerical simulations of turbulence in a periodic box. *Phys. Fluids 15* (2003), L21–L24.

[64] KHURSHID, S., AND DONZIS, D. A. Decaying compressible turbulence with thermal nonequilibrium. *Phys. Fluids 31*, 1 (2019), 015103.

[65] KIDA, S., AND ORSZAG, S. A. Energy and spectral dynamics in forced compressible turbulence. *J. Sci. Comp. 5* (1990), 85–125.

[66] KIDA, S., AND ORSZAG, S. A. Energy and spectral dynamics in decaying compressible turbulence. *J. Sci. Comp. 7* (1992), 1–34.

[67] KIM, S. H., AND PITSCH, H. Scalar gradient and small-scale structure in turbulent premixed combustion. *Phys. Fluids 19*, 11 (2007), 115104.

[68] KNAUS, R., AND PANTANO, C. On the effect of heat release in turbulence spectra of non-premixed reacting shear layers. *J. Fluid Mech. 626* (2009), 67–109.

[69] KOLLA, H., HAWKES, E., KERSTEIN, A., SWAMINATHAN, N., AND CHEN, J. On velocity and reactive scalar spectra in turbulent premixed flames. *J. Fluid Mech. 754* (2014), 456–487.

[70] KOLMOGOROV, A. N. Local structure of turbulence in an incompressible fluid for very large Reynolds numbers. *Dokl. Akad. Nauk. SSSR 30* (1941), 299–303.

[71] KOLMOGOROV, A. N. A refinement of previous hypotheses concerning the local structure of turbulence in a viscous incompressible fluid at high Reynolds number. *J. Fluid Mech. 13* (1962), 82–85.

[72] KONSTANDIN, L., GIRICHIDIS, P., FEDERRATH, C., AND KLESSEN, R. S. A new density variance–Mach number relation for subsonic and supersonic isothermal turbulence. *Astrophys. J.* (2012).

[73] KOVASZNAY, L. S. G. Turbulence in supersonic flow. *J. Aeronaut. Sci. 20*, 10 (1953), 657–674.

[74] KRAICHNAN, R. H. On the statistical mechanics of an adiabatically compressible fluid. *J. Acous. Soc. Amer. 27*, 3 (1955), 438–441.

[75] KRAICHNAN, R. H. Small-scale structure of a scalar field convected by turbulence. *Phys. Fluids 11* (1968), 945–953.

[76] KRITSUK, A. G., NORMAN, M. L., PADOAN, P., AND WAGNER, R. The statistics of supersonic isothermal turbulence. *Astroph. J. 665*, 1 (2007), 416–431.

[77] KUMARI, K., AND DONZIS, D. A. Direct numerical simulations of turbulent flows using high-order asynchrony-tolerant schemes: accuracy and performance. *arXiv preprint arXiv:2003.10561* (2020).

[78] LADEINDE, F., O'BRIEN, E. E., CAI, X., AND LIU, W. Advection by polytropic compressible turbulence. *Phys. Fluids 7* (1995), 2848–2857.

[79] LANDAU, L. D., AND LIFSHITZ, E. M. *Fluid mechanics*. Pergamon Press, 1987.

[80] LEE, K., AND GIRIMAJI, S. Flow-thermodynamics interactions in decaying anisotropic compressible turbulence with imposed temperature fluctuations. *Theoret. Comput. Fluid Dynamics* (2011), 1–17.

[81] LEE, S., LELE, S. K., AND MOIN, P. Eddy shocklets in decaying compressible turbulence. *Phys. Fluids 3* (1991), 657–664.

[82] LEE, S., LELE, S. K., AND MOIN, P. Simulation of spatially evolving turbulence and the applicability of Taylor hypothesis in compressible flow. *Phys. Fluids 4* (1992), 1521–1530.

[83] LEES, A., AND ALUIE, H. Baropycnal work: A mechanism for energy transfer across scales. *Fluids 4*, 2 (2019), 92.

[84] LELE, S. K. Compressibility effects on turbulence. *Annu. Rev. Fluid Mech. 26* (1994), 211–254.

[85] LIVESCU, D., AND MADNIA, C. K. Compressibility effects on the scalar mixing in reacting homogeneous turbulence. In *IUTAM Symposium on turbulent Mixing and Combustion, Kingston, Ontario, Canada* (2002), Springer, pp. 125–135.

[86] LOGAN, J., AND DICKENS, P. Towards an understanding of the performance of MPI-IO in lustre file systems. In *2008 IEEE International Conference on Cluster Computing, Tsukuba, Japan* (2008), IEEE, pp. 330–335.

[87] MAHLE, I., FOYSI, H., SARKAR, S., AND FRIEDRICH, R. On the turbulence structure in inert and reacting compressible mixing layers. *J. Fluid Mech. 593* (2007), 171–180.

[88] MCCOMB, W. D. *Homogeneous, isotropic turbulence: phenomenology, renormalization and statistical closures*, vol. 162. OUP Oxford, 2014.

[89] MCCOMB, W. D., BERERA, A., SALEWSKI, M., AND YOFFE, S. Taylor's (1935) dissipation surrogate reinterpreted. *Phys. Fluids 22*, 6 (2010), 061704.

[90] MCDANIEL, J., GOYNE, C., EDWARDS, J., CHELLIAH, H., CUTLER, A., AND GIVI, P. US national center for hypersonic combined cycle propulsion: an overview. In *16th AIAA/DLR/DGLR International Space Planes and Hypersonic Systems and Technologies Conference, Bremen, Germany* (2009), p. 7280.

[91] MIURA, H., AND KIDA, S. Acoustic energy-exchange in compressible turbulence. *Phys. Fluids 7* (1995), 1732–1742.

[92] MOIN, P., AND MAHESH, K. Direct numerical simulation: A tool in turbulence research. *Annu. Rev. Fluid Mech. 30* (1998), 539–578.

[93] MONIN, A. S., AND YAGLOM, A. M. *Statistical fluid mechanics, Vol. II*. MIT Press, 1975.

[94] NI, Q. Compressible turbulent mixing: Effects of Schmidt number. *Phys. Rev. E 91* (May 2015), 053020.

[95] NI, Q. Compressible turbulent mixing: Effects of compressibility. *Phys. Rev. E 93* (Apr 2016), 043116.

[96] OBUKHOV, A. M. The structure of the temperature field in a turbulent flow. *Izv. Akad. Nauk. SSSR 13* (1949), 58–69.

[97] PAN, S., AND JOHNSEN, E. The role of bulk viscosity on the decay of compressible, homogeneous, isotropic turbulence. *J. Fluid Mech. 833* (2017), 717–744.

[98] PEARSON, B., KROGSTAD, P.-Å., AND VAN DE WATER, W. Measurements of the turbulent energy dissipation rate. *Phys. Fluids 14*, 3 (2002), 1288–1290.

[99] PEARSON, B. R., YOUSEF, T. A., HAUGEN, N. E. L., BRANDENBURG, A., AND KROGSTAD, P.-Å. Delayed correlation between turbulent energy injection and dissipation. *Phys. Rev. E 70*, 5 (2004), 056301.

[100] PEKUROVSKY, D. P3dfft: A framework for parallel computations of fourier transforms in three dimensions. *SIAM J. Sci. Comp. 34*, 4 (2012), C192–C209.

[101] PETERS, N. *Turbulent Combustion*. Cambridge University Press, Cambridge, United Kingdom, 2000.

[102] PIROZZOLI, S., AND GRASSO, F. Direct numerical simulations of isotropic compressible turbulence: Influence of compressibility on dynamics and structures. *Phys. Fluids 16* (2004), 4386 – 4407.

[103] PITSCH, H., AND STEINER, H. Scalar mixing and dissipation rate in large-eddy simulations of non-premixed turbulent combustion. *Proceed. Comb. Inst. 28*, 1 (2000), 41–49.

[104] POPE, S. B. *Turbulent Flows*. Cambridge University Press, Cambridge, United Kingdom, 2000.

[105] PORTER, D. H., POUQUET, A., AND WOODWARD, P. R. A numerical study of supersonic turbulence. *Theoret. Comput. Fluid Dynamics 4*, 1 (1992), 13–49.

[106] PORTER, D. H., POUQUET, A., AND WOODWARD, P. R. Three-dimensional supersonic homogeneous turbulence: a numerical study. *Phys. Rev. Lett. 68*, 21 (1992), 3156.

[107] PORTER, D. H., POUQUET, A., AND WOODWARD, P. R. Kolmogorov-like spectra in decaying 3-dimensional supersonic flows. *Phys. Fluids 6* (1994), 2133–2142.

[108] PRATURI, D. S., AND GIRIMAJI, S. S. Effect of pressure-dilatation on energy spectrum evolution in compressible turbulence. *Phys. Fluids 31*, 5 (2019), 055114.

[109] RAVIKUMAR, K., APPELHANS, D., AND YEUNG, P. GPU acceleration of extreme scale pseudo-spectral simulations of turbulence using asynchronism. In *Proceedings of the International Conference for High Performance Computing, Networking, Storage and Analysis, Denver, CO, USA* (2019), pp. 1–22.

[110] RISTORCELLI, J. R. A pseudo-sound constitutive relationship for the dilatational covariances in compressible turbulence. *J. Fluid Mech. 347* (1997), 37–70.

[111] RUETSCH, G., AND FATICA, M. *CUDA Fortran for scientists and engineers: best practices for efficient CUDA Fortran programming*. Elsevier, 225 Wyman Street, Waltham, MA 02451, USA, 2013.

[112] SAGAUT, P., AND CAMBON, C. *Homogeneous Turbulence Dynamics*. Springer International Publishing AG, Gewerbestrasse 11, 6330 Cham, Switzerland, 2018.

[113] SAMTANEY, R., PULLIN, D. I., AND KOSOVIC, B. Direct numerical simulation of decaying compressible turbulence and shocklet statistics. *Phys. Fluids 13* (2001), 1415–1430.

[114] SARKAR, S. The pressure-dilatation correlation in compressible flows. *Phys. Fluids 4* (1992), 2674.

[115] SARKAR, S. The stabilizing effect of compressibility in turbulent shear flow. *J. Fluid Mech. 282* (1995), 163–186.

[116] SARKAR, S., ERLEBACHER, G., AND HUSSAINI, M. *Compressible homogeneous shear: simulation and modeling. In Turbulent Shear Flows 8 (ed. F.Durst et al.).* Springer, 1993, pp. 249–267.

[117] SARKAR, S., ERLEBACHER, G., AND HUSSAINI, M. Y. Direct simulation of compressible turbulence in a shear flow. *Theoret. Comput. Fluid Dynamics 2*, 5-6 (1991), 291–305.

[118] SARKAR, S., ERLEBACHER, G., HUSSAINI, M. Y., AND KREISS, H. O. The analysis and modelling of dilatational terms in compressible turbulence. *J. Fluid Mech. 227* (1991), 473–493.

[119] SCHMIDT, W., FEDERRATH, C., HUPP, M., KERN, S., AND NIEMEYER, J. C. Numerical simulations of compressively driven interstellar turbulence. *A&A 494*, 1 (2009), 127–145.

[120] SIMONE, A., COLEMAN, G. N., AND CAMBON, C. The effect of compressibility on turbulent shear flow: A rapid-distortion-theory and direct-numerical-simulation study. *J. Fluid Mech. 330* (JAN 10 1997), 307–338.

[121] SMITS, A. J., AND DUSSAUGE, J. P. *Turbulent shear layers in supersonic flow*. Springer, 2006.

[122] SREENIVASAN, K. R. On the scaling of the turbulence energy-dissipation rate. *Phys. Fluids 27* (1984), 1048–1051.

[123] SREENIVASAN, K. R. The passive scalar spectrum and the Obukhov-Corrsin constant. *Phys. Fluids 8* (1996), 189–196.

[124] SREENIVASAN, K. R. An update on the energy dissipation rate in isotropic turbulence. *Phys. Fluids 10* (1998), 528–529.

[125] SREENIVASAN, K. R. Turbulent mixing: A perspective. *Proc. Nat. Acad. Sci.* (2018).

[126] SREENIVASAN, K. R., AND ANTONIA, R. A. The phenomenology of small-scale turbulence. *Annu. Rev. Fluid Mech. 29* (1997), 435–472.

[127] SREENIVASAN, K. R., ANTONIA, R. A., AND DANH, H. Q. Temperature dissipation fluctuations in a turbulent boundary layer. *Phys. Fluids 20*, 8 (1977), 1238–1249.

[128] STAROSELSKY, I., YAKHOT, V., KIDA, S., AND ORSZAG, S. A. Long-time, large-scale properties of a randomly stirred compressible fluid. *Phys. Rev. Lett. 65* (Jul 1990), 171–174.

[129] SWAMINATHAN, N., AND GROUT, R. W. Interaction of turbulence and scalar fields in premixed flames. *Phys. Fluids 18*, 4 (2006), 045102.

[130] TAYLOR, G. I. Statistical theory of turbulence. *Proc. R. Soc. Lond. A 151* (1935), 421–444.

[131] TENNEKES, H., AND LUMLEY, J. L. *A First Course in Turbulence*. The MIT Press, 1972.

[132] THAKUR, R., GROPP, W., AND LUSK, E. On implementing MPI-IO portably and with high performance. In *Proceedings of the sixth workshop on I/O in parallel and distributed systems, Atlanta, GA, USA* (1999), pp. 23–32.

[133] URZAY, J. Supersonic combustion in air-breathing propulsion systems for hypersonic flight. *Annu. Rev. Fluid Mech. 50* (2018), 593–627.

[134] VALENTE, P. C., AND VASSILICOS, J. C. The decay of turbulence generated by a class of multiscale grids. *J. Fluid Mech. 687* (2011), 300–340.

[135] VASSILICOS, J. C. Dissipation in turbulent flows. *Annu Rev. Fluid Mech. 47* (2015), 95–114.

[136] VEDULA, P., YEUNG, P. K., AND FOX, R. O. Dynamics of scalar dissipation in isotropic turbulence: a numerical and modelling study. *J. Fluid Mech. 433* (2001), 29–60.

[137] VREMAN, A. W., SANDHAM, N. D., AND LUO, K. H. Compressible mixing layer growth rate and turbulence characteristics. *J. Fluid Mech. 320* (1996), 235–258.

[138] WAIDMANN, W., ALFF, F., BRUMMUND, U., BÖHM, M., CLAUSS, W., AND OSCHWALD, M. Experimental investigation of the combustion process in a supersonic combustion ramjet (scramjet). *DGLR Jahrbuch, Erlangen, Bavaria, Germany* (1994), 629–638.

[139] WANG, J., GOTOH, T., AND WATANABE, T. Shocklet statistics in compressible isotropic turbulence. *Phys. Rev. Fluids 2* (Feb 2017), 023401.

[140] WANG, J., GOTOH, T., AND WATANABE, T. Spectra and statistics in compressible isotropic turbulence. *Phys. Rev. Fluids 2* (Jan 2017), 013403.

[141] WANG, J., SHI, Y., WANG, L.-P., XIAO, Z., HE, X., AND CHEN, S. Effect of shocklets on the velocity gradients in highly compressible isotropic turbulence. *Phys. Fluids 23* (2011), 125103.

[142] WANG, J., SHI, Y., WANG, L.-P., XIAO, Z., HE, X. T., AND CHEN, S. Scaling and statistics in three-dimensional compressible turbulence. *Phys. Rev. Lett. 108* (May 2012), 214505.

[143] WANG, J., WAN, M., CHEN, S., AND CHEN, S. Kinetic energy transfer in compressible isotropic turbulence. *J. Fluid Mech. 841* (2018), 581–613.

[144] WANG, J., WAN, M., CHEN, S., XIE, C., AND CHEN, S. Effect of shock waves on the statistics and scaling in compressible isotropic turbulence. *Phys. Rev. E 97* (Apr 2018), 043108.

[145] WANG, J., WAN, M., CHEN, S., XIE, C., WANG, L.-P., AND CHEN, S. Cascades of temperature and entropy fluctuations in compressible turbulence. *J. Fluid Mech. 867* (2019), 195 215.

[146] WANG, J., YANG, Y., SHI, Y., XIAO, Z., HE, X., AND CHEN, S. Cascade of kinetic energy in three-dimensional compressible turbulence. *Phys. Rev. Lett. 110*, 21 (2013), 214505.

[147] WANG, J., YANG, Y., SHI, Y., XIAO, Z., HE, X. T., AND CHEN, S. Statistics and structures of pressure and density in compressible isotropic turbulence. *J. Turbul. 14*, 6 (2013), 21–37.

[148] WANG, L. P., CHEN, S., BRASSEUR, J. G., AND WYNGAARD, J. C. Examination of hypotheses in the kolmogorov refined turbulence theory through high-resolution simulations .1. velocity field. *J. Fluid Mech. 309* (1996), 113–156.

[149] WARHAFT, Z. Passive scalars in turbulent flows. *Annu. Rev. Fluid Mech. 32* (2000), 203–240.

[150] WHITE, T. G., OLIVER, M. T., MABEY, P., KÜHN-KAUFFELDT, M., BOTT, A. F. A., DÖHL, L. N. K., BELL, A. R., BINGHAM, R., CLARKE, R., FOSTER, J., ET AL. Supersonic plasma turbulence in the laboratory. *Nat. Comm. 10*, 1 (2019), 1758.

[151] WIDOM, B. Equation of state in the neighborhood of the critical point. *J. Chem. Phys. 43*, 11 (1965), 3898–3905.

[152] YAKHOT, V., AND DONZIS, D. A. Emergence of multiscaling in a random-force stirred fluid. *Phys. Rev. Lett. 119* (Jul 2017), 044501.

[153] YAKHOT, V., AND DONZIS, D. A. Anomalous exponents in strong turbulence. *Physica D. 384-385* (2018), 12–17.

[154] YANG, J., GOTOH, T., MIURA, H., AND WATANABE, T. Statistical properties of an incompressible passive vector convected by isotropic turbulence. *Phys. Rev. Fluids 4* (Jun 2019), 064601.

[155] YEUNG, P. K., XU, S., AND SREENIVASAN, K. R. Schmidt number effects on turbulent transport with uniform mean scalar gradient. *Phys. Fluids 14* (2002), 4178–4191.

[156] YEUNG, P. K., AND ZHOU, Y. Universality of the Kolmogorov constant in numerical simulations of turbulence. *Phys. Rev. E 56* (1997), 1746–1752.

[157] ZANK, G., AND MATTHAEUS, W. Nearly incompressible hydrodynamics and heat conduction. *Phys. Rev. Lett. 64*, 11 (1990), 1243.

[158] ZANK, G. P., AND MATTHAEUS, W. H. The equations of nearly incompressible fluids. i. hydrodynamics, turbulence, and waves. *Phys. Fluids 3*, 1 (1991), 69.

APPENDIX A

ASYMPTOTIC EQUATIONS

A.1 Compressible Navier-Stokes Equations

$$O\left(1\right):\frac{\partial\widehat{w_i^s}}{\partial\tau}+\widehat{u_j^s}\frac{\partial\widehat{w_i^s}}{\partial\eta_j}=-\frac{1}{\sqrt{\rho}}\frac{\partial\widehat{p^s}}{\partial\eta_i}+\frac{1}{\sqrt{\rho}}\left(\frac{\partial}{\partial\eta_j}\frac{\partial\widehat{u_i^s}}{\partial\eta_j}+\frac{\partial}{\partial\eta_j}\frac{\partial\widehat{u_j^s}}{\partial\eta_i}\right) \tag{A.1a}$$

$$O\left(\delta\right):\frac{\partial\widehat{w_i^d}}{\partial\tau}+\widehat{u_j^d}\frac{\partial\widehat{w_i^s}}{\partial\eta_j}+\widehat{u_j^s}\frac{\partial\widehat{w_i^d}}{\partial\eta_j}+\widehat{w_i^s}\frac{\partial\widehat{u_j^d}}{\partial\eta_j}=-\frac{1}{\sqrt{\rho}}\frac{\partial\widehat{p^d}}{\partial\xi_i}+\frac{1}{\sqrt{\rho}}\left(\frac{\partial}{\partial\eta_j}\frac{\partial\widehat{u_i^d}}{\partial\eta_j}+\frac{\partial}{\partial\eta_j}\frac{\partial\widehat{u_j^d}}{\partial\eta_i}+\frac{\partial}{\partial\eta_i}\frac{\partial\widehat{u_j^d}}{\partial\eta_j}\right) \tag{A.1b}$$

$$O\left(\frac{1}{M_t}\right):\frac{\partial\widehat{w_i^s}}{\partial\tau'}=0 \tag{A.1c}$$

$$O\left(\frac{\delta}{M_t}\right):\frac{\partial\widehat{w_i^d}}{\partial\tau'}=\frac{-1}{\sqrt{\rho}}\frac{\partial\widehat{p^d}}{\partial\eta_i} \tag{A.1d}$$

$$O\left(\delta^2\right):\widehat{u_j^d}\frac{\partial\widehat{w_i^d}}{\eta_j}+\widehat{w_i^d}\frac{\partial\widehat{u_j^d}}{\eta_j}=\frac{-1}{\sqrt{\rho}}\frac{\partial\widehat{p^d}}{\partial\xi_i} \tag{A.1e}$$

$$O\left(M_t\right):2*\frac{\partial}{\partial\xi_j}\frac{\partial\widehat{u_i^s}}{\partial\eta_j}+\frac{\partial}{\partial\eta_i}\frac{\partial\widehat{u_j^s}}{\partial\xi_j}+\frac{\partial}{\partial\eta_j}\frac{\partial\widehat{u_j^s}}{\partial\xi_i}=\frac{-1}{\sqrt{\rho}}\frac{\partial\widehat{p^s}}{\partial\eta_i} \tag{A.1f}$$

$$0\left(M_t^2\right):\frac{\partial}{\partial\xi_j}\frac{\partial\widehat{u_i^s}}{\partial\xi_j}=0 \tag{A.1g}$$

$$O\left(\delta M_t\right):\widehat{w_i^s}\frac{\partial\widehat{u_j^d}}{\partial\xi_j}+\widehat{u_j}^d\frac{\partial\widehat{w}_i{}^s}{\partial\xi_j}+\widehat{u_j}^s\frac{\partial\widehat{w_j^d}}{\partial\xi_j}=2*\frac{\partial}{\partial\xi_j}\frac{\partial\widehat{u}_i{}^d}{\partial\eta_j}+\frac{\partial}{\partial\xi_i}\frac{\partial\widehat{u}_j{}^d}{\partial\eta_j}+\frac{\partial}{\partial\eta_i}\frac{\partial\widehat{u}_j{}^d}{\partial\xi_j} \tag{A.1h}$$

$$O\left(\delta M_t^2\right) : \frac{\partial}{\partial \xi_j}\frac{\partial \widehat{u_i}^d}{\partial \xi_j} + 2 * \frac{\partial}{\partial \xi_i}\frac{\partial \widehat{u_j}^d}{\partial x_j} = 0 \tag{A.1i}$$

$$O\left(\delta^2 M_t\right) : \widehat{u_j}^d \frac{\partial \widehat{w_i}^d}{\partial \xi_j} + \widehat{w_i}^d \frac{\partial \widehat{u_j}^d}{\partial \xi_j} = 0 \tag{A.1j}$$

A.2 Solenoidal Kinetic Energy Equations

$$O\left(1\right) : \left\langle w_i^s \frac{\partial w_i^s}{\partial \tau}\right\rangle + \left\langle \widehat{w}_i^s \left\{ u_j^s \widehat{\frac{\partial w_i^s}{\partial \eta_j}} \right\}^s \right\rangle_k = -\left\langle \widehat{w}_i^s \left\{ \frac{1}{\sqrt{\rho}} \widehat{\frac{\partial p^s}{\partial \eta_i}} \right\}^s \right\rangle_k + \left\langle \widehat{w}_i^s \frac{1}{\sqrt{\rho}} \left\{ \left(\frac{\partial}{\partial \eta_j}\frac{\partial \widehat{u}_i^s}{\partial \eta_j} + \frac{\partial}{\partial \eta_j}\frac{\partial \widehat{u}_j^s}{\partial \eta_i} \right) \right\}^s \right\rangle_k \tag{A.2a}$$

$$O\left(\delta\right) : \left\langle \widehat{w}_i^s \left\{ u_j^d \widehat{\frac{\partial w_i^s}{\partial \eta_j}} \right\}^s \right\rangle_k + \left\langle \widehat{w}_i^s \left\{ u_j^s \widehat{\frac{\partial w_i^d}{\partial \eta_j}} \right\}^s \right\rangle_k + \left\langle \widehat{w}_i^s \left\{ w_i^s \widehat{\frac{\partial u_j^d}{\partial \eta_j}} \right\}^s \right\rangle_k = -\left\langle \widehat{w}_i^s \left\{ \frac{1}{\sqrt{\rho}} \widehat{\frac{\partial p^d}{\partial \xi_i}} \right\}^s \right\rangle_k \tag{A.2b}$$

$$O\left(\frac{1}{M_t}\right) : \left\langle \widehat{w}_i^s \frac{\partial w_i^s}{\partial \tau'} \right\rangle = 0 \tag{A.2c}$$

$$O\left(\frac{\delta}{M_t}\right) : \left\langle \widehat{w}_i^s \left\{ \frac{1}{\sqrt{\rho}} \widehat{\frac{\partial p^d}{\partial \eta_i}} \right\}^s \right\rangle_k = 0 \tag{A.2d}$$

$$O\left(\delta^2\right) : \left\langle \widehat{w}_i^s \left\{ u_j^d \widehat{\frac{\partial w_i^d}{\partial \eta_j}} \right\}^s \right\rangle_k + \left\langle \widehat{w}_i^s \left\{ w_i^d \widehat{\frac{\partial u_j^d}{\partial \eta_j}} \right\}^s \right\rangle_k = -\left\langle \widehat{w}_i^s \left\{ \frac{1}{\sqrt{\rho}} \widehat{\frac{\partial p^d}{\partial \xi_i}} \right\}^s \right\rangle_k \tag{A.2e}$$

$$O\left(M_t\right) : 2\left\langle \widehat{w}_i^s \left\{ \frac{\partial}{\partial \xi_j} \widehat{\frac{\partial u_i^s}{\partial \eta_j}} \right\}^s \right\rangle_k + \left\langle \widehat{w}_i^s \left\{ \frac{\partial}{\partial \eta_i} \widehat{\frac{\partial u_j^s}{\partial \xi_j}} \right\}^s \right\rangle_k + \left\langle \widehat{w}_i^s \left\{ \frac{\partial}{\partial \eta_j} \widehat{\frac{\partial u_j^s}{\partial \xi_i}} \right\}^s \right\rangle_k = 0 \tag{A.2f}$$

$$0\left(M_t^2\right):\left\langle \widehat{w}_i^s\left\{\widehat{\frac{\partial}{\partial\xi_j}\frac{\partial u_i^s}{\partial\xi_j}}\right\}^s\right\rangle_k=0 \tag{A.2g}$$

$$O\left(\delta M_t\right):\left\langle \widehat{w}_i^s\left\{w_i^s\widehat{\frac{\partial u_j^d}{\partial\xi_j}}\right\}^s\right\rangle_k+\left\langle \widehat{w}_i^s\left\{u_j^d\widehat{\frac{\partial w_i^s}{\partial\xi_j}}\right\}^s\right\rangle_k+\left\langle \widehat{w}_i^s\left\{u_j^s\widehat{\frac{\partial w_j^d}{\partial\xi_j}}\right\}^s\right\rangle_k=0 \tag{A.2h}$$

$$O\left(\delta^2 M_t\right):\left\langle \widehat{w}_i^s\left\{u_j^d\widehat{\frac{\partial w_i^d}{\partial\xi_j}}\right\}^s\right\rangle+\left\langle \widehat{w}_i^s\left\{w_i^d\widehat{\frac{\partial u_j^d}{\partial\xi_j}}\right\}^s\right\rangle_k=0 \tag{A.2i}$$